NTNU – Trondheim
Norwegian University of
Science and Technology

Arterial Flow and Pulse Wave Propagation in one dimensional Arterial Networks with Statistically Distributed Model Parameters

Vinzenz Gregor Eck

Master of Science in Product Design and Manufacturing
Submission date: June 2012
Supervisor: Leif Rune Hellevik, KT
Co-supervisor: Paul Roger Leinan, KT
Mahmoud Ismail, Institute for Computational Mechanics - Technische Universität München

Norwegian University of Science and Technology
Department of Structural Engineering

I. Assignment

Arterial Flow and Pulse Wave Propagation in one dimensional Arterial Networks with Statistically Distributed Model Parameters

One dimensional models of arterial networks are widely used to analyze arterial flow and pulse wave propagation. The models and their application have been employed extensively, but the issue of data uncertainty and statistically distributed model parameters has been considered little.

Suggested topics for the thesis are therefore:

- Presentation of a mathematical model for one dimensional arterial networks
- Introduction of the Polynomial Chaos method with relevant applications
- Coupling of the statistical method with the mathematical model
- Assessment of the impact of statistically distributed parameters on tentative example cases:
  - complete systemic arterial tree
  - truncated up/downstream networks used as boundary conditions for 3D models
  - arterial network before and after a vascular surgery (e.g stenting)
- Implementation of a method for advanced 3D visualisation of simulation results could be an additional topic

II. Preface

" One never knows, do one?[1] "

Fats Waller (1904 – 1943)

This work is conducted as my final Master/Diploma thesis concluding my double degree studies in mechanical engineering at the Technische Universität München (TUM) in Germany and the Norwegian University of Science and Technology (NTNU) in Norway.

The thesis is about simulation of uncertainty in the human blood flow system. More precisely, it presents a framework to evaluate the impact of statistically distributed model parameters in the arterial system on the pressure and flow of blood.
The research on blood flow in human arteries was not an obvious topic for me when I started my studies in engineering. Most examples and aspects of my studies have been dealing with the design and construction of technical solutions for human problems, as fast locomotion on land, sea and in the air. The idea to apply the knowledge of engineering science to a system which is inside everybody, but still not fully understood, fills me with curiosity and inquisitiveness.

Vinzenz Gregor Eck

June 11th 2012
Trondheim, Norway

[1] Source: B. Crow. Jazz Anecdotes. *Oxford University Press*,1990

III. Abstract

Parametric uncertainty in blood flow simulations of cardiovascular systems has received little attention, although methods for blood flow simulation has been subject of many studies. This work presents the implementation and assessment of a method for one dimensional flow and pressure wave simulations in arterial networks with statistically distributed model parameters. The pressure and flow waves in the arterial system are characterized by means of cross-sectionally averaged 1D governing equations for mass and momentum, discretized with a MacCormack scheme (explicit and second order in time and space). The stochastic model considered is a combination of a generalized polynomial chaos with a stochastic collocation method and joined with the one dimensional model. The implementation is validated with the simulation of a single arterial bifurcation, which has been published by others previously, with a somewhat different approach. The assessment is completed with a sensitivity analysis of the wave dynamics, in particular reflected waves, in the systemic arterial tree in the context of ageing. The numerical simulations showed that the impact of model uncertainty in different compartments of the arterial tree on systolic and diastolic pressure peaks can be determined with the elaborated method. In particular, the uncertainty in material parameters of the aortic arch showed a strong influence on the pressure wave forms.

IV. Sammendrag

Parametrisk usikkerhet i simuleringer av det kardiovaskulære systemet har fått liten oppmerksomhet. Dette til tross for stor interesse for blodstrømningsmodellering i litteraturen. Denne masteroppgaven vil presentere gjennomføringen og vurderingen av en metode for 1-dimensional volumstrøm og trykk bølgeforplanting i det arterielle nettverk med statistisk dristribuerte modellparametere. Trykk- og strømningsbølgene i det arterielle systemet er karakterisert ved hjelp av 1D ligningene for bevaring av masse og bevegelsmengde, diskretisert av MacCormack skjema (eksplisitt og 2. grad i tid og rom). Den stokastiske modellen er en kombinasjon av 'generalized polynomial chaos' med 'stochastic collocation method', i kombinasjon med den 1-dimensjonale modellen. Implementeringen er verifisert med en simulation av en enkel bifurkasjon, fra en en tidligere publikasjon med en litt annen framgangsmåte. Til slutt har det blitt gjennomført en sensitivitetsanalyse av bølgedynamikken i det arterielle karsystemet, spesielt med tanke på endringen av de reflekterte bølgene som en følge av aldring. De numeriske simuleringene viste at effekten av usikkerheten i det arterielle systemet kan ved hjelp av den implementerte modellen, fastsette de maksimale verdiene av systole- og diastoletrykket. Spesielt har usikkerheten på grunn materialparameterene i aorta en betydelig inflytelse på trykkbølgene.

V. Acknowledgements

First, I would like to thank my professor and supervisor, Leif Rune Hellevik, for his guidance and sharing his thoughts, which has helped me much in developing this work.
I would like to express my appreciation to doctorate student Jonathan Feinberg for his introduction to the theory of generalized polynomial chaos, as well as answering all my questions.
I also would like to thank doctorate student Paul Roger Leinan for the inspirations and fruitful discussions.
In addition, thanks to Moritz Heber and Knut-Petter Maråk for their advices and the proofreading of my work.
And last, I would like to thank my biomechanical fellows, Elisabeth Meland and Thomas Eeg, for the nice and motivating atmosphere in our office.

List of Abbreviations

PDF	probability density function
STD	standard deviation
2D	two dimensional
3D	three dimensional
CFL	Courant Friedrich Levy
CSV	comma-separated values
gPCE	generalized polynomial chaos expansion
gPC	generalized polynomial chaos
HDD	hard disk drive
IDE	integrated development environment
LUT	look up table
MCS	Monte Carlo Sampling
NTNU	Norwegian University of Science and Technology
PDE	partial differential equation
SI	International System of Units (abbr. from french: Système international d'unités)
SPDE	stochastic partial differential equations
TUM	Technische Universität München (University of Technology, Munich)
VPC	vascular polynomial chaos
XML	Extensible Markup Language

List of Applied Software

Mathematical Frameworks

Vascular1DFlow

software for flow modeling in compliant vessel networks by Leinan, P. and Hellevik, L. (2012). Division of Biomechanics, NTNU, Trondheim
http://www.ntnu.edu/biomechanics

Polynomial Chaos Toolbox

software for generalized polynomial chaos simulations by Feinberg, J. (2012). Simula research laboratory,Oslo.
http://www.simula.no

Programming Language and Libraries

$python^{TM}$	programming language	http://www.python.org
lxml2	parser for XML files	http://lxml.de/lxml2.html
csv	parser for CSV files	http://docs.python.org/library/csv.html
Cpickle	parser for python data types	http://docs.python.org/library/pickle.html
Graphviz	network visualisation software	http://www.graphviz.org/Home.php
pydot	python interface for Graphviz	http://code.google.com/p/pydot
xdot	python viewer for Graphviz graphs	http://code.google.com/p/jrfonseca
numpy	library for numerical computations	http://numpy.scipy.org/
scipy	library for scientific computations	http://scipy.org/
mayavi2	library for 3D visualisation	http://code.enthought.com/projects/mayavi
matplotlib	library for scientific plotting	http://matplotlib.sourceforge.net
pygtk	library for graphical user interfaces	http://www.pygtk.org
timeit	module for process time evaluation	http://docs.python.org/library/timeit.html

Additional Programs

Aptana Studio 3	IDE for python	http://www.aptana.com/
Calc of LibreOffice	spreadsheet program	http://www.libreoffice.org/features/calc/
DataThief	plot data extraction program	http://www.datathief.org/
Texaker	IDE for LaTeX	http://www.xm1math.net/texmaker/
Gimp	image manipulation program	http://www.gimp.org/

Nomenclature

α	limit factor of confidence interval
β	stiffness parameter of the compliance
Δt	time step
δx	length of a vessel segment
Δx	spacing between two grid nodes
γ	velocity profile parameter
Γ	domain of the joint probability density
λ_1	speed of w_1
λ_2	speed of w_2
λ_w	wavelength
$\mathbf{\Lambda}$	eigenvalue matrix
$\mathcal{P}$	probability measure
$\mathbf{M}$	system matrix
$\mathbf{R}$	right eigenmatrix
μ	dynamic viscosity of blood
ν	Poisson ratio
Ω	sample space
ω	event
$\Phi(z)$	multivariate orthogonal polynomial
$\phi(r)$	shape profile function
ρ	blood density
$\tilde{c}$	Fourier coefficients of the polynomial chaos expansion
Υ^*	theoretical relative STD
A	lumen area, cross-sectional area
a	acceleration
Amp	amplitude of a pulse peak
$\mathcal{A}$	σ-algebra
C	vessel compliance
c	pulse wave velocity, wave speed
D	number of random variables z_i
E	Young's Modulus of a vessel
$E[z]$,$\mathbb{E}$	expected value
$\mathbb{E}_i$	partial expected value
$\mathbb{E}_T$	total expected value
F	force
h	wall thickness of a vessel
K	collocation nodes
k	collocation node

L^d	deterministic system of equations
L^s	stochastic system of equations
L	vessel length
m	mass
M	order of polynomial chaos expansion
N	number of grid nodes
N_p	number of of polynomial chaos expansion terms
P	mean pressure
P_b	backward contribution of P
P_f	forward contribution of P
$p(z)$	probability density function of z
Q	volumetric flow rate
Q_b	backward contribution of Q
Q_f	forward contribution of Q
R_f^P	reflection coefficient
r, R	vessel radius
r_d	distal vessel radius
r_p	proximal vessel radius
STD_i	partial STD with respect to z_i
STD_T	total STD with respect to z
$STD^*{}_i$	relative partial STD
STD	standard deviation
$t_{occ.}$	occurrence time of a pulse peak
T_f^p	transmission coefficient
t	time
T	total simulation time
$\mathbf{u}$	vector of primary variables; P, Q and A.
$u(x,t,z)$	stochastic solution of the system L^s
U_K=$(\tilde{u}_1, \ldots, \tilde{u}_K)$	solution of all collocation evaluations
$\tilde{u}_k$	solution of one collocation evaluation
V_{con}	control Volume
$v_x = v_x(x,t)$	mean axial velocity
w_1	forward Riemann invariant
w_2	backward Riemann invariant
x	position along the vessel
$z = (z_1, \ldots, z_D)$	D-variant random vector containing random variables
Z_c	characteristic impedance
z_i	continuous random variable

Contents

List of Figures

List of Tables

1. Introduction

The cardiovascular system (figure 1) transports blood and with it vital substances like oxygen, nutrients and hormones in a closed cycle through the human body [10]. It consist of the heart, the lungs and blood vessels, classified in arteries, veins and capillary vessels. The pulmonary circulation (heart-lungs-heart), systemic circulation (heart-body-heart) and coronary circulation (blood supply of the heart) form the cardiovascular circulation.

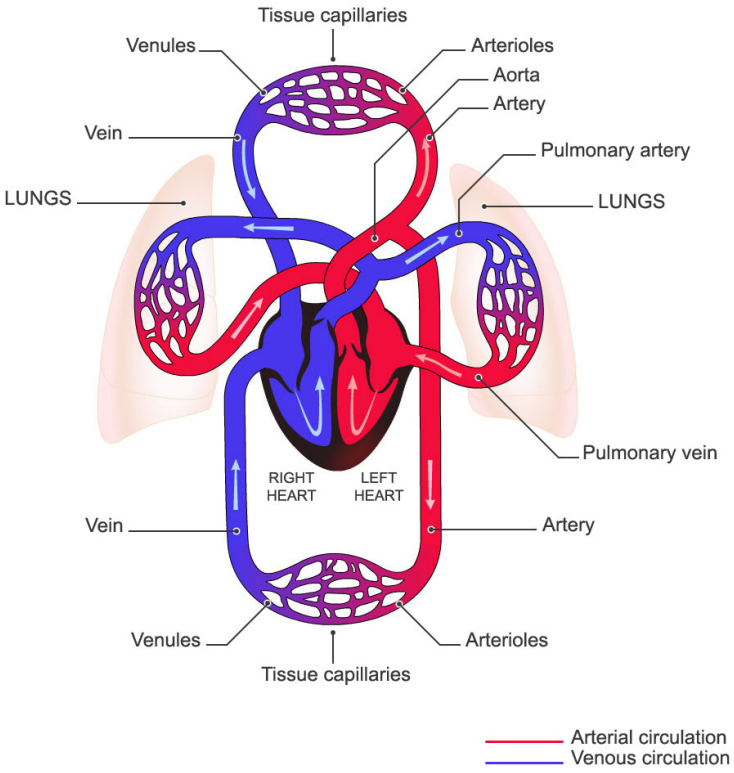

Figure 1: Schema of the human cardiovascular system[2]

The functionality and the design of this complex system with its ramified network of elastic tubes, was a research topic for many scientist through history [21]. The progress in computational resources allows the investigation of the blood flow in the circulatory system on much wider scale. Not only the basic understanding, but also the influence of stenosis [28], aneurysms [33], and other vascular diseases are getting more into the focus of the research.

[2]Image source : http://www.urgo.co.uk/260-the-venous-system-within-the-cardiovascular-system

There are three basic types of computer model approaches applied for the simulation of vascular flow; lumped parameter models, one dimensional models and three dimensional models with fluid structure interaction [29]. The lumped parameter models simplify the vascular system, and describe parts of the system *(e.g the hole systemic circulation)* as one lumped compartment. The one dimensional approach, offers more detailed physics (pressure, flow and wall shear stress in axial direction and time) than the lumped parameter model, which has no spatial distribution [39]. The three dimensional models point out very high accuracy, but are not yet feasible for larger vascular networks. Thus they are mainly used to investigate local flow and velocity patterns [7] *e.g. at bifurcations or inside the heart.* However, to determine the change of pressure and flow over time and space in large arterial systems, one dimensional models stand out with accurate performance [26].

The systemic circulation, especially the arterial tree, has been subject of many simulation studies with one dimensional models (overview in Reymond et al. [23]), as they provide realistic results under a variety of physiological and pathological conditions. All of theses studies are based on deterministic models, assuming certain model parameters. However, the simulation of vascular networks include many model parameters, which cannot be determined without uncertainty. The physiological data, the material and geometry parameters of vessels and the blood properties can generally be regarded as uncertain in nature. In addition comes the uncertainty of the measurements while evaluating these data from test subjects. The other part of uncertainty is up to the boundary conditions. However, there is only one study by D. Xiu and S.J. Sherwin [38] presenting a model to simulate uncertainty in vascular networks.

To increase the knowledge about uncertainty in the systemic circulation, this work is focused on the design and implementation of a framework (vascular polynomial chaos) for uncertainty analysis of the systemic circulation. The uncertainty analysis covers the simulation of networks with uncertain parameters and subsequent sensitivity analysis to investigate the effect and influence of the uncertain parameters. The vascular polynomial chaos combines a deterministic one dimensional model (vascular1DFlow) with a generalized polynomial chaos method (polynomial chaos toolbox), to asses the variability in vascular systems.

In section 2, the applied theory and the used frameworks vascular1DFlow and polynomial chaos toolbox are presented. Section 3 gives an overview of the elaborated vascular polynomial chaos framework and its methods. Section 4 outlines the verification of the elaborated approach on a small test case (section 4.1). After the verification, the elaborated vascular polynomial chaos framework is used for the uncertainty analysis of the systemic arterial tree, in order to show the full potential of this method (section 4.2).

2. Therory and Applied Methods

2.1. Mathematical Framework - vascular1DFlow

The mathematical model for blood flow simulation in vascular systems applied in this work is called vascular1DFlow[3]. The following sections give a brief introduction to the mathematics of vascular1DFlow, starting with the system of governing equations solved for each simulation step. Furthermore, some mathematical methods and conditions concerning simulation of wave phenomena will be discussed.

2.1.1. System of Governing Equations

Conservation of Mass and Momentum

Blood flow in the arterial system can, like any other fluid system, be described with the conservation of mass and the Navier-Stokes equations in integral form [13]. The conservation of mass equation states the mass balance within control a volume V_{con}. The Navier-Stokes equations or momentum equations are based on Newtons second law *($F = m \cdot a$)* and state the balance between inertia and net forces within a control volume V_{con}.
Blood is assumed to be a Newtonian fluid with dynamic viscosity μ and density ρ. The vascular system is regarded as one dimensional in space with straight compliant tubes with a circular cross section [1].
[NB: referred to hereafter as vessel or branch]
A vessel segment with the length δx is employed as control volume V_{con}. The integrated form of conservation of mass and momentum equations for V_{con} are:

$$\frac{\partial A}{\partial t} + \frac{\partial Q}{\partial x} = 0 \tag{2.1a}$$

$$\frac{\partial Q}{\partial t} + \frac{\partial}{\partial x}\left(2\pi \int_0^R r v^2 dr\right) + \frac{A}{\rho}\frac{\partial P}{\partial x} = -2\pi\frac{\mu}{\rho}\left[\frac{\partial v}{\partial r}\right]_{r=R} \tag{2.1b}$$

The primary variables, the mean pressure $P = P(x,t)$, the volumetric flow rate $Q = Q(x,t)$ and the lumen area $A = A(x,t)$ are average quantities over the cross sections of the vessel segment (equation 2.2a-2.2c). They depend only on the position along the vessel x and the time t.

[3]Leinan, P. and Hellevik, L. (2012). Vascular1DFlow: Software for flow modeling in compliant vessel networks. Division of Biomechanics, NTNU

$$A(x,t) = 2\pi \int_0^{R_{(x,t)}} r \, dr \tag{2.2a}$$

$$Q(x,t) = 2\pi \int_0^{R_{(x,t)}} r v(x,r,t) \, dr = A(x,t)\, v_x(x,t) \tag{2.2b}$$

$$P(x,t) = \frac{2\pi}{A(x,t)} \int_0^{R_{(x,t)}} r p(x,r,t) \, dr, \tag{2.2c}$$

where $v_x = v_x(x,t)$ is the mean axial velocity.

The second and forth term in the momentum equation (equation 2.1b), are the convective acceleration and the viscous wall friction force respectively, both depend on the velocity profile in a local cross section.

Velocity Profiles

The velocity profiles are in general approximated and assumed to be axial symmetric to the axis x (i.e. axis along a vessel). Common approaches to model velocity profiles [29] are:

- assumed shape profiles: flat, Poiseuille, power law, assumed stokes layer
- time periodic profiles : Womersley velocity profile
- approximated profiles

In vascular1DFlow the power law is applied as an approximation for the velocity profile. In general, a function $\phi(r)$ is defined for the assumed shape profiles such that:

$$v(x,r,t) = \phi(r) v_x(x,t), \tag{2.3}$$

where $v_x(x,t)$ is the mean (cross sectional) axial velocity. $\phi(r)$ for the power law profile introduced by T.J.R. Hughes and J. Lubliner [13] is assumed to be:

$$\phi(r) = \frac{\gamma+2}{\gamma}\left(1 - \left(\frac{r}{R}\right)^{\gamma}\right), \tag{2.4}$$

where R is the radius of the vessel, and γ determines the bluntness of the velocity profile. The non-slip condition at the vessel wall is satisfied with $\phi(R) = 0$. Furthermore, $\gamma = 1$ results in a flat profile and $\gamma = 2$ in a Poiseuille flow profile.

Finally, by substituting 2.3 and 2.4 into the momentum equation 2.1b, the v_x-terms are expressed with the primary variables Q and A:

$$\frac{\partial Q}{\partial t} + \delta \frac{\partial}{\partial x}\left(\frac{Q^2}{A}\right) + \frac{A}{\rho}\frac{\partial P}{\partial x} = -2\pi(\gamma+2)\frac{\mu}{\rho}\frac{Q}{A} \tag{2.5}$$

$$\text{with} \quad \delta = \frac{(\gamma+2)}{(\gamma+1)} \tag{2.6}$$

Constitutive Laws

The conservation of mass (2.1a) and momentum equations (2.1b) state two differential equations, with three primary variables (P, Q and A). Consequently a constitutive law (i.e. a physical relation between primary variables) is needed to close the system of equations.

Blood vessels have elastic properties, i.e the cross sectional areas A change due to alteration in pressure P. The vessel compliance C is defined as a measure for the changes in cross sectional area A. Generally it is a function of the location in the vascular network and time dependent through viscoelastic effects [24]. The spatial variations can be attributed to factors like variations in material properties with respect to *e.g. collagen fibre architecture, support from surrounding tissue, and variations in vessel cross sectional area.*

Here the vessel compliance is assumed to be a function of pressure P, location x and time t:

$$C(x,t,P) = \frac{\partial A(P)}{\partial P} \tag{2.7}$$

With the vessel compliance (2.7) a constitutive law for A and P is given, which closes the two governing equations (2.1a) and (2.1b). Applying the chain rule of derivation to the first term of the conservation of mass (2.1a) and including the vessel compliance yields:

$$\frac{\partial P}{\partial t} + \frac{1}{C}\frac{\partial Q}{\partial x} = 0. \tag{2.8}$$

The vessel compliance can be derived form a constitutive model, stating the relation of P and A. There exist several constitutive models, here the focus will be on the model types implemented in vascular1DFlow: *Laplace* and *exponential*. Each model has a stiffness parameter β, hence, they are superscribed with the constitutive model name; β^{Lap} and β^{exp} respectively.

The Laplace description is based on Laplace's law with the assumption of a thin, homogeneous and elastic vessel wall [26]:

$$P = P_s + \beta^{Lap}(\sqrt{A} - \sqrt{A_s}), \tag{2.9}$$

where P_s and A_s are reference pressure and area, respectively. Differentiation of the algebraic form (2.9) with respect to P yields an expression for the compliance:

$$C = \frac{\partial A}{\partial P} = \frac{2}{\beta^{Lap}}\sqrt{A_s} + \frac{2}{(\beta^{Lap})^2}(P - P_s) \tag{2.10}$$

The stiffness parameter β^{Lap} is defined as a function of some vessel material parameters such as: reference area A_S, Young's modulus $E(x)$ and wall thickness $h(x)$:

$$\beta^{Lap} = \frac{\pi h E}{(1-\nu^2)A_s}, \tag{2.11}$$

where the Poisson ratio ν is typically assumed to be 0.5 for incompressible tissue.

A more physiological definition states the exponential relation, which has been determined from experiments by Hellevik et al. [11]:

$$P = P_s e^{\beta^{exp}(\frac{A}{A_s}-1)} \tag{2.12}$$

where A_s is the cross-sectional area of the vessel at a reference pressure P_s. By differentiating equation 2.12 with respect to P an expression for the compliance C is found:

$$C = \frac{\partial A}{\partial P} = \frac{A_s}{\beta^{exp} P} \quad \text{where} \quad P > 0 \tag{2.13}$$

Pulse Wave Velocity

The pulse wave velocity is expressed by the Bramwell-Hill equation [3]:

$$c = \sqrt{\frac{A}{\rho}\frac{\partial P}{\partial A}} = \sqrt{\frac{A}{\rho C}} \tag{2.14}$$

System Equations of vascular1DFlow

The governing equations for flow in a compliance vessel are in vascular1DFlow represented by a three equation system for the three primary variables (P, Q and A), the conservation of mass (2.1a), the momentum equation with power law velocity profile (2.5) and the conservation of mass combined with the vessel compliance (2.8):

$$\begin{aligned}
\frac{\partial A}{\partial t} + \frac{\partial Q}{\partial x} &= 0, && \text{recap eq. } (2.1a) \\
\frac{\partial Q}{\partial t} + \delta\frac{\partial}{\partial x}\left(\frac{Q^2}{A}\right) + \frac{A}{\rho}\frac{\partial P}{\partial x} &= -2\pi(\gamma+2)\frac{\mu}{\rho}\frac{Q}{A}, && \text{recap eq. } (2.5) \\
\frac{\partial P}{\partial t} + \frac{1}{C}\frac{\partial Q}{\partial x} &= 0, && \text{recap eq. } (2.8)
\end{aligned}$$

where $\delta = \frac{(\gamma+2)}{(\gamma+1)}$.

A similar approach can be found in the work of K. DeVault et al. [4]. In general it is adequate to describe the system with two of the equations above, in order to gain a closed system. A common approach is to represent the system by equation 2.1a and 2.5 with A, Q as primary variables, where a pressure-area relation (C) can be substituted into $\frac{\partial P}{\partial x}$ [6]. Another approach is the representation by equation 2.5 and 2.8 with P and Q as primary variables, where the pressure-area relation is readily available in the vessel compliance C [2]. Other possible choices include systems where the velocity v_x becomes one of the two primary variables, an overview can be found in *e.g.* S.J. Sherwin et al. [26].

However, in vascular1DFlow the three equation system is used, as the compliance can be defined as a more complex function, *e.g.:*

$$C(A, P, x, t) = \frac{\partial A}{\partial P} + \frac{\partial A}{\partial t} \tag{2.16}$$

The system equations written in matrix notation and rearranged becomes:

$$\frac{\partial \mathbf{u}}{\partial t} + \mathbf{M}(\mathbf{u})\frac{\partial \mathbf{u}}{\partial x} = \mathbf{b}(\mathbf{u}), \quad \mathbf{u} = \begin{bmatrix} P \\ Q \\ A \end{bmatrix}, \tag{2.17}$$

where

$$\mathbf{M} = \begin{bmatrix} 0 & \frac{1}{C} & 0 \\ Cc^2 & 2\delta v_x & -\delta v_x^2 \\ 0 & 1 & 0 \end{bmatrix}, \quad \mathbf{b} = \begin{bmatrix} 0 \\ -2\pi(\gamma+2)\frac{\mu}{\rho}v_x \\ 0 \end{bmatrix}, \tag{2.18}$$

and where $c^2 C = A/\rho$ (equation 2.14) and $v_x = Q/A$.

2.1.2. Numerical Discretization and Numerical Integration Scheme

A branch in the network is discretized on a uniform grid with N grid nodes $i = \{1, .., N\}$ and vessel length $L = \Delta x(N-1)$, where Δx is the spacing between two grid nodes. To solve the system equations 2.17 an explicit forward-backward MacCormack scheme [12] is implemented in vascular1DFlow for the interior grid nodes:

$$\text{for} \quad i = \{2, .., N-1\}$$

$$\overline{\mathbf{u}}_i^{n+1} = \mathbf{u}_i^n - \Delta t \left[\mathbf{M}(\mathbf{u}_i^n) \frac{(\mathbf{u}_{i+1}^n - \mathbf{u}_i^n)}{\Delta x} + \mathbf{b}(\mathbf{u}_i^n) \right] \tag{2.19}$$

$$\mathbf{u}_i^{n+1} = \frac{1}{2}(\mathbf{u}_i^n + \overline{\mathbf{u}}_i^{n+1} - \Delta t \left[\mathbf{M}(\overline{\mathbf{u}}_i^{n+1}) \frac{(\overline{\mathbf{u}}_i^{n+1} - \overline{\mathbf{u}}_{i-1}^{n+1})}{\Delta x} + \mathbf{b}(\overline{\mathbf{u}}_i^{n+1}) \right]) \tag{2.20}$$

where Δt is the time step.

First, with the *predictor* step (equation 2.19) $\overline{\mathbf{u}}_i^{n+1}$ is calculated. In a second step, $\overline{\mathbf{u}}_i^{n+1}$ given as input to the *corrector* step (equation 2.20), leads to the updated primary variables $\mathbf{u}_i^{n+1}$.

The boundary nodes $i = \{1, N\}$ are solved in a characteristic manner.

2.1.3. Characteristic Analysis

In the system of governing equations 2.17 the system variables P,Q and A are coupled in space and time with the off diagonal elements in matrix $\mathbf{M}$. This is also valid for a reduced system of governing equations, with the system variables P and Q consisting of equations 2.8 and 2.5. The reduced system and the system matrix are:

$$\frac{\partial \mathbf{u}}{\partial t} + \mathbf{M}(\mathbf{u})\frac{\partial \mathbf{u}}{\partial x} = 0 \tag{2.21}$$

$$\mathbf{M} = \begin{bmatrix} 0 & \frac{1}{C} \\ Cc^2 - \delta v_x^2 C & 2\delta v_x \end{bmatrix} \tag{2.22}$$

Both systems can be transformed into an uncoupled system, where the rows are independent of each other. This is done by linear algebra, using the eigenvalues and eigenmatrices. The transformation is here carried out for the reduced system, but follows the same schema for the three equations system.
The relation between the eigenvalues and the matrix $\mathbf{M}$ is given with the right eigenmatrix $\mathbf{R}$:

$$\mathbf{MR} = \mathbf{R\Lambda} \tag{2.23}$$

$\mathbf{\Lambda}$ is defined as the eigenvalue matrix of $\mathbf{M}$ containing the eigenvalues λ_1 and λ_2:

$$\mathbf{\Lambda} = \begin{bmatrix} \lambda_1 & 0 \\ 0 & \lambda_2 \end{bmatrix}, \tag{2.24a}$$

$$\lambda_1 = \delta v_x + \sqrt{c^2 + \delta(\delta-1)v_x^2} = \delta v_x + c' \tag{2.24b}$$

$$\lambda_2 = \delta v_x - \sqrt{c^2 + \delta(\delta-1)v_x^2} = \delta v_x - c' \tag{2.24c}$$

$$\text{where } c' = c\sqrt{\delta(\delta-1)\mathcal{M}^2} \text{ with } \mathcal{M} = \frac{v}{c}$$

The inverse of the right eigenmatrix is defined as the left eigenmatrix of $\mathbf{M}$: $\mathbf{L} = \mathbf{R}^{-1}$, and consequently, $\mathbf{LR} = \mathbf{I}$. The left and right eigen-matrices are:

$$\mathbf{R} = \begin{bmatrix} \mathbf{r}_1 & \mathbf{r}_2 \end{bmatrix}, \quad \mathbf{L} = \begin{bmatrix} \mathbf{l}_1^T \\ \mathbf{l}_2^T \end{bmatrix}, \tag{2.25}$$

where $\mathbf{l}_j^T$ and $\mathbf{r}_j$ for $j = \{1, 2\}$ are the left and right eigenvectors of the system matrix $\mathbf{M}$. Written out:

$$\mathbf{R}(\mathbf{u}) = \begin{bmatrix} -\frac{1}{(C\lambda_1)} & \frac{1}{(C\lambda_2)} \\ -1 & 1 \end{bmatrix}, \tag{2.26}$$

$$\mathbf{L}(\mathbf{u}) = \frac{C\lambda_1\lambda_2}{\lambda_1 - \lambda_2}\begin{bmatrix} 1 & -\frac{1}{(C\lambda_2)} \\ 1 & -\frac{1}{(C\lambda_1)} \end{bmatrix} \tag{2.27}$$

The differential system given in equation 2.21 can now be transformed in the equivalent form by multiplying with L from the left and substituting with 2.23:

$$\begin{aligned}
\frac{\partial \mathbf{u}}{\partial t} + \mathbf{M}\frac{\partial \mathbf{u}}{\partial z} &= 0 \\
\mathbf{L}\frac{\partial \mathbf{u}}{\partial t} + \mathbf{L}\mathbf{M}\frac{\partial \mathbf{u}}{\partial z} &= 0 \\
\mathbf{L}\frac{\partial \mathbf{u}}{\partial t} + \mathbf{L}\mathbf{R}\mathbf{\Lambda}\mathbf{R}^{-\mathbf{1}}\frac{\partial \mathbf{u}}{\partial z} &= 0 \\
\mathbf{L}\frac{\partial \mathbf{u}}{\partial t} + \mathbf{\Lambda}\mathbf{L}\frac{\partial \mathbf{u}}{\partial z} &= 0,
\end{aligned} \tag{2.28}$$

A change in variables is introduced by Sherwin et al. [26]:

$$\frac{\partial \mathbf{w}}{\partial \mathbf{u}} = \mathbf{L}, \tag{2.29}$$

where $\mathbf{w} = [w_1, w_2]^T$ is the vector of the characteristic variables. Introduction of the characteristic variables transforms the system into an uncoupled system with two non-zero Riemann invariants with two characteristic directions:

$$\frac{\partial \mathbf{w}}{\partial t} + \mathbf{\Lambda}\frac{\partial \mathbf{w}}{\partial z} = 0. \tag{2.30}$$

$$\mathbf{w} = \begin{bmatrix} w_1 \\ w_2 \end{bmatrix}. \tag{2.31}$$

In vascular1DFlow an incremental form of the Riemann invariants between two states, $\Delta t = t^{n+1} - t^n$ is implemented. Hence, the integration of the Riemann invariants equation 2.29, in combination with the mean value theorem gives:

$$\Delta \mathbf{w} = \int_{\mathbf{u}^n}^{\mathbf{u}^{n+1}} \frac{\partial \mathbf{w}}{\partial \mathbf{u}} d\mathbf{u} = \int_{\mathbf{u}^n}^{\mathbf{u}^{n+1}} \mathbf{L}(\mathbf{u})\, d\mathbf{u} = \mathbf{L}(\widehat{\mathbf{u}})\Delta \mathbf{u}. \tag{2.32}$$

where $\mathbf{u}^n \leq \widehat{\mathbf{u}} \leq \mathbf{u}^{n+1}$. Furthermore, the incremental change in the primary variables $\Delta \mathbf{u}$ is found from rearranging equation 2.32

$$\Delta \mathbf{u} = \mathbf{L}^{-1}(\widehat{\mathbf{u}})\Delta \mathbf{w} = \mathbf{R}(\widehat{\mathbf{u}})\Delta \mathbf{w}. \tag{2.33}$$

2.1.4. Linear Wave Splitting

Blood flow in the arterial system is pulsatile and can be characterized as forward and backward propagating flow and pressure waves. Forward directed pulses propagate from the heart toward the periphery. On the way through the arterial tree, some parts of the waves are reflected *e.g due to changes in vessel compliance or at bifurcations.* The reflected waves propagate back to the heart containing information related to the arterial tree and the periphery.
The flow and pressure signals $Q(t)$ and $P(t)$ measured at all points in the system can be split into forward and backward contributions. A common method for wave splitting suggested by N. Westerhof et al. [32] is based on the linearized and inviscid form of the governing equations (2.8) and (2.1b):

$$C\frac{\partial p}{\partial t} + \frac{\partial Q}{\partial x} = 0 \tag{2.34}$$

$$\frac{\partial Q}{\partial t} + \frac{A}{\rho}\frac{\partial p}{\partial x} = 0 \tag{2.35}$$

To separate the flow and pressure waves, the inviscid governing equations are first transformed into wave equations. After introducing the characteristic impedance, the linear wave splitting is conducted.

Wave Character of the Inviscid Governing Equations
Cross derivation of equation 2.34 and 2.35 followed by the subtraction of the resulting equations yields a partial differential equation (PDE) for the P and Q:

$$\frac{\partial^2 Q}{\partial t^2} + c^2\frac{\partial^2 Q}{\partial x^2} = 0 \tag{2.36}$$

$$\frac{\partial^2 p}{\partial t^2} + c^2\frac{\partial^2 p}{\partial x^2} = 0 \tag{2.37}$$

$$\textit{with:} \quad c^2 = \frac{A}{\rho C} \tag{2.38}$$

where the wave speed previously defined (equation 2.14) is inserted.
Both equations 2.36 and 2.37 are classic wave equations which have together the following general solutions:

$$P = P_0 f(x - ct) + P_0^* g(x + ct) \tag{2.39}$$

$$Q = Q_0 f(x - ct) + Q_0^* g(x + ct) \tag{2.40}$$

where f and g represent waves propagating with wave speed c forward and backward, respectively.

Characteristic Impedance

Inserting the solution for the wave equations 2.39 and 2.40 into the linearized momentum equation 2.35 yields:

$$-cQ_0 f' + cQ_0^* g' + \frac{A}{\rho} P_0 f' + \frac{A}{\rho} P_0^* g' = 0 \tag{2.41a}$$

$$f'(\frac{A}{\rho} P_0 - cQ_0) + g'(\frac{A}{\rho} P_0^* + cQ_0^*) = 0 \tag{2.41b}$$

As equations 2.41a and 2.41b must hold for arbitrarily chosen f and g, an expression for the characteristic impedance Z_c is obtained:

$$\left.\begin{aligned} \frac{A}{\rho} P_0 - cQ_0 \stackrel{!}{=} 0 \quad &\Rightarrow \quad \frac{P_0}{Q_0} = \frac{c\rho}{A} \\ \frac{A}{\rho} P_0^* + cQ_0^* \stackrel{!}{=} 0 \quad &\Rightarrow \quad -\frac{P_0^*}{Q_0^*} = \frac{c\rho}{A} \end{aligned}\right\} \equiv Z_c$$

$$Z_c = \frac{c\rho}{A} \quad \text{or} \quad Z_c = \frac{P}{Q} = \frac{P_f}{Q_f} = \frac{P_b}{Q_b} \tag{2.42}$$

From the expression above, the characteristic impedance Z_c is seen to be the ratio of the pulsatile pressure and flow components in the case of a unidirectional wave, i.e. in absence of reflections. Z_c expresses also the ratio of local inertia $\frac{\rho}{A}$ to compliance C substituting the Brahmwell-Hill equation for the wave speed 2.14 into equation 2.42:

$$Z_c = \sqrt{\frac{\rho}{AC}} \tag{2.43}$$

Linear Wave Splitting

Let $P_f = P(x - ct)$ and $P_b = P(x + ct)$ be a forward and a backward travelling pressure wave, respectively. Then the solutions P_f and P_b are constant along the characteristics $\Gamma : x \pm ct$. The same is applicable for the flow waves and its solutions: $Q_f = p(x - ct)$ and $Q_b = Q(x + ct)$. Consequently, the total flow and pressure are the sum of their forward and backward travelling components:

$$P = P_f + P_b, \quad Q = Q_f + Q_b \tag{2.44}$$

The forward and backward travelling pressure and flow contributions can be set in relation through the characteristic impedance Z_c (equation 2.42):

$$Q = \frac{P_f}{Z_c} - \frac{P_b}{Z_c}, \quad P = Z_c Q_f - Z_c Q_b \tag{2.45}$$

Through algebraic elimination using equations 2.44 and 2.45 the backward and forward contributions of pressure and flow can be calculated. Written in incremental form:

$$\Delta P_f = \frac{\Delta P + Z_c \Delta Q}{2}, \quad \Delta P_b = \frac{\Delta P - Z_c \Delta Q}{2} \tag{2.46}$$

$$\Delta Q_f = \frac{\Delta Q + \frac{\Delta P}{Z_c}}{2}, \quad \Delta Q_b = \frac{\Delta Q - \frac{\Delta P}{Z_c}}{2} \tag{2.47}$$

2.1.5. Non Linear Wave Splitting

Non linear wave splitting can be derived based on the characteristic analysis (section 2.1.3). With the w_1 a forward and w_2 a backward propagation Riemann invariant is given, containing all information travelling in each direction, respectively. From equation 2.32 and definition 2.27 one can state:

$$\frac{1}{\frac{C\lambda_1\lambda_2}{\lambda_1-\lambda_2)}} \begin{bmatrix} \Delta\mathbf{w_1} \\ \Delta\mathbf{w_2} \end{bmatrix} = \begin{bmatrix} \Delta\hat{w}_1 \\ \Delta\hat{w}_2 \end{bmatrix} = \begin{bmatrix} 1 & Z_2 \\ 1 & -Z_1 \end{bmatrix} \begin{bmatrix} \Delta P \\ \Delta Q \end{bmatrix}, \tag{2.48}$$

where $Z_2 = -\frac{1}{(C\lambda_2)}$ and $Z_1 = \frac{1}{(C\lambda_1)}$.
The two equations given in the system 2.48 can be rearranged yielding in two expressions for ΔP and ΔQ:

$$\Delta P = \frac{Z_1\hat{w}_1 + Z_2\hat{w}_2}{Z_1 + Z_2} \tag{2.49}$$

$$\Delta Q = \frac{\hat{w}_1 - \hat{w}_2}{Z_1 + Z_2} \tag{2.50}$$

The forward contribution of the system variables, is given for $\hat{w}_2 = 0$, the backward contributions for $\hat{w}_1 = 0$. The forward and backward contributions of the incremental pressure and flow waves are:

$$\Delta P_f = \frac{Z_1\hat{w}_1}{Z_1 + Z_2} \tag{2.51a}$$

$$\Delta P_b = \frac{Z_2\hat{w}_2}{Z_1 + Z_2} \tag{2.51b}$$

$$\Delta Q_f = \frac{\hat{w}_1}{Z_1 + Z_2} \tag{2.51c}$$

$$\Delta Q_b = \frac{-\hat{w}_2}{Z_1 + Z_2} \tag{2.51d}$$

For the linearised case, λ_1 = -λ_2, and Z_1=Z_2=Z_c. Inserting this into 2.50 and 2.49 yields to the expressions derived in the linear wave splitting section 2.1.4.

2.1.6. CFL Number and CFL Condition

The CFL number is a characteristic quantity which states the relation between numerical speed (Δx/Δt) and the largest velocity in the system with which information can propagate. In the system of vascualar1DFlow it is the speed of forward travelling Riemann invariant w_1: $\lambda_1 = \delta v_x + \sqrt{c^2 + \delta(\delta-1)v_x^2}$ (see section 2.1.3), as $\lambda_1 > \lambda_2$ since $v_x > 0$.

$$CFL = \lambda_1 \cdot \frac{\Delta t}{\Delta x} \tag{2.52}$$

The CFL condition (Courant, Friedrich, Levy, 1928) is a necessary but not sufficient condition for the stability of numerical schemes, especially explicit time integration schemes [12].

$$\text{CFL-condition: } 0 \leq CFL \leq 1.0 \tag{2.53}$$

In unsteady simulations of physical systems with wave phenomena and/or non linearities, the CFL condition arises under no matter what time integration scheme, explicit and implicit alike [22]. If the simulation proceeds faster than the physical solution, not all information is caught from one time step to the next. The accuracy of the simulation, i.e a proper representation of the physics of the system, decreases. Numerical speed slower than the physical velocity i.e $CFL << 1$ leads to dissipation and dispersion in the solution [12]. Therefore, the time step (Δt) and/or grid inter size (Δx) is determined in order to match the CFL condition. However, λ is a function of the system variables P,Q and A, as $v_x = A/Q$ and $c = f(A, C(P))$. Due to this, CFL changes during the simulation. The prediction of the highest CFL before running the simulation is challenging as a result of the non linear relationship between the system variables. As an approximation, the velocity v_x is assumed to be zero. CFL becomes a function of c_o, the wave speed calculated with known reference area and pressure *(e.g. at initial condition)*:

$$CFL \approx c_o \cdot \frac{\Delta t}{\Delta x} \tag{2.54}$$

In doing so, the CFL condition has to be underestimated as $c < \lambda_1$. Figure 2 shows the calculated CFL numbers of a simulation with λ_1, c_o and the approximation error. In vascular1DFlow, the time step is determined with this approximation of the CFL (see section 3.8.1). By examining CFL numbers after the simulation, the extent of the underestimation can be controlled.

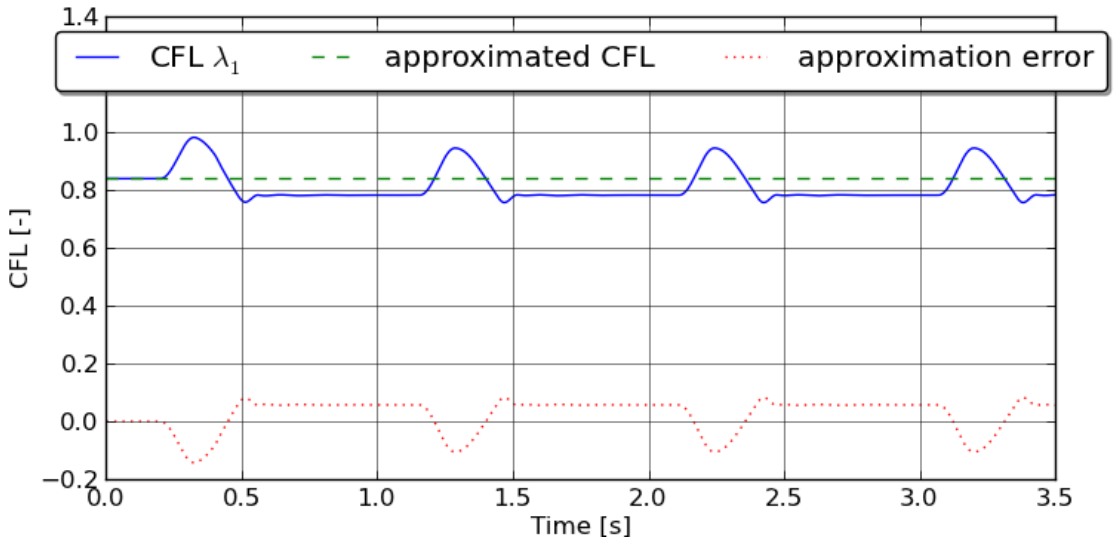

Figure 2: Comparison of the predicted approximated CFL and the actual CFL number of a simulation. The approximation in this case was appropriate, as the actual CFL λ_1 never exceeds 1.0 but stays close to it.

2.2. Stochastic Framework - Polynomial Chaos Toolbox

To evaluate the impact of stochastic variability of vascular network model parameters on the simulation result, the deterministic vascular1DFlow framework (section 2.1) needs stochastic components. By defining uncertain model parameters as continuous random variables, the deterministic PDEs of vascular1DFlow are recast to stochastic PDEs (SPDE). There are several approaches to solve/evaluate stochastic differential equations. Most common methods are solving the SPDE directly with stochastic calculus [14], [8] or applying the Monte Carlo Sampling (MCS) [5]. However, in the presented work the relatively new generalized polynomial chaos (gPC) model is applied [37]. With gPC, the stochastic solution of the SPDE is expressed as a set of orthogonal polynomials of the uncertain network parameters, the general polynomial chaos expansion (gPCE). The gPCE is constructed with deterministic solutions of the PDE for a very small set of sample points. The sample points are selected by a Stochastic Collocation method from possible permutations of the uncertain parameter values of the network. Compared to a MSC simulation with 10 000 executions, the gPC needs five evaluations to achieve the same accuracy [34].
The construction of the gPCE is conducted by a stochastic framework, whereas a mathematical framework, here vascular1DFlow (section 2.1), solves the deterministic PDEs for each evaluation.
The stochastic framework applied in the present work is the *polynomial chaos toolbox* [4].

2.2.1. Basic Expressions and Definitions

The following sections concentrate on random variables with continuous probability density function. However, the generalized polynomial chaos is also suitable for discrete random variables. A brief summary of some stochastic terms to enhance the understanding is given below. Further information on stochastic calculus can be found in Montgomery and Runger [19], Georgii [9] or Gardiner [8].

Sample Space Ω
: is a set of all possible outcomes of a random trail or experiment. A sample space is continuous if it consists of an interval of either finite or infinite real numbers.

Event ω
: is a subset of outcomes in the sample space Ω. It can be seen as the conditional sample space of a random trail or experiment.

Continuous Random Variable z_i
: is a function that associates a real number with each element in the continuous sample space ω or Ω.

[4] Jonathan Feinberg (2012). polynomial chaos toolbox: software for generalized polynomial chaos simulations. Simula research laboratory, Oslo

Probability Density Function (PDF) $p(z)$

describes the the probability distribution of the continuous random variable z. The probability that z is between a and b is determined by the integral of $p(z)$ from a to b.

Probability Distribution

or cumulative distribution function of a continuous random variable is the integral of its probability density function. Well-known probability distributions are *e.g. Uniform, Gaussian, Gamma or Weibull distribution.*

Expected Value $E[z], \mathbb{E}$

of a continuous random variable is the average of all real numbers, which the random variable can take on, weighted with the probability density.

$$E[z] = \int_{-\infty}^{\infty} zp(z)dz \tag{2.55}$$

Variance

is the measurement of the dispersion or variability of a continuous random variable.

$$\sigma^2 = Var(z) = \int_{-\infty}^{\infty} (z-\mu)^2 p(z)dz \tag{2.56}$$

Standard Deviation (STD)

defined as the square root of the variance.

$$\sigma = STD(z) = \sqrt{Var} = \sqrt{\sigma^2} \tag{2.57}$$

100($1-\alpha$*)%-Confidence Interval*

is an interval estimate for the plausibility of the outcomes of an experiment. The interval includes all outcomes of an experiment which are 100($1-\alpha$)% plausible. In general, a 100($1-\alpha$) confidence interval [a,b] is defined, such that:

$$\begin{aligned} P(Z < a) &= alpha/2 \\ P(a <= Z <= b) &= 1 - alpha \\ P(Z > b) &= alpha/2 \end{aligned} \tag{2.58}$$

2.2.2. Generalized Polynomial Chaos (gPC)

The system of SPDE $L^s(x,t,u,z)=0$ for the variable $u(x,t,z)$ is considered. L^s is defined in the fixed physical space $G \subset \mathbb{R}^a, a=1,2,3$ with the coordinates $x=(x_1,\ldots,x_a)$ and in time space $T \subset \mathbb{R}$ with the time variable t. In addition, the system L^s and the system variable u depend on a D-variant random vector $z=(z_1,\ldots,z_D) \in \mathbb{R}^D, D \geq 1$. Where all $(z_1,\ldots,z_D)$ are continuous random variables, which are assumed to be mutually independent of each other. This assumption allows a more straightforward numerical implementation [34]. However, it is also possible to use the generalized polynomial chaos method for a set of dependent random variables [27].
The D-variant random vector $z=(z_1,\ldots,z_D)$ is defined in the complete probability space $(\Omega,\mathcal{A},\mathcal{P})$, where Ω is the set of outcomes, $\mathcal{A}$ the σ-algebra of events and $\mathcal{P}$ the probability measure. Each random variable $z_i(\omega)$, for $\omega \in \Omega$, has its PDF $p_i : \Gamma_i \longrightarrow [0,1]$. Then the joint probability density of the random vector $z=(z_1,\ldots,z_D)$ is:

$$p_z = \prod_{i=1}^{D} p_i \tag{2.59}$$

in the domain:

$$\Gamma = \prod_{i=1}^{D} \Gamma_i \tag{2.60}$$

Let $L_z^2(\Gamma)$ be defined as weighted function space with the inner product

$$\langle a,b \rangle_z = E[a \cdot b] = \int_\Gamma a(z)b(z)p_z dz, \quad \forall a,b \in L_z^2(\Gamma) \tag{2.61}$$

and the norm

$$||a||_z = \sqrt{E[a^2]} = \left(\int_\Gamma a^2(z)p_z dz \right)^{1/2} \tag{2.62}$$

The system of equations $L^s(x,t,u,z)=0$ can be solved with a deterministic solver without capturing the parametric uncertainty. However, to determine the uncertainty, the solution $u(x,t,z)$ can be approximated by means of the the generalized polynomial chaos expansion:

$$u(x,t,z) \approx \tilde{u}(x,t,z) \sum_{i=0}^{N_p} = c_i(x,t)\Phi_i(z), \tag{2.63}$$

where $c_i(x,t)$ are Fourier coefficients and $\Phi_i(z)$ multivariate orthogonal polynomial with respect to p_z. N_p+1 is the number of total polynomial terms i included in the expansion. The number of expansion terms N_p can be calculated with:

$$N_p = \binom{M+D}{D}, \tag{2.64}$$

where M is the order of the final resulting polynomial.

	probability distribution	standardized orthogonal polynomials	Support
Continous	Gaussian	Hermite	$(-\infty, \infty)$
	Gamma	Laguerre	$[0, \infty]$
	Beta	Jacobi	$[0, 1]$
	Uniform	Legendre	$[0, 1]$
Discrete	Poisson	Charlier	$0, 1, 2, \ldots$
	Binomial	Krawtchouk	$0, 1, \ldots, N$
	Negative Binomial	Meixner	$0, 1, 2, \ldots$
	Hypergeometric	Hahn	$0, 1, \ldots, N$

Table 1: Some univariate probability distributions and their corresponding standardized orthogonal polynomials, taken from Xiu and Karniadakis [37]

Orthogonal Polynomials

By choosing orthogonal polynomials, the basis of the solution space will have the smallest possible dimensions. For most of the univariate probability distributions exist well-known standardized orthogonal polynomials defined in the Askey scheme [37]. All common pairs are listed in table 1 including some discrete distributions. If the orthogonal polynomial correspondents are unknown, they can be constructed e.g. with the Discretized Stielte's Procedure [18].

A multivariate orthogonal polynomial $\Phi(z)$ can be obtained by re-arranging the tensor product of basic orthogonal polynomials corresponding to $z_1 \ldots z_D$, where only terms of order less or equal to M are considered. For enhanced handling the terms are arranged with Graded Reverse Lexicographical Notation [35]. The procedure of creating $\Phi(z)$ will be illustrated by the following example:

The bivariate random vector $z = (z_1, z_2)$ with Normal distributed $z_1 \sim N(0, 1)$ and $z_2 \sim N(0, 1)$ is assumed.
For each z_i there is a set of orthogonal Hermite polynomials:

$$\begin{aligned} z_1: &\quad H(x) = 1,\ x,\ x^2 - 1,\ x^3 - 3x, \ldots \\ z_2: &\quad H(y) = 1,\ y,\ y^2 - 1,\ y^3 - 3y, \ldots \end{aligned}$$

The Tensor product of the Hermite polynomials $H(x) \otimes H(y)$ is:

$$H(x) \otimes H(y) = \begin{bmatrix} 1 & x & x^2 - 1 & x^3 - 3x & \cdots \\ y & xy & (x^2 - 1)y & (x^3 - 3x)y & \\ y^2 - 1 & x(y^2 - 1) & (x^2 - 1)(y^2 - 1) & (x^3 - 3x)(y^2 - 1) & \\ y^3 - 3y & x(y^3 - 3y) & (x^2 - 1)(y^3 - 3y) & (x^3 - 3x)(y^3 - 3y) & \\ \vdots & & & & \ddots \end{bmatrix}$$

The corresponding multi-indices $(index_{H(x)}, index_{H(y)})$ are written in matrix form:

$$\begin{bmatrix} (0,0) & (1,0) & (2,0) & (3,0) & \cdots \\ (0,1) & (1,1) & (2,1) & (3,1) & \\ (0,2) & (1,2) & (2,2) & (3,2) & \\ (0,3) & (1,3) & (2,3) & (3,3) & \\ \vdots & & & & \ddots \end{bmatrix}$$

Using the Grevelex notation the multi-indices are ordered in an ascending way following a master index $a = \sum_{k=0}^{D}$ multi-index$_k$. In this way the orthogonal polynomials $\Phi_{(iH(x),iH(y))}$ can be denoted by a single index i. Thus the polynomial chaos expansion can be expressed using single indices for Φ_i.

a |	0	1		2			3			
multi-index	$(0,0)$	$(1,0)$	$(0,1)$	$(2,0)$	$(1,1)$	$(0,2)$	$(3,0)$	$(2,1)$	$(1,2)$	$\cdots$
single index i	0	1	2	3	4	5	6	7	8	$\cdots$

The polynomials in the tensor product can now be set in order to the corresponding single indices, and the resulting orthogonal polynomials $\Phi(z)$ are:

$$\Phi(z) = 1,\ x,\ y,\ x^2-1,\ xy, y^2-1,\ x^3-3x,\ (x^2-1)y,\ x(y^2-1),\ y^3-3y, \ldots$$

To approximate the solution $u(x,t,z)$ with the gPCE, the coefficients c_i have to be identified. The Fourier coefficients are defined as

$$c_i = \frac{\langle u, \Phi_i \rangle_{p_z}}{||\Phi_i||^2_{p_z}} = \frac{E[u \cdot \Phi_i]}{E[\Phi_i^2]} = \frac{\int_\Gamma u \Phi_i p_z dz}{\int_\Gamma \Phi_i^2 p_z dz} \tag{2.65}$$

The coefficients can be approximated with Stochastic Collocation Method $(c_i \approx \tilde{c}_i)$ following three steps in principle [35]:

1. Choose K collocation nodes selected for the joint probability density p_z
2. Solve the deterministic system $L^d(x,t,\tilde{u}_k, Z_k) = 0$ for each $k \in [1, \ldots, K]$
3. Evaluate the coefficients $\tilde{c}_i$ based on the solutions $U_K = (\tilde{u}_1(x,t,Z_1), \ldots, \tilde{u}_K(x,t,Z_K))$ (from step 2.)

$$c_i \approx \tilde{c}_i = (\Theta^T \Theta)^{-1} \Theta^T \tilde{u} \tag{2.66}$$

where

$$\Theta_{ik} = \Phi_i(Z_k) \text{ for } i \in [0, N], k \in [1, K]$$

The Stochastic Collocation Method evaluates the c_i coefficients based on the solution of samples i.e solving $L^s(u, x, t, z)$ for a certain number of sample nodes K. By inserting the deterministic values $z = Z_k$ at each collocation node K into L^s, the system becomes deterministic $L^s \rightarrow L^d$. Thus, L^d can be solved with any regular deterministic solver for partial differential equations, disregarding stochastic calculus.

In order to choose the collocation nodes, various approaches exist, the sparse grid collocation is the one mainly used [36]. Sparse grid collocation is based on the tensor product of univariate collocation schemes, however, only a subset of the full tensor grid is considered. The basis for the tensor product are Clenshaw Curtis nodes over Γ.

After the evaluation of the expansion coefficients $\tilde{c}_i$ with sparse grid collocation, the gPCE can be constructed reconsidering equation 2.63:

$$u(x,t,z) \approx \tilde{u}(x,t,z) = \sum_{i=0}^{N_p} \tilde{c}_i \Phi_i(z), \quad \text{recap eq. (2.63)}$$

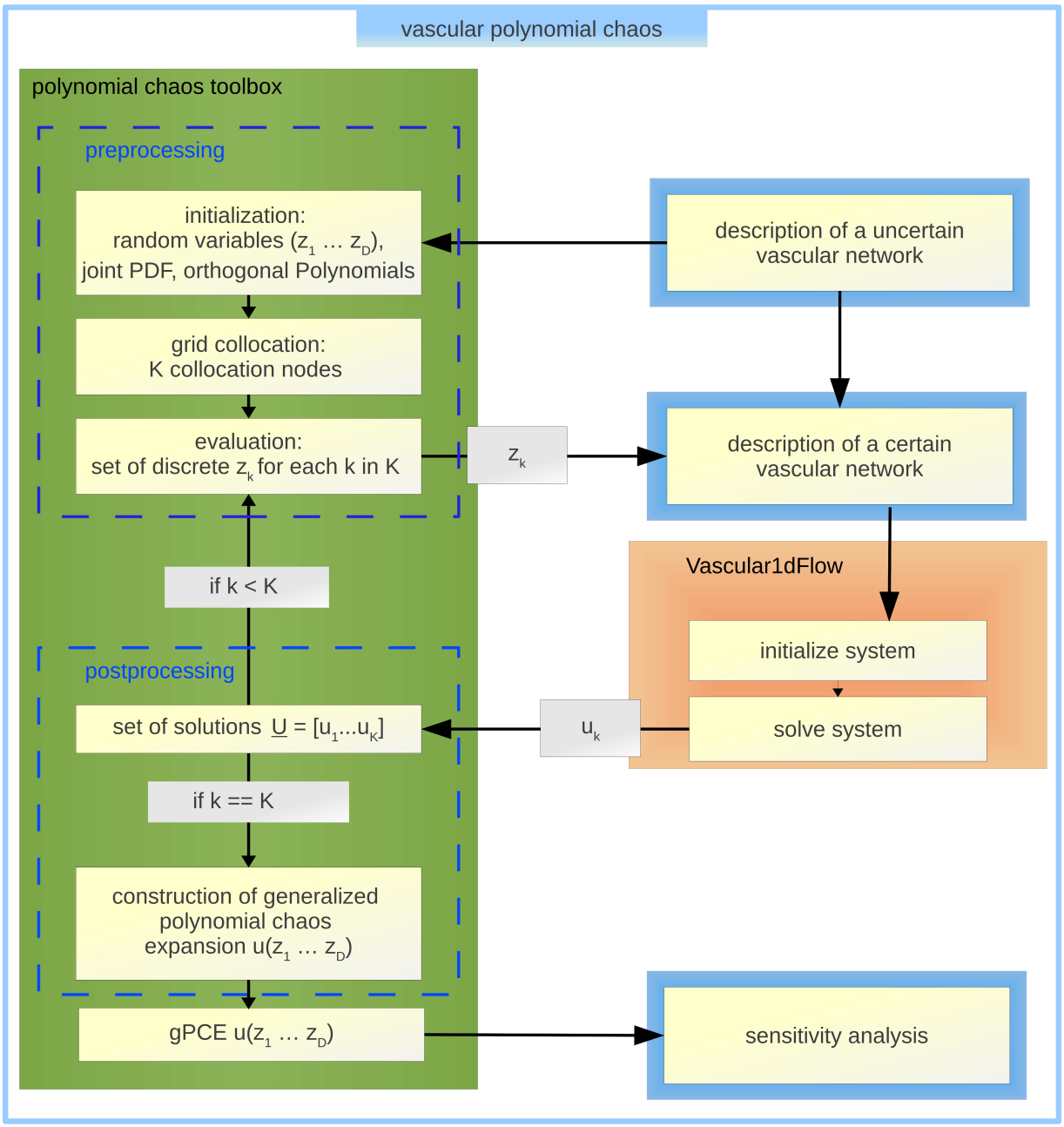

Figure 3: The basic process schema of *VPC*, coupling two frameworks vascular1DFlow and polynomial chaos toolbox. All blue highlighted process parts belong to *VPC*.

3. Elaborated Methods and Implementations

3.1. Vascular Polynomial Chaos (VPC)

For the purpose of simulating vascular networks with uncertain model parameters the *vascular polynomial chaos* (VPC) model has been designed. It combines the two frameworks vascular1DFlow and polynomial chaos toolbox with a periphery for vascular network and solution data handling. In addition, VPC carries out sensitivity analysis after the gPC is performed. As both vascular1DFlow and polynomial chaos toolbox are written in $python^{TM}$[5], both frameworks are merged seamlessly using the same programming language for VPC.

The basic approach of VPC is straight forward, illustrated in figure 3. Assuming, a description of a vascular network with D uncertain parameters $(z_1, \ldots, z_D)$ is given in a processable from (further information in section 3.2.1).

Let $L^s(x,t,u,z) = 0$ be the equation system of vascular1DFlow (2.17) with system variable $u(x,t,z) = (P(x,t,z), Q(x,t,z), A(x,t,z))^T$. Besides the coordinate x and time t, L^s is dependent on the D-variant random vector, containing the stochastic parameters of the network $z = (z_1, \ldots, z_D)$.
L^s is a stochastic system of partial differential equations. Its solution $u(x,t,z)$ is approximated in terms of the generalized polynomial chaos gPC with a polynomial chaos expansion (gPCE) of order M:

$$u(x,t,z) \approx \sum_{i=0}^{N_p} \tilde{c}_i \Phi_i(z), \quad N_p = \binom{M+D}{D} \quad \text{recap eq. (2.63)}$$

As a first step, the preprocessing of polynomial chaos toolbox, the orthogonal polynomials $\Phi_i(z)$ are identified, combining orthogonal polynomials that correspond to the distributions $(z_1, \ldots, z_D)$ (2.2.2). Furthermore, sparse grid collocation is used to determine K collocation nodes with corresponding values of $\mathbb{Z}_K = (Z_{k1} \ldots Z_{kD})$.

In a second step, the evaluation process, the solutions $U_K = (\tilde{u}_1(x,t,Z_1), \ldots, \tilde{u}_K(x,t,Z_K))$ required for the construction of the expansion coefficients are determined. This is done iteratively for each collocation node $k \in K$. The deterministic values Z_k are assigned to the uncertain network description, resulting in a certain network description. This description is passed to vascular1DFlow, which solves the now deterministic equation system $L^d(x,t,\tilde{u}_k,Z_k) = 0$ and returns the solution $\tilde{u}_1(x,t,Z_k)$.

In a third step, the post processing of the polynomial chaos toolbox, the expansion coefficients $\tilde{c}_i$ are evaluated using the resulting solutions $U_K = (\tilde{u}_1(x,t,Z_1), \ldots, \tilde{u}_K(x,t,Z_K))$. Then the gPCE is constructed using orthogonal polynomials Φ_i and evaluated expansion coefficients $\tilde{c}_i$.

In a last step, the post processing of VPC, the resulting approximated solution is used for sensitivity analysis of the parametric uncertainty in the vascular network.

[5] http://www.python.org

In the basic approach, the gPCE is constructed for the given solutions U_K consisting of $(\tilde{u}_1, \ldots, \tilde{u}_K)$, which are the solutions of the evaluation at each collocation node. In general, the solution $\tilde{u}$ calculated by vascular1DFlow is defined for each vessel in form of three matrices, one for each primary variable P,Q and A. Each matrix takes for each quantity the form:

$$u(q)_{nt} = \begin{bmatrix} q_{10} & \cdots & q_{1T} \\ \vdots & \ddots & \vdots \\ q_{N0} & \cdots & q_{NT} \end{bmatrix}, \tag{3.1}$$

where

$q \in P, Q, A$
$t \in [0, T]$ with T = total time
$n \in [1, N]$ with N = number of grid points

The solution of one quantity at a certain grid node of a vessel over time, i.e one line in the matrix (equation 3.1), is referred to as the signal S(t) of the quantity; P(t),Q(t) and A(t) respectively.

The solution $\tilde{u}_k$ of one collocation evaluation contains the three quantity matrices of each vessel in the network. Recapitulating, the expansion coefficients $\tilde{c}_i$ of gPCE are a function of x and t whereas Φ depends on z. As the solution of vascular1DFlow consist of matrices with discrete values for each grid node and time point, x and t respectively, the expansion coefficients $\tilde{c}_i$ take on the same matrix form. This means, for each time point at each node, a gPCE dependent on the uncertain parameters is created. *E.g. a network with five vessels at ten grid nodes and 300 time points would have the corresponding number of* $N_{Poly} = (5 * 10 * 300) * 3 = 45000$ *polynomials (gPCEs)*.

Implementing the basic approach as described above does not lead to a feasible program due to two problems listed below. However, the basic structure and proceeding described is correct and implemented in a slightly different way (see figure 4).

Problems of the basic approach:

- The data size of total collected deterministic solution data quickly reaches the limit of processable computer memory size.
  [NB: even for small networks as the first test case 4.1 the size of all collected data goes up to several gigabytes.]

- Uncertainty in some model parameters affects indirectly the simulation parameter Δt. This results in a different time-sampling rate of the solution signals, i.e. the number of time points of the signals can vary for each gPC evaluation. Hence the solution values in the signals of different evaluations do not match to each other. The gPCE coefficients can therefore not be constructed correctly.

Additional the basic approach quickly reaches its limits regarding data handling and sensitivity analysis:

- Uncertainty analysis is mostly focused on a few measuring points in some branches of the vascular network. The computational cost can be decreased by proceeding the construction of the gPCE only for these specific grid nodes.
- The possibility of processing the P,Q and A signals, in terms of *e.g. peak detection or (linear-) wave splitting*, would lead to a more advanced and improved result of the uncertainty analysis.
- A different simulation aspect/parameter than the solution signals might be focus of the uncertainty analysis, *e.g. the deformation of the wall over the length of a branch*. These parameter values need to be extracted separately.

The limitations of the basic approach are bypassed by refining the process with three cascades. Splitting the evaluation process i.e. running deterministic simulations with vascular1DFlow and constructing the gPCE, is the main idea behind the cascade approach. The cascade process is illustrated in figure 4.

After initialising the uncertain vascular network and gPC, the evaluation process is carried out in the first cascade. The simulation results of vascular1DFlow are saved after each evaluation to the hard disk drive (HDD). Thus, the solution data stays not longer than necessary in the computer memory.

In the second cascade, the solution data is preprocessed and filtered in the way needed for the current uncertainty analysis, including unification of signal lengths. Afterwards the gPCE is constructed from the preprocessed data. The preprocessed data and its resulting gPCE are saved to HDD, as well.

In the last cascade, the sensitivity analysis based on the calculated gPCE is performed.

Saving data to HDD between the cascades economises memory and creates backup data which can be used later on. In the VPC, the evaluation of the deterministic simulations takes the most time. As the solution data of vascular1DFlow generated during the evaluation process is saved, it can be loaded (completely or partially) for preprocessing as often as required. The same data can be used multiple times without running the costly evaluation process again, if *e.g. new preprocessing methods are available or a change in investigation purpose or investigation node in the network arises.*

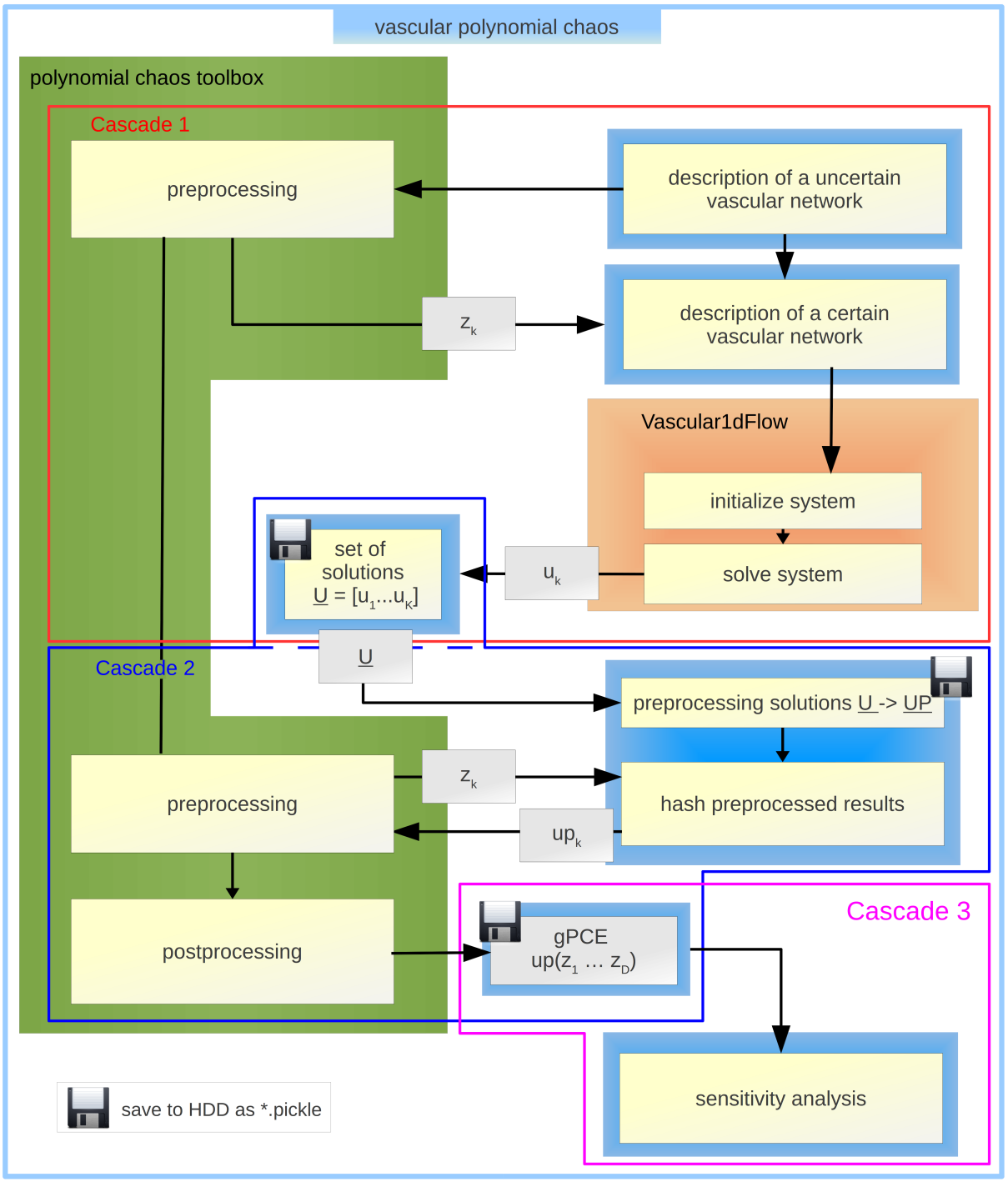

Figure 4: The implemented process schema of *VPC*. Refining the basic process schema (figure 3) into a cascade process.

3.2. Virtual Representation of a Vascular Network

For the simulation, a virtual representation of the network model data is required. In the current version of vascular1DFlow, model data of vascular networks are defined directly in the *Main-file* of the framework as python-code. For small vascular networks and test cases with regards to verification of vascular1DFlow, this is a practical approach.

In the process flow schema of VPC (figures 3 and 4) the model data of a certain and uncertain vascular network is indicated as 'network description'. As illustrated in the flow schemas, the network description is adapted in each gPC evaluation, applying the changed parameters Z_k. In order to do so, ia more flexible network description than so far implemented is required. This goes hand in hand with the need to enhance the definition of large networks. Furthermore, the possibility to load and save network descriptions from separate files would increase the convenience of the frameworks.

3.2.1. Offline and Online Description

In the new approach, the online-description *(during program runtime)* and offline-description *(stored on HDD)* of a vascular network are separated. For the online-description an object oriented data structure, suited for the vascular1DFlow and VPC was elaborated. It is based on two classes; $<$classVascularNetwork$>$ and $<$classVessel$>$. The offline-description is based on XML, in which all vascular network data is placed in a specific manner. The XML-file of the first test case (section 4.1) can be found in the appendix A.2

The online-description of a particular vascular network is accomplished by creating instances of the two classes after parsing through its offline-description (figure 5).
One $<$classVascularNetwork::instance$>$ forms the basis of each online-description of a particular network. The instance provides data of boundary conditions *(e.g. terminal reflection coefficients)*, fluid parameters *(e.g. blood density, viscosity)*, the simulation context *(e.g. total time, CFL)* and references to vessels of the network. Each vessel of the vascular network is defined as individual $<$classVessel::instance$>$.

The structures of the offline and online descriptions are due to XML and the object oriented approach the same for all vascular networks. Hence, the potential of automation increases *e.g. applying changes in vessel data during the gPC evaluation*. Additionally, several vascular networks can be handled and processed online at the same runtime.

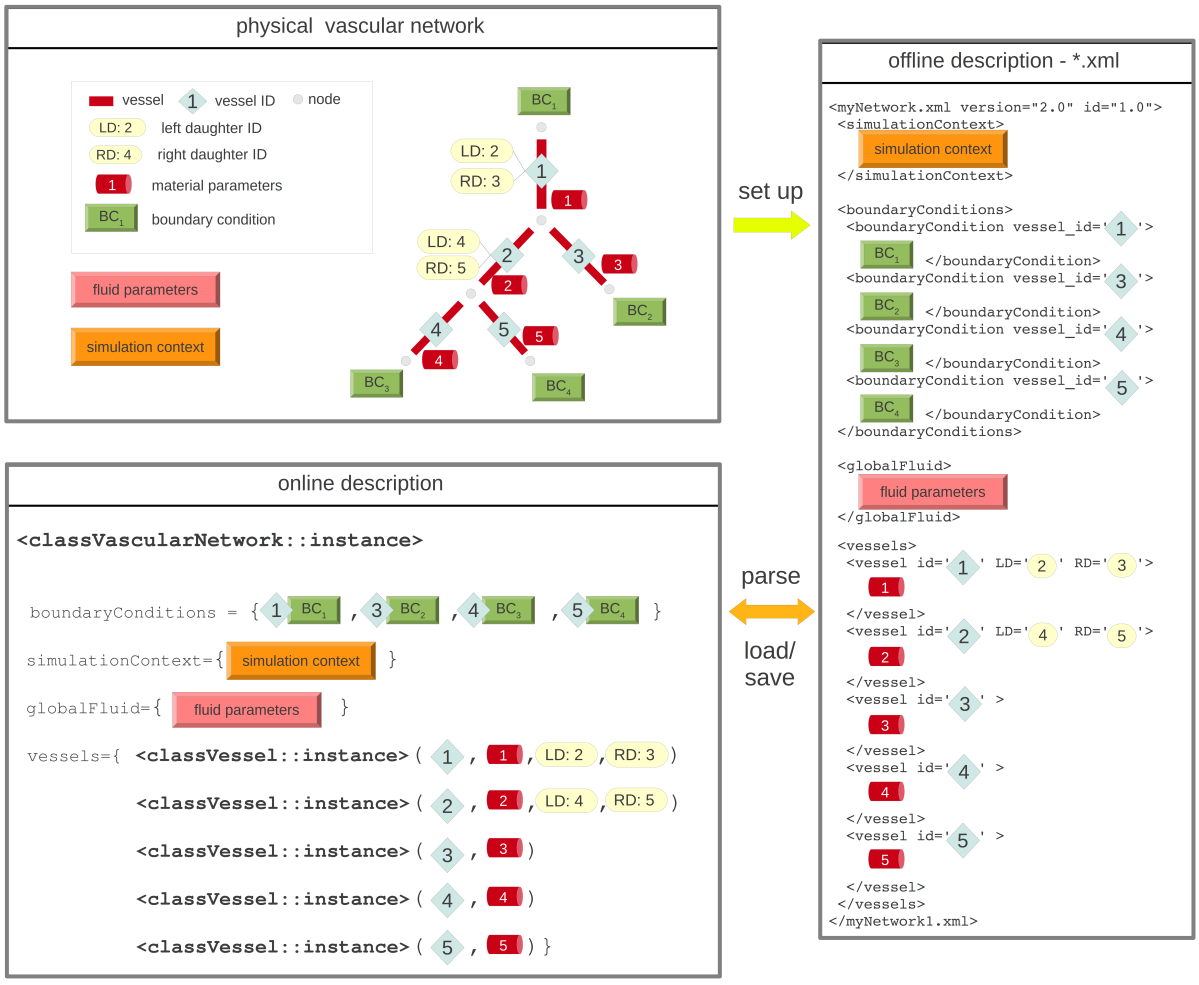

Figure 5: Principle data flow of the implemented network description. The offline description is created form a physical network. With the moduleXML the online description can be constructed and transferred to VPC or vascular1DFLow.

To stream data from the offline-description to the online-description the **moduleXML** was implemented. To enhance convenience, this module contains some special features. The unit of each parameter can be defined with the $<..$ *unit=' '*$>$ - tag. While parsing, parameter values are converted automatically into SI units based on the unit-tag. Parameter values can include mathematical operators, among others $+, -, *, /, \sqrt[x]{}, ^x, exp()$. The expressions are evaluated and executed while creating the online-description. Both features are shown in the XML-example in figure 6.

Once the vascular network is 'online' it can either be solved with vascular1DFlow or directed to *VPC* for uncertainty analysis. To ensure compatibility for both frameworks, each parameter can be defined 'offline' with certain and uncertain values. Certain values are defined as $<$*scalar unit="*$>$ *value* $<$ *scalar*$>$. When directing data to vascular1DFlow, only

these values are taken into account. Uncertain data is assumed to be uniformly distributed, in a fixed range. Hence a value $<$*interval*$>$ is sufficient to describe the uncertainty. In the XML-example (figure 6) this is highlighted for the proximal radius of a vessel.

VPC recognises all uncertain parameters by the defined interval. Based on the interval values, continuous random variables $(z_1, \ldots, z_D)$ and the D-variant random vector $z = (z_1, \ldots, z_D)$ are created. The distinct values $\mathbb{Z}_k = (Z_{k1} \ldots Z_{kD})$ of each *gPC* evaluation are assigned to its $<$scalar$>$ correspondence. Thus, the certain network description is adapted and processable for vascular1DFlow. The procedure is fully automated. Merely the definition of an uncertain parameter in the offline description is needed to perform a uncertainty analysis with *VPC*.

```
XML file:
   ..
   <radiusA>
       <scalar unit = 'mm'> 6.0/2 </scalar>
       <interval unit = 'mm'> 2.0 4.0 </interval>
   </radiusA>
   ...

<classVessel::instance>:
   ..
   radiusA = 0.003                  # SI [m]
   radiusAinterval = [0.002,0.004]  # SI [m]
   ...
```

Figure 6: XML example code for defining certain and uncertain values for the proximal radius of a vessel and the the resulting variables in the online-description after parsing the XML file

3.2.2. Network Topology

In vascular1DFlow, the vascular system is regarded as a tree of connected vessels. Vascular systems branch with bifurcations only, i.e. each connecting point connects two or three vessels. To describe the topology of the tree several approaches are possible. In vascular1DFlow a node description is used. In addition to this, the mother-daughter description is included in the new network descriptions (figure 7).

In both descriptions, each vessel is identified with a specific vessel-ID.

The **Node description** sets the vessels in relation based on the connection points (figure 7(a)). Each connection point is therefore labelled with a specific node-ID. Each vessel has a start and an end node. If the start node of a vessel corresponds to the end node of another vessel, it means they are connected. For each vessels three pieces of information are necessary to describe the topology (see table 2).

The **Mother-daughter description** does only use the vessel-IDs to describe the topology (figure 7(b)). The three vessels forming a bifurcation are often described with the parent-child or mother-daughter relationship, where the proximal vessel is called mother and the two branches are the daughter vessels. The structure of the tree can be described by this relation. In addition to its own vessel-ID each mother vessel 'knows' the vessel-IDs of its daughter vessels. To differentiate the daughters they are defined as the 'left' and the 'right' branch. In case of a simple connection of only two vessels, the vessel downstream is defined as a 'left' daughter of the upstream 'mother' vessel. For each vessel the vessel-IDs and all daughter-IDs if existent are necessary to describe the topology (see table 3).

The mother-daughter description has some advantages over the node descriptions, among others:

- No additional information (node-IDs) and therefore less information in total is needed to describe the network topology (see tables 2 and 3).
- All connections are per definition either vessel to vessel connections or bifurcations. Thus, no connection test to identify multiple branching is required.
- The location of all branches is clearly defined with the 'left'- and 'right'-tag. Figure 8 shows possible alterations of the example network (figure 7(a)) only possible using the node description.

Due to its advantages, the mother-daughter relation is implemented and used in $<$classVascularNetwork$>$ (section 3.2.1), vascular network creator (section 3.3) and for the 3D visualisation (section 3.7).

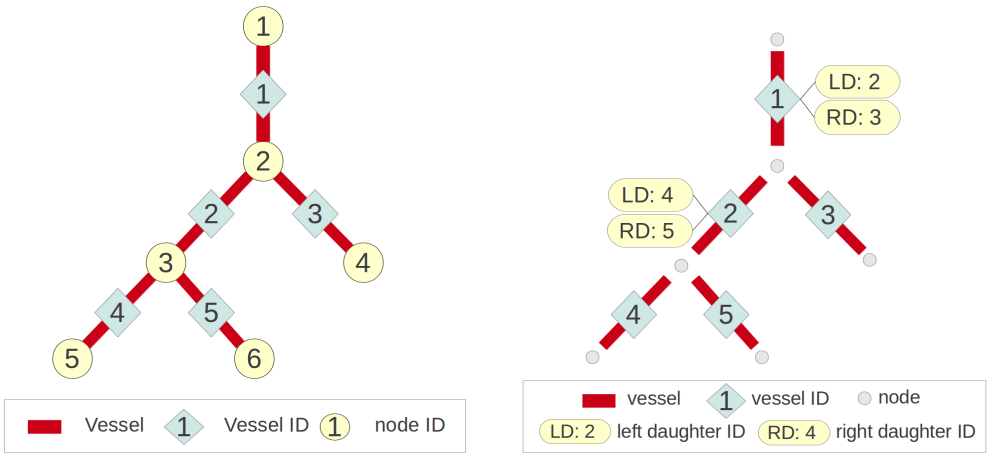

(a) node description

(b) mother-daughter description

Figure 7: Example of a vascular network specified using 7(a) the node description and 7(b) the mother-daughter description

ID	start node	end node
1	1	2
2	2	3
3	2	4
4	3	5
5	3	6

Table 2: Data required to specify the example network in figure 7(a) with the node description

ID	left daughter	right daughter
1	2	3
2	4	5
3		
4		
5		

Table 3: Data required to specify the example network in figure 7(b) with the mother-daughter description

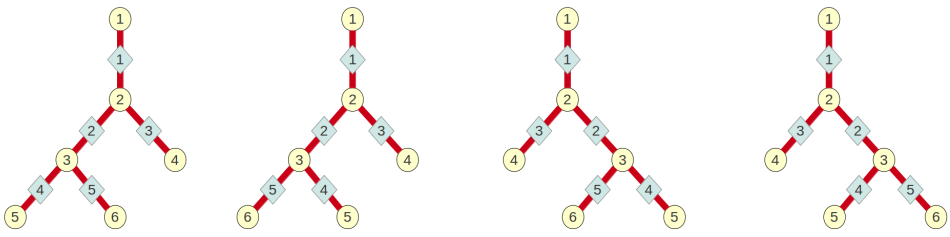

Figure 8: Possible alterations of the tree structure of the example network in figure 7(a), using the node description

3.3. Vascular Network Creator - vnc

With the choice of XML, the data of vascular networks is available on HDD in human and machine readable files. Specific network files can be created by completing a XML-template file with given experimental data. However, for the more convenient generation of vascular networks, the python program **vascular network creator (vnc)** has been created. The program has a text based menu embedded in the Unix/Linux console window. The topology of the current network is shown in a second window using the dot language from Graphviz [6] via the pydot [7] interface. Basic functions include adding and deleting of branches. Boundary conditions can be applied to the peripheral vessels. Created networks can be saved to HDD and loaded into the program from XML. However, large data sets are most convenient to organize and handle in tables and spreadsheets *e.g.with Calc of LibreOffice* [8] . Thus vnc includes bindings to load vessel data from CSV files: the **moduleCSV**. The vessel data can be saved as CSV in the spreadsheet program which then is read out by the moduleCSV and passed to vnc. For fast update of offline descriptions (xml) from csv files, vnc includes an update method, which updates the XML file from the CSV.

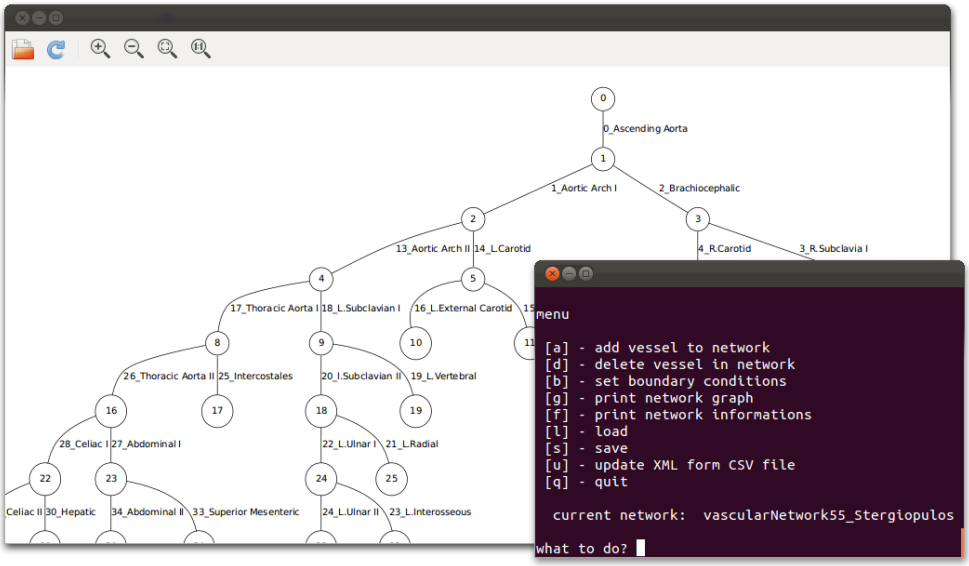

Figure 9: **vnc - vascular network creator**: The menu in the console window is used for generating offline descriptions of vascular networks. The topology of the current network is shown in a separate window.

[6] http://www.graphviz.org/Home.php
[7] http://code.google.com/p/pydot/
[8] http://www.libreoffice.org/features/calc/

3.4. Saving Data to HDD

Simulation results, preprocessed data and the gPCE's are saved to HDD using the python module Cpickle[9]. The module provides an algorithm for the conversion of python objects into series of bytes. Cpickle is written in C instead of python, which increase the speed of the module. Using Cpickle the data structure of the saved data remains the same and no arranging after reloading is needed. During the evaluation process each simulation solution is saved in a well defined standardized manner. Solutions from deterministic simulations run directly with vascular1DFlow are saved in the same form. Thus all post processing methods *e.g. the 3D Visualisation (section 3.7)* are able to process them. The simulation solution is defined as:

```
simulationSolution = [dataSet, dataSet2 ...]
dataSet = { 'Pressure' :  pressureData,
            'Flow'     :  flowData,
            'Area'     :  areaData,
            'waveSpeed':  waveSpeedData,
            .. }
```

3.5. Preprocessing of the Solution Data

In the second cascade of VNC, the solution data of the evaluation process U_K is preprocessed, before the gPCE is constructed (see section 3.1). The preprocessing is conducted in four steps:

1. Select all required solution signals for the user defined investigation points
2. Unify the length of signals corresponding to an investigation point
3. Conduct wave splitting of the signals in forward and backward propagating waves
4. Find local and global extrema of the unified and segregated signals

For each investigation point, several gPCE are created for each quantity P,Q and A; one for the signal itself, on for the forward and backward contribution and one for each extrema in every signal. The methods and algorithm applied in steps 2 - 4 are explained in the following sections.

[9] http://docs.python.org/library/pickle.html

3.5.1. Recasting Signals to Unify the Signal Lengths

The solutions signal length of different collocation evaluations can vary. This occurs due to some model parameters influence on the wave speed c_o (equation 2.14), according to the chosen compliance model (see section 2.1.1). The time step is determined before each evaluation simulation using c_o and the CFL-condition (section 2.54). Thus the time step vary proportional to c_o. As discussed in section 3.1 equal numbers of time points are required for the calculation of the gPCE coefficients. This is ensured by unification of the signals lengths of each investigation point with the following algorithm:

1. Find the signal with minimal length L_{min}
2. Create a time vector $\tilde{t}_{min} = [0, \ldots, totalTime]$ with the length L_{min}
3. Interpolate all signals whose length exceeds L_{min} proceeding the following steps
   a) Create a straight spline fit[10] connecting all points of the signal as a function of t
   b) Recast the signal by inserting the time vector $\tilde{t}_{min}$ into the spline fit function
   c) Overwrite inappropriate signal with the unified signal

Vascular1DFlow is explicit and thus the time step is usually very small (around 1-5 ms) which results in signals with 200-1000 time points per second. In the verification test cases (section 4.1.4), the signal lengths vary about ± 10 per 500 time points. Thus interpolation of the signals is quantitatively small, and the accuracy is ensured.

3.5.2. Separation in Forward and Backward Contributions

The linear or non linear wave splitting is conducted as explained in section 2.1.4 and 2.1.5. First the characteristic impedance Z_c of the vessel or the Riemann invariants and the impedances Z_1 and Z_2 are determined, depending on whether linear or the non linear wave splitting is conducted. Then, the the ΔQ_f, ΔQ_b, ΔP_f and ΔP_f signals are calculated. *[NB: denoted as S in the following.]* The ΔS signals represent the change of the separated signals S from one time point to the next one. The signal S for a certain time point t_i can be calculated by the integral from zero to t_i over the Δ-forward and Δ-backward contributions, respectively. As the signals consist of discrete values, the integrals can be rewritten as summations:

$$P_{f\,i} = \sum_{j=0}^{i} \Delta P_{f\,j} \quad , \quad P_{b\,i} = \sum_{j=0}^{i} \Delta P_{b\,j} \tag{3.2}$$

$$Q_{f\,i} = \sum_{j=0}^{i} \Delta Q_{f\,j} \quad , \quad Q_{b\,i} = \sum_{j=0}^{i} \Delta Q_{b\,j} \tag{3.3}$$

[10]The packages numpy (http://numpy.scipy.org/) and scipy (http://scipy.org/) are used for spline fitting

The four summations (equations (3.2) and (3.3)) can be calculated numerically with different approaches. A benchmark test of several methods including the applied one, is described in section 3.8.2. After the summations are calculated, the wave separation is completed.

3.5.3. Global and Local min and max Function

The fourth step of the preprocessing in VPC is the evaluation of the local and global extrema.

Finding local and global minima and maxima of a signal defined as a set of discrete values is non a trivial task for computer algorithm. Evaluating extrema with linear algebra i.e differentiating the signal with respect to t and finding zero-crossings, is only applicable after fitting the discrete signal with a spline. It was found, that this method gives poor results for the pulse and flow signals of the example test cases.
Another algorithm, originally written in Matlab by Billbauer[11] and converted to python[12], is applied in a modified version instead. The algorithm traverses a given signal and checks each point for extrema conditions. An extrema is defined as a point with sign change in gradient and whose y-value is at least ξ_y distant to the neighbouring extrema. ξ_y is used to filter small perturbations due to noise out of the given signal. The basic principle of the algorithm is:

1. *[Modification]* Detect if first peak is minimum or maximum. This modification replaces a user input parameter of the original function.

2. *[Original]* Traverse signal until a point (x_{e1}, y_{e1}) with sign change in gradient is detected. Proceed traversing the signal and check the following points (x_i, y_i). The decision whether (x_{e1}, y_{e1}) is an extrema is determined by the following conditions:

   a) *[Original]* if $y_{e1} - \xi_y > y_i$ for maxima or $y_{e1} + \xi_y < y_i$ for minima, respectively, then (x_{e1}, y_{e1}) is extrema. Save extrema and return to step 2

   b) *[Original]* if another point with sign change in gradient (x_{e2}, y_{e2}) is detected before condition a.) holds true, then both (x_{e1}, y_{e1}) and (x_{e2}, y_{e2}) are not extrema. Return to step 2

3. *[Modification]* Return all minima and maxima in the form: [x values],[y values].

[11] http://billauer.co.il/peakdet.html
[12] https://gist.github.com/250860

3.6. Sensitivity Analysis

The sensitivity of the simulation result on a uncertain parameter is defined as the relative change of occurrence time and amplitude of pressure and flow waves at a certain point in the network due to this uncertain parameter.

Total and partial sensitivity measures
For the sensitivity analysis, the expected value (equation 2.55), STD (equation 2.57) and the 100(1-α)%-confidence intervals (equation 2.58) are used as sensitivity measures. These sensitivity measures, are calculated from the constructed gPCEs with methods provided by the polynomial chaos toolbox. The expected values and the STDs are on one hand calculated taking all uncertain parameters into account ($\mathbb{E}_T = E[gPCE(z_1, z_2, ...z_D)]$).
[NB: denoted as total expected values and total STD]
On the other hand, to evaluate the sensitivity of one specific uncertain parameter, the expected values, STDs and confidence intervals are calculated for each uncertain parameter separately. *[NB: denoted as partial expected values/STD]*
This is done by inserting the mean values of all other uncertain parameters into the gPCE. The gPCE is transformed into a partial gPCE* representing the variability of the solution due to the specific parameter *(e.g.* $\mathbb{E}_1 = E[gPCE(z_2 = E[z_2], ...z_D = E[z_D])]$*).* The partial sensitivity measures can be calculated from the gPCE* in the same manner as before. To evaluate the sensitivity of the uncertain parameters, the total and partial sensitivity measures are compared.

Analysis of the Total Signals
The sensitivity measures can be calculated for the total pressure and flow signals. The expected values and the STD of the total signal can give an overview of the variability of the uncertain solution (figure 12). However, the change in occurrence time and the change in amplitude can not be analysed, as these effects are mixed. Furthermore, the plots are sometimes demanding to interpret especially the STD plots (figure 12(b)).

Analysis of the Signal Peaks
To analyse both effects (i.e. change in amplitude and occurrence time) separately, the peaks of the solution signals are detected (section 3.5.3). The peaks of pressure waves are specific points of the signals, which can be recognized easily.
The occurrence times and amplitudes of maxima and minima of the pressure and flow pulses have a fundamental physiologic significance *(e.g. systolic and diastolic pressure in the ascending aorta; see also section 4.2)*.
Two gPCEs, one for the occurrence time and one for the amplitude, are constructed for each signal peak. The resulting gPCEs can be analysed as discussed above, resulting in total and partial expected values and STDs. The sensitivity as defined above is estimated with the total and partial sensitivity measures of the peaks. In figure 10 the total and partial sensitivity measures of a peak are illustrated as box plots. The magnitude of variability, in this case parameter β_2 can be seen clearly, comparing the yellow (total STD) and the blue box (partial STD).

100(1-α)%-Confidence Intervals

Another way to visualize the sensitivity of the parameters are 100(1-α)%-confidence intervals (figure 11). The confidence intervals are calculated for the time and amplitude gPCEs of the extracted peaks. In general, they predict the range in which the peaks appear with 100(1-α)% confidence, running the simulation with these uncertain parameters. The confidence interval can be calculated for each uncertain parameter isolated, just like the expected value and the STD. Thus, one obtains two confidence intervals (one for time and one for the amplitude) for each peak, in dependency of each uncertain parameter. The two confidence intervals can be used to construct a confidence interval line, representing the appearance of the peaks, which is 100(1-α)% likely. The confidence interval lines can be plotted together with the expected values of the total signal. These plots show also in which range the peaks are varying due to the uncertain parameters and it is possible to extract the sensitivity of the signals since stronger variation means higher sensitivity and vice versa. In principle, the confidence interval lines present similar information as the expected value and STD box plots, but they also visualise how large the impacts on the simulation are within 100(1-α)% confidence.

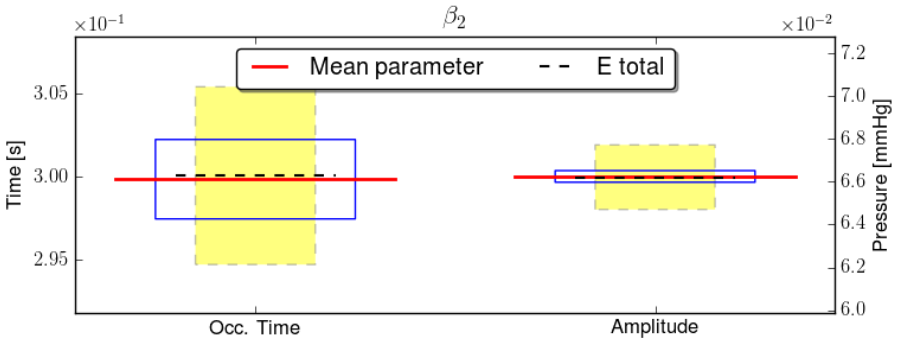

Figure 10: Example box plot with the total and partial sensitivity measures of a pressure peak, from the simulation case I (section 4.1)

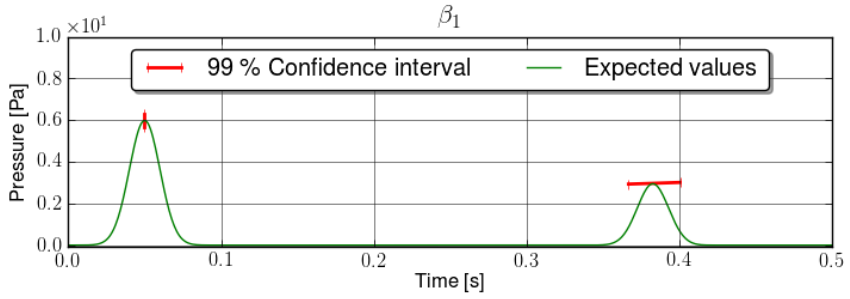

Figure 11: Example confidence interval, showing the prediction of the peak appearance with 99% confidence, due to the parameter β_1, from the simulation case I (section 4.1)

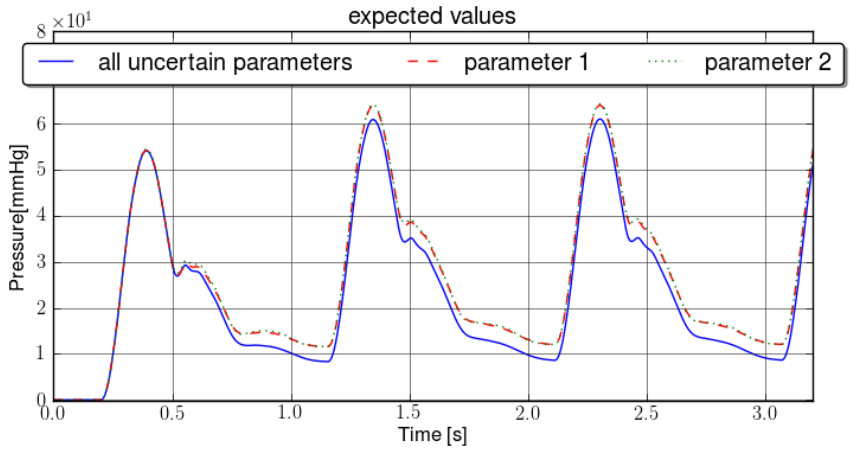

(a)

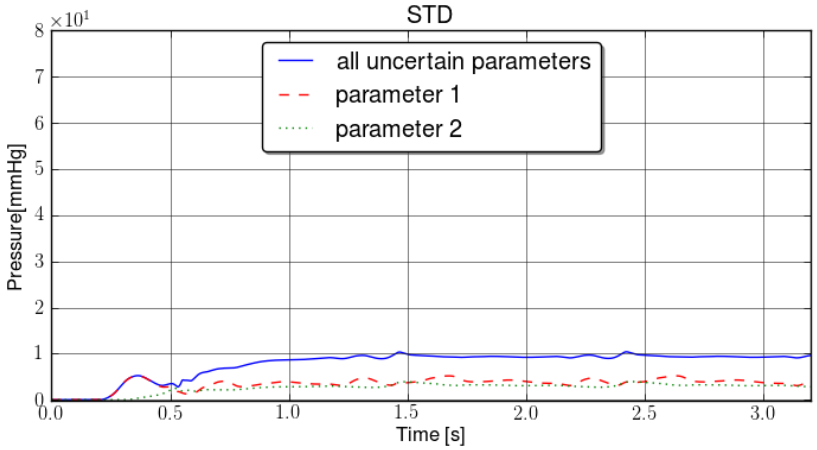

(b)

Figure 12: Example total and partial sensitivity measures, expected values (12(a)) and STDs (12(b)), of a test simulation of the network in case II (section 4.2)

3.7. 3D Visualisation

The appropriate representation of the simulation result in plots and graphics is one fundamental task of the post processing.

It is common to illustrated the solution signals in two dimensional graphs. For vascular1DFlow, the values of a quantity *(e.g. P,Q,A)* can be plotted in two different ways: time-quantity plot for a given grid node or space-quantity plot for one vessel at a given time point. The latter can be easily animated, showing the space-quantity plot over the hole simulation time. The two dimensional plots are created with the matplotlib[13] library.

Despite their accurate and scientific representation of the solution data, 2D graphs have some disadvantages. Arterial networks consists of many branching vessels. With separate two dimensional plots for each vessel, the overview of the system and its solution is quickly lost. For small networks, the 2D graphs may be arranged corresponding to the vessels in the network. However, the possibilities to visualize a total multi-branched network are limited. In addition 2D plots are sometimes not easy to understand for non-scientists.

The disadvantages of 2D graphs are bypassed with the implementation of an advanced 3D visualisation. The object oriented 3D visualisation program is written in python and is based on the library mayavi2[14]. The program creates a 3D representation of a vascular network defined by the previously described online description (section 3.2.1). The solution data of a simulation saved as *.pickle (section 3.4) can be loaded additionally. With the 3D representation the changes over space and time of the solution can be visualized at the same time for the hole network. The dynamics of large networks *e.g. the propagation of pulses from the heart to the periphery and back*, can be studied more conveniently. Furthermore, 2D plots can be opened by selecting a vessel with the mouse cursor (section 3.7.3). Hence, the 3D visualisation program combines the scientific 2D plots with a convenient 3D representation of the network.

3.7.1. Creation of a 3D Representation from 1D Simulation Data

The 3D representation of a vascular network is composed of 3D-vessel representations, corresponding to the data stored in the online/offline description.

Creation of a 3D-vessel

Vascular1DFlow solves the governing equations for blood flow for one dimension, i.e. along the axis of each vessel. Thus, data is only available at the grid nodes of each vessel.
However, the cross-sectional area A is a two dimensional information. From this, the radius of the vessel at each grid point can be calculated, as the areas are assumed to be circular (section 2.1.1). The 3D model of a vessel can be constructed with the length, radius and number of grid nodes N, as a straight vessel. The x-axis of the 3D-vessel corresponds to the x-axis of the vessel in vascular1DFlow, where the same number of grid nodes is located over the same length. At each grid node, a circle consisting of 24 points is constructed in

[13] http://matplotlib.sourceforge.net/
[14] http://code.enthought.com/projects/mayavi/

the yz-plane according to the given radius (figure 13(a)). All circular points are meshed to a surface, representing the 3D-vessel (figure 13(b)).

Visualisation of Scalar Quantities
At each grid node scalar values (1D) of the pressure P, flow Q and velocity $v = Q/A$ are given. The scalar values of a quantity are mapped to a colour array. All circular points of a grid node are coloured with the map-colour corresponding to the grid node quantity (see figure 13(c)). The surface points between the circles are interpolated according to the point values. In doing so, any one dimensional information can be visualized on a three dimensional tube. The quantities and their corresponding colors are displayed in a look up table (LUT) in the visualisation window. The mapped quantity can be changed by a key stroke during the visualisation runtime.

Creation of a 3D model of the Vascular Network
The network given by a network description is created by parsing through the tree defined with the mother-daughter relation. For each vessel, the vascular representation is created and positioned in reference to its mother. As the mother-daughter relation states the relative positioning of the daughters, no additional information for the position is needed (section 3.2.2). However, as the branches at a bifurcation are angled, one additional parameter is required. The angle between the mother and daughter axis becomes therefore an additional vessel property, defined in the online and offline description. However, if there is no angle given, it is assumed to be 30 degree.

3.7.2. Unsteady 3D Visualisation

A 3D representation of a vascular network is created by the proceeding explained before. It is created with the initial condition given within the solution data. To visualize an unsteady simulation, the 3D representation is visualized for every time step in the simulation data set (section 3.4). The visualisation time step is defined as 1/33 s (i.e. 33 frames per second) to display a smooth illustration. At each visualisation time step, the 3D-vessels (A) and the mapped scalars (P, Q, v) are adapted to the simulation solution of a time point. Where the time points of the simulation solution are iterated with $\varphi = 1$. If the total time of the simulation is reached, the visualisation starts from the beginning.

The representation can not be recreated 30 times per second as this takes too long. An update method is implemented instead: it reassigns the 3D-vessel radius according to A^t and the colours according to the mapped scalars (P^t, Q^t, v^t). The algorithms implemented are optimized for low computational time and low memory usage (see also section 3.8.2).

Nevertheless, on old computers with low computational power, the 3D visualisation of large networks can stutter. To enhance the visualisation in this case, the wall movements, i.e. the change of 3D-vessel radius can be turned off.

The solution of a simulation can consist of many time points, as vascular1DFlow is explicit in time. For this reason, the time point iterator φ can be increased, i.e. the solution of some time points are skipped.

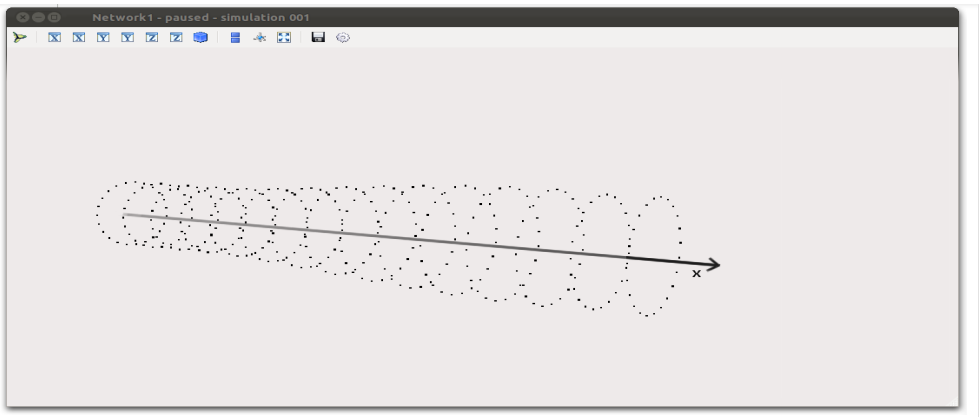

(a) Circular points based on the vessel area A

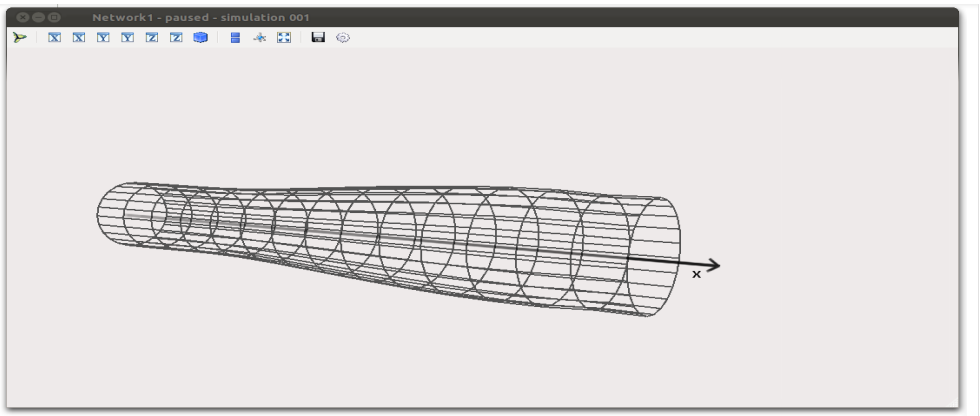

(b) Wire frame of the created circular points

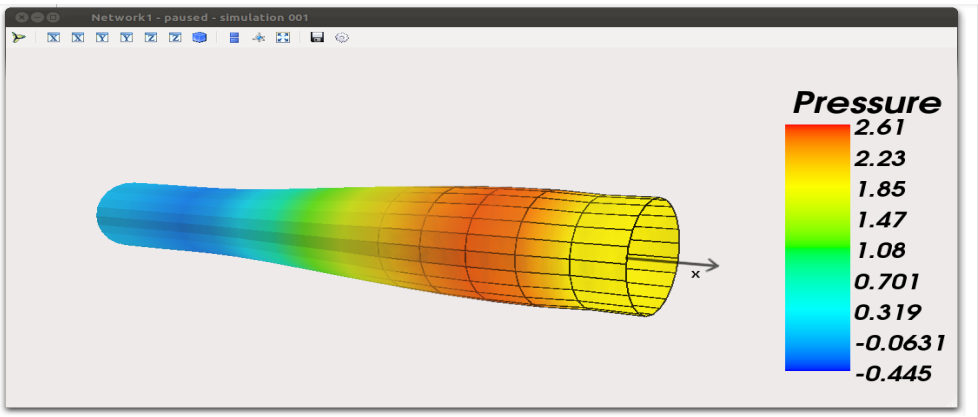

(c) Colour map with coloured surfaces and corresponding LUT of pressure values

Figure 13: Creation of a 3D vessel representation with colour mapped scalar information

3.7.3. Additional Features of the 3D Visualisation

In addition to the visualisation of a vascular network and solution data as 3D vessels and mapped colors, some advanced features are implemented. All features explained below can be activated by a keyboard short cut or mouse click. The camera showing the 3D representation is free rotatable and movable in space.

2D Plots from within the 3D Visualisation
By clicking on a vessel with the mouse cursor, a 2D time-quantity plot of the vessel is opened in a second window. The plot shows the three quantities P,Q and A over the total simulation time in the middle of the vessel. With the key stroke 'g', the save-mode is activated, and the 2D time-quantity plots are saved to HDD as .png-files.

The space-quantity plots can be activated with the key-stroke 'G'. The mouse click on a vessel opens now two additional windows; one for the time-quantity and one for the space-quantity plot. Here the space quantity plot is animated, showing the three signals $P(t)$,$Q(t)$ and $A(t)$ for the hole vessel. Figure 14 shows the 3D visualisation of a large vascular network representing the arterial tree with the two 2D plots of the ascending aorta.

Amplification of the Radius of a Vessel
The wall movements are determined by the vessel compliance and the actual pressure in the vessel. To increase the effect of dilatation and contraction of the vessels, the change of vessel radius can be amplified. The calculation of the visualized radius $\hat{r}(t,x)$ is given by:

$$\hat{r}(t,x) = r(t=0,x) + \Delta r(\Delta t, x)\,\zeta \tag{3.4}$$

$$\text{where} \quad \Delta r(\Delta t, x) = r(t,x) - r(t=0,x), \tag{3.5}$$

where ζ is the amplification factor and $r(t,x)$ is the vessel radius at point x at time t. The factor ζ can be increased and decreased with keystrokes during visualisation runtime.

Visualisation of Different Solution Data Sets
The 3D visualisation provides the possibility to load several solution data sets from different simulations of a network. These can be altered during the visualisation process. The effect on the total network of *e.g. different boundary conditions* can be studied without opening and closing programs or files. With this, the data sets created by each gPC evaluation in VPC can be checked.

Pictures and Films of the 3D Visualisation
Pictures of each visualisation time step are stored on HDD after the keystroke 'm'. Theses pictures can be combined to a film e.g. with FFmpeg[15]. The pictures saved to HDD show exactly the same as the 3D visualisation window.

[15] http://ffmpeg.org/index.html

Velocity Profiles

In vascular1DFlow the velocity profiles are approximated with the power law profiles (section 2.1.1). The 3D Visualisation presents the approximated velocity profile in form of 3D arrowheads. The vessels are cut open by half and at every second grid node in the vessel, the velocity profile is visualized in the zx plane, with 11 arrows. The arrows point in mean velocity direction and the colors and sizes are set according to the velocity at the profile points, calculated with the power law (equation (2.3) and (2.4)). The visualisation of the velocity profile is proceeded with and without wall movement, as illustrated in figure 15(a) and figure 15(b).

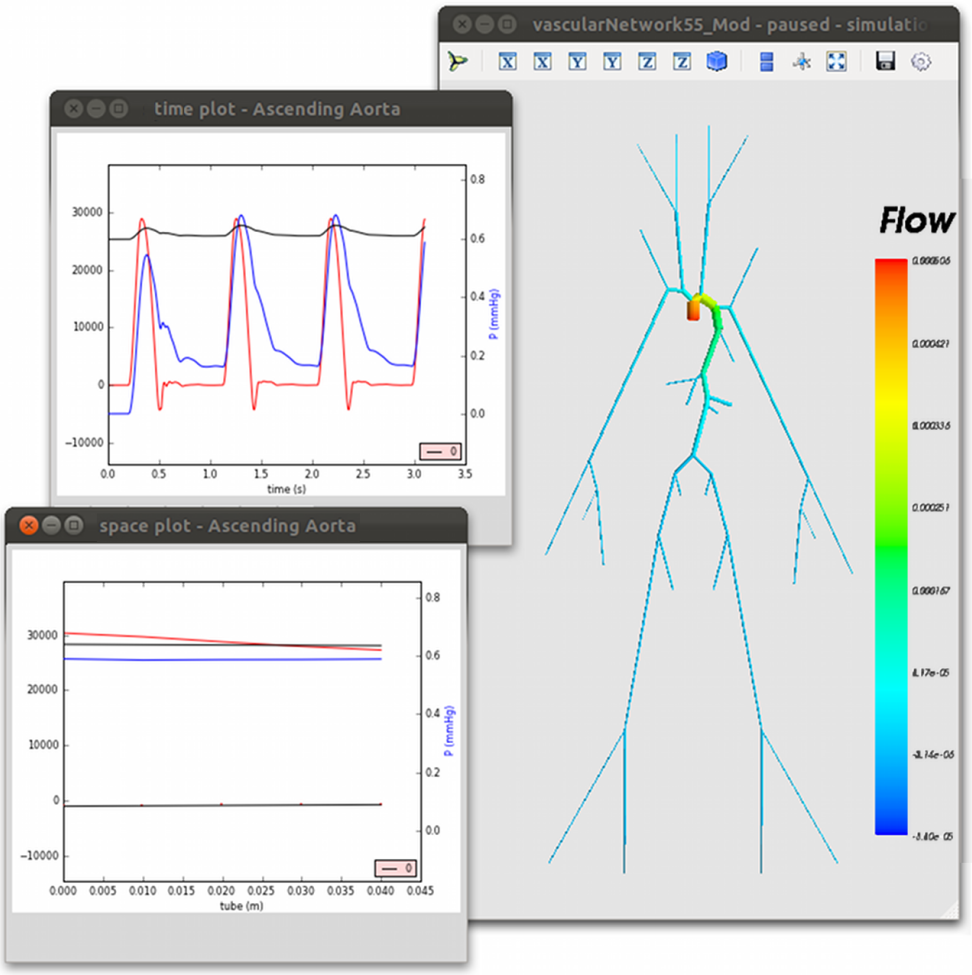

Figure 14: 3D visualisation of a vascular network with the 2D plots, space-quantity and time-quantity, for the ascending aorta

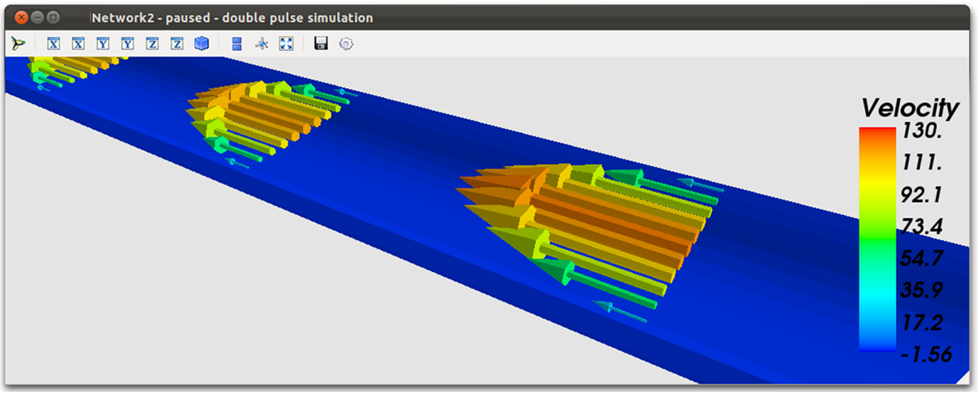

(a) Velocity profile without movements of the vessel wall

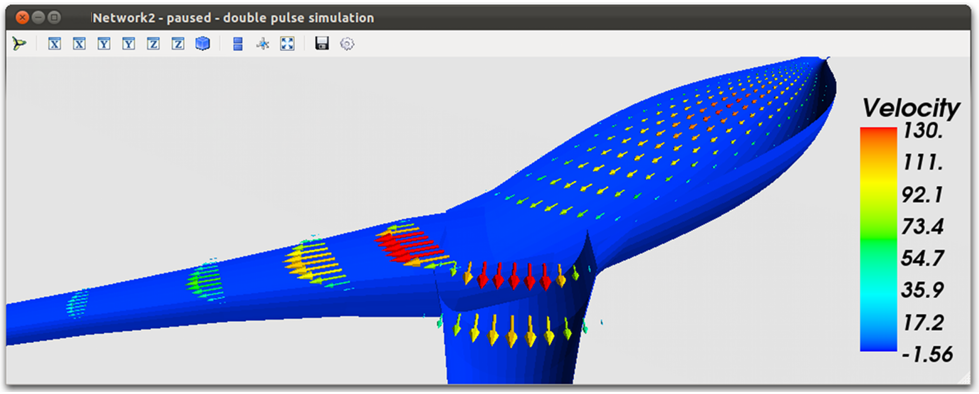

(b) Velocity profile with enabled wall movements, where the change in radius is increased by a factor ζ

Figure 15: 3D Visualisation showing the velocity profiles of a cut open vessel(s).

3.8. Additional Algorithms and Methods

3.8.1. Meshing Optimisation

Meshing in vascular1DFlow means determining the number of grid nodes N_i and thus Δx_i for each branch i in a network ($\Delta x_i = L_i/N_i$). N_i, respectively Δx_i, has mainly three effects on the simulation

1. Determination of the resolution of the spatial solution in the branch i. To gain a minimum spatial resolution in each branch a minimum number of grid nodes N_{min} is defined for each branch i.

2. Control of Δt of the simulation (for fixed material parameters and CFL (section 2.1.6). For fixed material parameters and CFL Δt_i and N_i are indirect proportional, i.e. decreasing N_i increases Δt and vice versa. Thus, with regard to computational time, N_i is desired to be as small as possible.

3. Influence on the accuracy of the simulation by controlling Δt and therefore the CFL number (section 2.1.6).

In vascular1DFlow the time step Δt is determined in deference to the CFL condition (2.54). For each branch i in the network, the speed λ_{1i} and c_i respectively is calculated for the given material parameters and compliance model (section 2.1.1) using the Bramwell-Hill equation (equation 2.14). The grid node inter space Δx_i in each branch is calculated with the given length L_i and the number of grid nodes N_i. The local time steps Δt_i satisfying the CLF condition are calculated with

$$\Delta t_i = \frac{\Delta x CFL_{max}}{c_i} \tag{3.6}$$

where $CFL_{max} < 1$ is the user defined maximal CFL. The smallest Δt_i determines the simulation time step Δt as the CFL condition is fulfilled for all branches in the network.

$CFL_{j\ res}$ is introduced as the resulting CFL using c_j, Δx_j and Δt for all branches j. Here j excludes the branch where Δt_i = Δt. As discussed before is $CFL_{j\ res} \leq CFL_{max}$. However, it was found that sometimes $CFL_{j\ res}$ can be very small (close to 0.1), which leads to inaccurate representation of the physics (section 2.1.6). This is primarily a result of a poorly meshed network. For an accurate simulation it is necessary to keep the $CFL_{j\ res}$ close or equal to CFL_{max}. This can be accomplished by increasing the number of grid nodes N_j of the poorly meshed branches.

To find the optimal number of grid nodes N_i for each branch i in a given network the following algorithm has been elaborated:

1. Define all grid nodes with the minimum amount of designated nodes (N_{min}) and CFL_{max}

2. Determine all Δt_i and assign Δt = min (Δt_i)

3. Calculate $CFL_{j\ res}$ with Δt for all remaining branches j
4. Minimize $r\ =\ \mid CFL_{max} - CFL_{j\ res} \mid$ under the condition $r\ \geq\ 0$ by increasing N_j iteratively
5. Apply the new number of grid nodes to the network.

3.8.2. Speed up of Numerical Algorithms

Computational costs, i.e computational time and memory usage, is one significant factor regarding numerical simulations, even though the computational power of computer increases. Many algorithms written in basic python can be boosted in speed and memory usage by using additional modules. A common approach is to apply the numpy-package, which is partially written in C and Fortran, and thus by far faster than Python [15].

All algorithms created within the current work are optimized and tested in terms of computational speed and memory usage. This is especially significant for the update of the 3D visualisation (section 3.7) for each visualisation step. In the following, the optimisation of one process is highlighted. Three different algorithms for the summation process of the wave splitting are considered (section 3.5.2).

Recapitulating the four summations to be calculated:

$$P_{f\,i}\ =\ \sum_{j=0}^{i} \Delta P_{f\,j} \quad P_{b\,i}\ =\ \sum_{j=0}^{i} \Delta P_{b\,j} \qquad \text{recap eq. } (3.2)$$

$$Q_{f\,i}\ =\ \sum_{j=0}^{i} \Delta Q_{f\,j} \quad Q_{b\,i}\ =\ \sum_{j=0}^{i} \Delta Q_{b\,j} \qquad \text{recap eq. } (3.3)$$

The first algorithm to calculate the summations is written with basic python commands (an introduction to Python can be found in [16]). The approach is a *for-loop*, which is a more or less direct translation of the summations. While the Δ signals are iterated, the sum is stored in the new vector signal. Illustrated for the signal S and ΔS where both are vectors with positions $i \in [0, L]$ (written as S[i]):

FOR ΔS[I] IN ΔS:
  S[I] = S[I-1] + ΔS[I]

The second more advanced approach is based on *matrix* arithmetic and uses the python numpy-package. Calculating the scalar product of the ΔS values with a lower diagonal matrix of ones M, leads to the result:

$$M \circ \Delta S = S \tag{3.7}$$

$$\begin{bmatrix} 1 & 0 & 0 & 0 & 0 \\ 1 & 1 & 0 & 0 & 0 \\ 1 & 1 & 1 & 0 & 0 \\ 1 & 1 & 1 & 1 & 0 \\ 1 & 1 & 1 & 1 & 1 \end{bmatrix} \circ \begin{bmatrix} \Delta 1 \\ \Delta 2 \\ \Delta 3 \\ \Delta 4 \\ \Delta 5 \end{bmatrix} = \begin{bmatrix} \Delta 1 \\ \Delta 1 + \Delta 2 \\ \Delta 1 + \Delta 2 + \Delta 3 \\ \Delta 1 + \Delta 2 + \Delta 3 + \Delta 4 \\ \Delta 1 + \Delta 2 + \Delta 3 + \Delta 4 + \Delta 5 \end{bmatrix} \tag{3.8}$$

The matrix M, once created and stored in the computer memory, can be used for all four signals. However, as the signal lengths increase, the matrix size (equation 3.9) increases and with it the required memory.

$$\text{number of elements} = \frac{(L^2 + L)}{2}, \quad L = \text{length of signal S} \tag{3.9}$$

The third approach is a combination of the two previous ones, the *for-loop matrix* algorithm. ΔS is divided into equal parts in a way, that the resulting length of the sub-signals $\Delta \hat{S}$ is around 100. Then, the same matrix summation process as above is applied for each sub-signal, but with the significantly smaller matrix $\hat{M}$. This procedure is implemented with a for-loop. However, for each iteration, the last value of the processed signal, has to be added to the first value in the next sub-signal, to ensure the consistence of the summation (see also example below). The division into sub-signals is possible unless the signal length L is a prime number, in this case a special treatment is applied. After removing the last value of ΔS, it is dividable into equal parts. In the end of the process, the signal is completed by adding the sum of the last number and the removed number.
Applying the process to the example given above:

1. Identify, the length of the sub-signals $\hat{L}$, the size of the matrix $\hat{M}$, the number of iterations for the for-loop and the additional number if $\hat{L}$ is a prime number. For the better understanding, is the example from before coloured, illustrating the sub-matrix $\hat{M}$ in blue, the sub-signals in red, and the identified prime number in green. *[NB: The algorithm does not construct the matrix $\hat{M}$ like this.]* In this case, L is 2, the number of iterations is 2, and the matrix size N($\hat{M}$)=3, compared to N(M) = 15 (example above).

$$M \circ \Delta S = S \tag{3.10}$$

$$\begin{bmatrix} \begin{bmatrix} 1 & 0 \\ 1 & 1 \end{bmatrix} & \begin{matrix} 0 & 0 \\ 0 & 0 \end{matrix} & \begin{matrix} 0 \\ 0 \end{matrix} \\ \begin{matrix} 1 & 1 \end{matrix} & \begin{bmatrix} 1 & 0 \\ 0 & 1 \end{bmatrix} & \begin{matrix} 0 \\ 0 \end{matrix} \\ \begin{matrix} 1 & 1 \end{matrix} & \begin{matrix} 1 & 1 \end{matrix} & 1 \end{bmatrix} \circ \begin{bmatrix} \begin{bmatrix} \Delta 1 \\ \Delta 2 \end{bmatrix} \\ \begin{bmatrix} \Delta 3 \\ \Delta 4 \end{bmatrix} \\ \begin{bmatrix} \Delta 5 \end{bmatrix} \end{bmatrix} \tag{3.11}$$

2. Remove the last number from the signal and store it:

$$\Delta S_{rem} = \Delta S_5$$

3. Iterate with a for loop over the sub-signals, calculating the dot product with matrix $\hat{M}$.
Iteration 1:

$$\begin{bmatrix} 1 & 0 \\ 1 & 1 \end{bmatrix} \circ \begin{bmatrix} \Delta 1 \\ \Delta 2 \end{bmatrix} = \begin{bmatrix} S_1 \\ S_2 \end{bmatrix} = \begin{bmatrix} \Delta 1 \\ \Delta 1 + \Delta 2 \end{bmatrix}$$

Add the last solution in the vector calculated to the first ΔS value in the vector of the next iteration step.
Iteration 2:

$$\begin{bmatrix} 1 & 0 \\ 1 & 1 \end{bmatrix} \circ \begin{bmatrix} \Delta 3 + S_2 \\ \Delta 4 \end{bmatrix} = \begin{bmatrix} S_3 \\ S_4 \end{bmatrix} = \begin{bmatrix} \Delta 1 + \Delta 2 + \Delta 3 \\ \Delta 1 + \Delta 2 + \Delta 3 + \Delta 4 \end{bmatrix}$$

4. Complete the calculations by adding the removed prime value:

$$S_5 = \Delta S_{rem} + S_4$$

5. Obtain the same solution S as before

$$\begin{bmatrix} S_1 \\ S_2 \\ S_3 \\ S_4 \\ S_5 \end{bmatrix} = \begin{bmatrix} \Delta 1 \\ \Delta 1 + \Delta 2 \\ \Delta 1 + \Delta 2 + \Delta 3 \\ \Delta 1 + \Delta 2 + \Delta 3 + \Delta 4 \\ \Delta 1 + \Delta 2 + \Delta 3 + \Delta 4 + \Delta 5 \end{bmatrix}$$

All three algorithms for the summation in equations (3.2) and (3.3) are implemented and tested using the timeit module[16] of python, constructed for process time-tests. Each algorithm is run 100 times and the mean process time is calculated. This procedure is repeated 100 times, and again the mean time of the mean times is evaluated, which gives in total 10.000 evaluations. The resulting calculation times for different signal lengths are illustrated in figure 16.

For small L, the *for-loop* is the slowest algorithm. If the signal length reaches a certain limit, the *matrix* algorithm gets slower than the *for-loop*. This is mainly due to the large amount of memory, required. The process time of the *for-loop matrix* algorithm, using the benefit of both processes, increases very slowly.
[NB: The matrix M and signals S are split so that the lengths of the sub signals is around 100.]

[16] http://docs.python.org/library/timeit.html

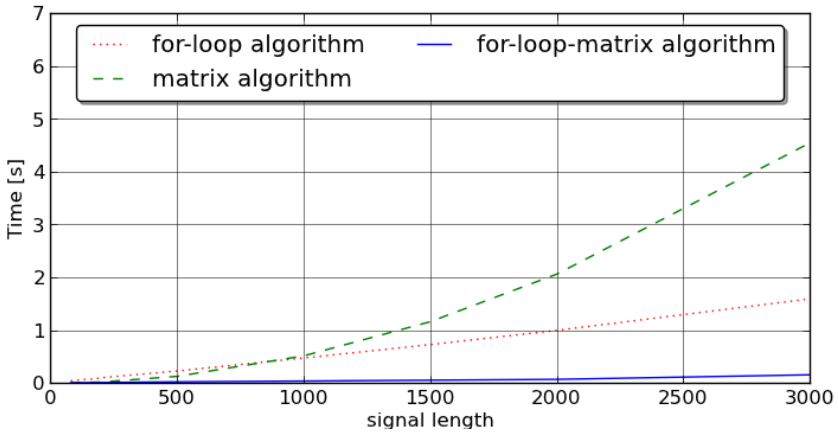

Figure 16: Comparison of different algorithms in process speed.

4. Assessment of the Vascular Polynomial Chaos

The elaborated vascular polynomial chaos method for the simulation of uncertain vascular systems is tested in two cases. The first case (section 4.1) is used for the verification of the elaborated simulation approach. In the second case (section 4.2) a large vascular network of 49 arteries representing the systemic arterial tree is studied with the elaborated simulation approach.

4.1. Case I - Verification of Vascular Polynomial Chaos

The case I, used for verification of the simulation approach, is a simple network consisting of three arteries, forming a bifurcation. The model parameters and boundary conditions are set identical to the first test case in the work of D. Xiu and S.P. Sherwin [38]. In addition to analytic solutions, the result of their work is used for verification.
The following sections will describe the network and simulation set up (4.1.1), the verification of the mathematical model (4.1.2), the verification of the simulation approach (4.1.3) and the discussion of the result (4.1.4).

4.1.1. Simulation Setup

The bifurcation (figure 17) considered for the verification test case consists of three vessels; one mother branch and two daughter branches. All vessels have the same length. The mother and the daughter branches differ in their material parameters, whereas the two daughter branches are defined identical. All simulation parameters are listed in table 4. The offline description, i.e. the XML-file, can be found in the appendix A.2.

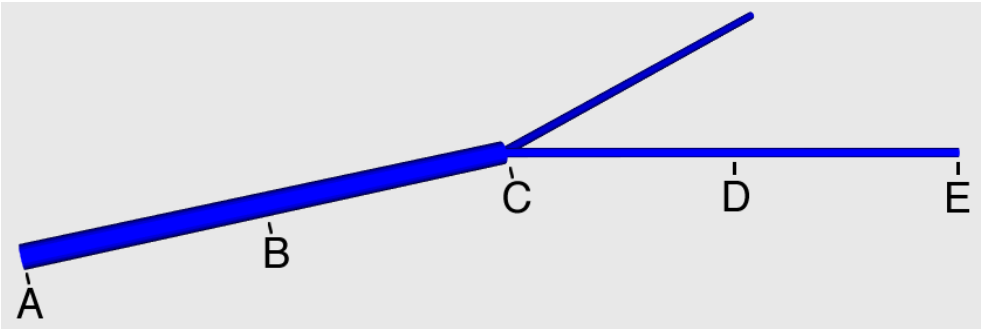

Figure 17: Initial condition of the simple bifurcation network with indicated measuring points

Parameter	Mother branch		Daughter branches	
Radius r	0.005	[m]	0.002	[m]
Length L	0.2	[m]	0.2	[m]
$\hat{\beta}_i^{Lap}$	324970.0	[Pa/m]	796020.0	[Pa/m]
β_i^{Lap} interval	[292473.0 357467.0]	[Pa/m]	[716418.0 875622.0]	[Pa/m]
global Parameter				
waves speed c	1.2	[m/s]		
blood density ρ	1000	[kg/m^3]		
blood viscosity μ	0	[Pa s]		
CFL	0.95	[-]		
total time T	0.5	[s]		

Table 4: Material and simulation parameters of the test case

The description of the vessel compliance C applied by D. Xiu and S.P. Sherwin [38] in their work, is based on the third constitutive equation 2.9 described in section 2.1.1.

$$C = \frac{2}{\beta^{Lap}}\sqrt{A_0} + \frac{2}{(\beta^{Lap})^2}(P - P_0) \quad \text{recap eq. } (2.10)$$

where the stiffness parameter β^{Lap} is a function of the Young modulus E and the wall thickness h of the vessel (equation 2.11). The wave speed c of the system (eq. 2.14) is per definition related to the compliance C. Thus a relation between β^{Lap} and the wave speed c can be stated (eq. 4.2). Inserting the linearised expression of the compliance 2.10 into the definition of the wave speed leads to expression 4.1.

$$c = \sqrt{\frac{A}{\rho C}} \quad \text{recap eq. } (2.14)$$

$$c = \sqrt{\frac{\beta^{Lap}}{2\rho}}\sqrt[4]{\frac{A}{A_0}} \tag{4.1}$$

Assuming constant density ρ and constant cross-sectional areas of the vessel $A = A_0$, leads to:

$$c \sim \sqrt{\beta^{Lap}} \tag{4.2}$$

For this problem the β^{Lap} parameters of each vessel are set to obtain the same wave speed c of 1.2 m/s in each branch of the network. These values will be denoted with $\hat{\beta}_i^{Lap}$, where $i = 1$ stands for the mother and $i = 2, 3$ for the daughter branches (values see table 4). The blood density ρ is set to $1000\ kg/m^3$ and for the total network, viscous forces are neglected, i.e. μ = 0.

For the parametric uncertainty analysis, the β_i^{Lap} parameters are assumed to be uniformly distributed in a interval of $\pm 10\% \hat{\beta}_i^{Lap}$ or $0.9\hat{\beta}_i^{Lap} \leq \beta_i^{Lap} \leq 1.1\hat{\beta}_i^{Lap}$. Hence $\hat{\beta}_i^{Lap}$ corresponds to the expected value E[β_i^{Lap}] of each distribution.

NOTE TO THE NOTATION: All variables referring to the expected values of the distributions i.e $\hat{\beta}_i^{Lap}$ are denoted with a hat $\hat{\chi}$. The variables without $\hat{\chi}$ belong to the uncertain parameters β_i^{Lap}.

As illustrated in figure 17 measuring points A-E are defined in the network. At these points, the sensitivity analysis will be carried out. As the daughter branches are defined identically, the points D and E represent both daughter branches.
At point A, the inflow point of the network, the inflow velocity (figure 18) is prescribed with

$$U^{in} = U_{peak} exp(-C(t - t_0)^2) \tag{4.3}$$

where U_{peak} = 0.005 m/s, C = 5000 s^{-2} and t_0 = 0.05 s [38].

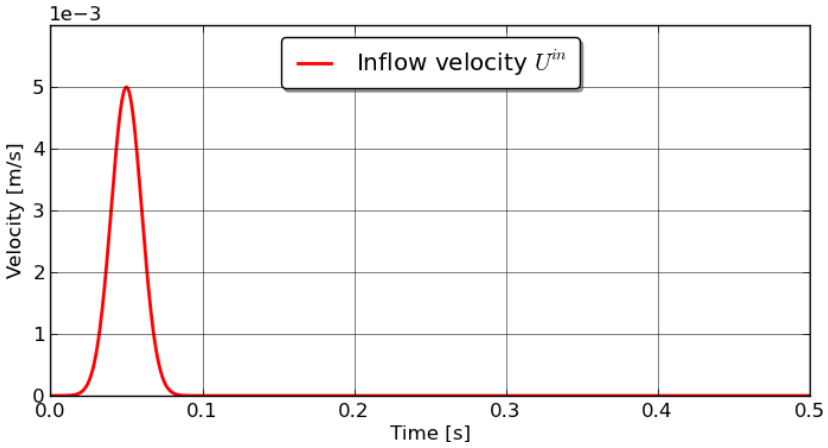

Figure 18: Inflow velocity as defined in equation 4.3

The velocity function 4.3 results in a short flow pulse, with a pulse time period of $t_{pl} \approx$ 0.05 s. The wavelength of the pulse is approximately $\lambda_w = c \cdot t_{pl} = 0.072m$ i.e $\lambda_w << L$ of the mother and daughter branches. The wave speed c of the pulse (1.2 m/s) is quite slow and can probably be found in big arteries. The pulse time period and the pulse wavelength are much shorter than the corresponding values of a normal heart beat. However, the so defined inflow allows a better prediction of the simulation result and thus leads to a more easy understanding of the dynamics of the system.
At the end of the daughter branches and the inlet, absorbing boundary conditions, i.e. zero reflection, are assumed. The pressure wave is reflected at the bifurcation with the reflection coefficient R_f^P [26].

Using the linearised reflection coefficient for pressure waves equation 4.4, R_f^P becomes

0.5 for the given wave speed and initial areas A_i,i=1,2,3.

$$R_f^P = \frac{\frac{A_1}{c_1} - \frac{A_2}{c_2} - \frac{A_3}{c_3}}{\frac{A_1}{c_1} + \frac{A_2}{c_2} + \frac{A_3}{c_3}} \tag{4.4}$$

The total simulation time is set to 0.5 s, which guarantees the return of the reflected pulse to the inlet. The CFL number (equation 2.52) is fixed to 0.95. Figure 19 shows the simulation at different points in time, visualised with the implemented 3D visualisation (section 3.7) described in.

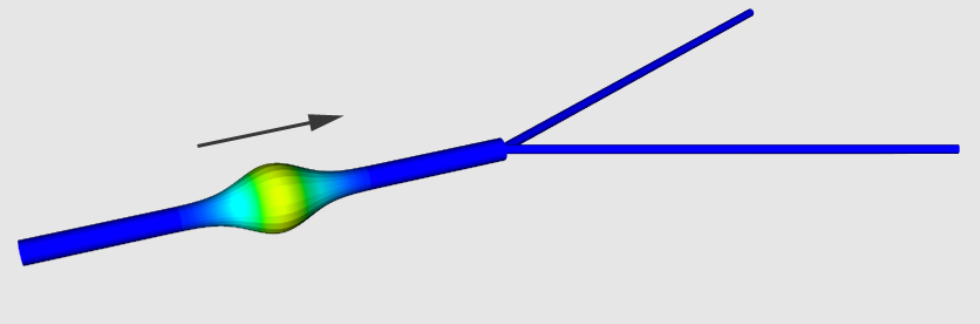

(a) Forward propagating pressure pulse in the mother branch

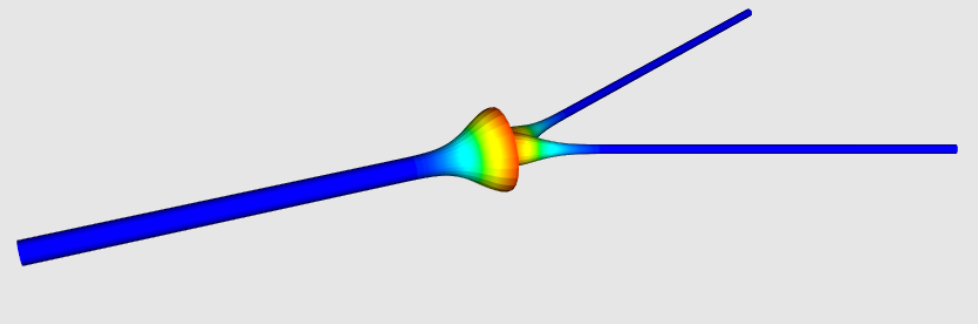

(b) Reflection of the pulse at the bifurcation

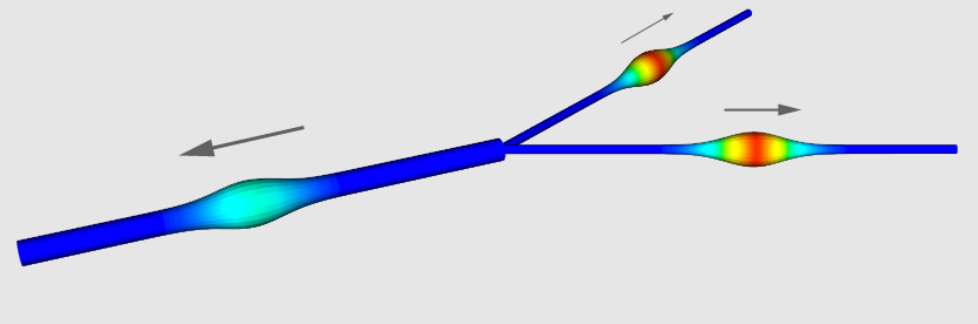

(c) Backward travelling pressure pulse in the mother branch and forward directed pulses in the daughter branches

Figure 19: Time series of the propagation pressure pulse at time t = 0.14 s 19(a), t = 0.21 s 19(b) and t = 0.3 s 19(c), with indicated pulse propagation directions

4.1.2. Verification of the Mathematical Model

Before running the vascular polynomial chaos simulation with the uncertain β^{Lap} parameters, the deterministic simulation is verified. This is carried out by comparing the simulation results using the $\hat{\beta}_i^{Lap}$ values with the analytical solution and with the results obtained by D. Xiu and S.P. Sherwin [38].

At the measuring points A-E the flow signal $Q(t)$ of the simulation is checked against the analytical solution.

Analytic Solution

The analytic flow is calculated from the defined inflow velocity (equation 4.3) multiplied with the initial area A_0. The flow pulse occurrence times and amplitudes vary in the simulation for each measuring point A-E. To determine the analytic solution at point A-E, the phase shift and amplitude of the analytic flow pulse is evaluated.

The occurrence time of the pulse peak can be determined for each measurement point as the flow pulse travels with the constant wave speed c = 1.2 m/s through the network. *E.g occurrence time at point E:* $t^E_{occ.}$ *= (0.2 m + 0.1 m) / 1.2 m/s = 0.3 s*.

As the viscous forces are neglected (section 4.1.1), the flow pulse amplitude changes only due to the reflection at the bifurcation. The initial amplitude of the entering flow pulse in the mother tube is $Amp^A_f = Amp^B_f = 4E-07m^3/s$ determined by the inflow and initial area A_0. For pressure pulses the linear reflection coefficient at the bifurcation is R^P_f = 0.5 (equation 4.4). The flow Q and pressure P are coupled through the characteristic impedance equations $P = -Z_0\ Q$ (equation 2.42 in section 2.1.4). Thus the reflection coefficient at the bifurcation for the flow pulse is $R^Q_f = -0.5.$, as the impedance can be seen as constant. The amplitude of the reflected flow pulse in the mother branch becomes $Amp^M_b = Amp^M_f * R^Q_f = -2E-07m^3/s$. At the bifurcation, point C, the incoming and reflected wave superpose. The amplitudes add which results in an amplitude half of the incoming wave $Amp^C = 2E-07m^3/s$. The amplitude of the pulse propagating through the daughter branches is determined by the pulse at point C, i.e the amplitude at point D and E is the same as at point C.

Accuracy of the Simulation

The mismatch of the simulation flow signal $Q(t)$ with 50 grid nodes and the analytic solution points out poor accuracy (figure 20).

The accuracy of the simulation is depending on the numerical discretisation of the system, *i.e. on the time step* Δt *of the simulation and on the grid inter space* Δx *in the branches*. In vascular1DFlow an explicit forward-backward MacCormack scheme is applied (see section 2.1.2). In general, the accuracy increases with smaller Δt and with smaller Δx [12]. Δt is determined with the approximated CFL number (section 3.8.1):

$$CFL = \frac{\Delta t}{\Delta x}\, c \quad \text{recap eq. } (2.52)$$

Δx is user defined by the number of grid points N and the length of a vessel L; $\Delta x = L/N$.

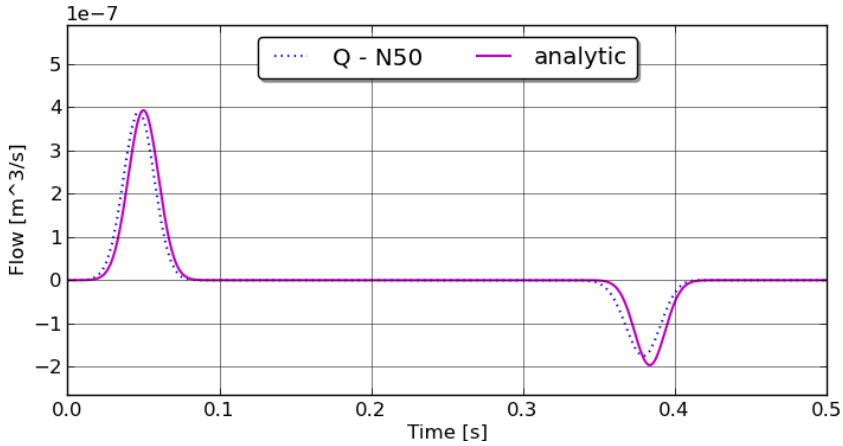

(a) Total signal Q(t) at Point A compared to the analytical solution with number of grid points N = 50

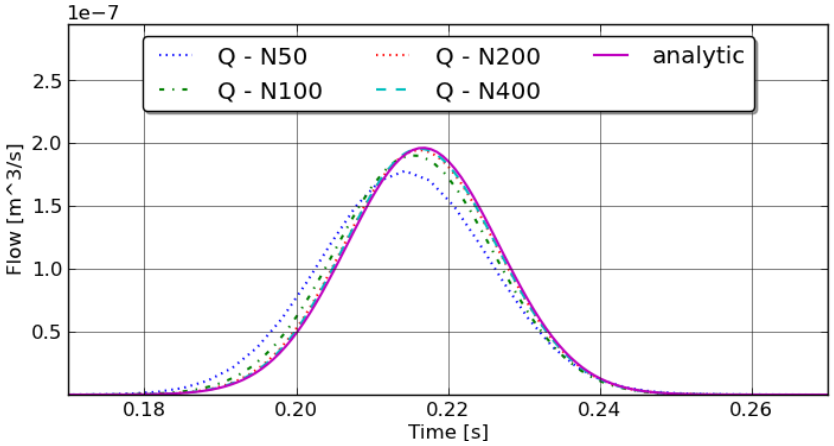

(b) Detail of the flow pulse at point C for solution with N = 50,100,200,400 compared with the analytical solution

Figure 20: Comparison of the simulation flow signal Q(t) with the analytical solution

The CFL number is held constantly close to one and the wave speed c is constant in the network. Consequently the accuracy of the simulation can be increased by grid refinement only, i.e extending the number of grid nodes per branch. This leads to a decreased Δx and Δt. Figure 20 shows the comparison of simulation with different N = 50,100,200 and 400 and the analytical solution. However, with increasing number of grid points and smaller time steps, the computational costs, i.e the time it takes to calculate the solution, increases as well.

To identify an appropriate match in accuracy and computational costs, the accuracy of the simulation with different number of grid points is estimated and compared to the process time. There are mainly three different kinds of errors leading to a decrease in accuracy: dispersion, diffusion and numerical round-off errors. Dispersion results in a time shift of the

total pulse and diffusion in a damped amplitude and widening of the pulse. To estimate the accuracy in those cases, the dissipation and diffusion of the pulse peaks are considered. The trend of the widening-error is assumed to stay proportional to the changes in amplitude, so the consideration of the damping of the amplitude only states a sufficient estimate for the accuracy. The numerical round-off errors are neglected.

For each pulse peak at all measuring points j = A-E a relative dispersion and diffusion error is defined:

$$Err_j^{Diff} = \frac{|Amp_j^{analytic} - Amp_j^{simulation}|}{Amp_j^{analytic}} \qquad Err_j^{Disp} = \frac{|t_{occ.\ j}^{analytic} - t_{occ.\ j}^{simulation}|}{t_{occ.\ j}^{analytic}} \tag{4.5}$$

where Amp_j is the amplitude and $t_{occ.\ j}$ the occurrence time of the pulse peak j. As the errors may increase or decrease over the total simulation time, the relative dispersion and diffusion errors of all peaks are concentrated and a relative expected error is calculated:

$$Err_{total} = \frac{1}{n_{peak}} \sum_{j=A}^{E} \frac{Err_j^{Diff} + Err_j^{Disp}}{2}; \tag{4.6}$$

where the number of peaks n_{peak} is seven (two at A,B and one at C,D,E). The total relative error compared to the simulation time is illustrated in figure 21. The best match between accuracy and computational costs is found for N = 200. At this point the change in accuracy i.e. the slope of the total relative error curve is almost horizontal. Additionally, the slope of the computational time curve increases after the point N = 200 slightly, this may be due to an increased need for computer memory. The curves in figure 21 are estimated with a relatively small set of samples, thus they are composed by straight lines. However, as the trend of the curves is essential, these curves are nevertheless appropriate.

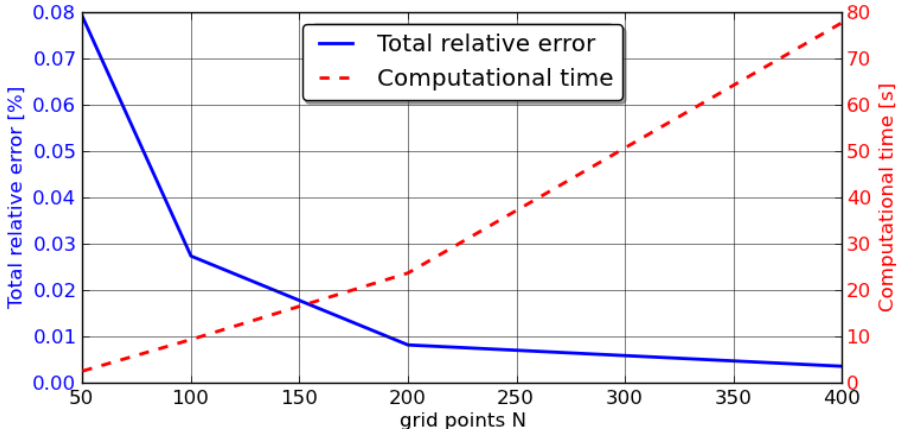

Figure 21: Comparison between simulation time and the total relative error of the simulation at point C

The pressure signal P(t) of simulations with different N is compared to the results of D. Xiu and S.P. Sherwin [38]. The simulations with N $>$ 100 show a appropriate match with the extracted data. Figure 22 shows this comparison with the extracted peak data at measuring point B.

The signals and signal points of the work of D. Xiu and S.P. Sherwin [38] are extracted with the program DataThief[17]. The deterministic simulation of the bifurcation with vascular1DFlow delivers accurate results, compared to the results of D. Xiu and S.P. Sherwin [38] and the analytical solution.

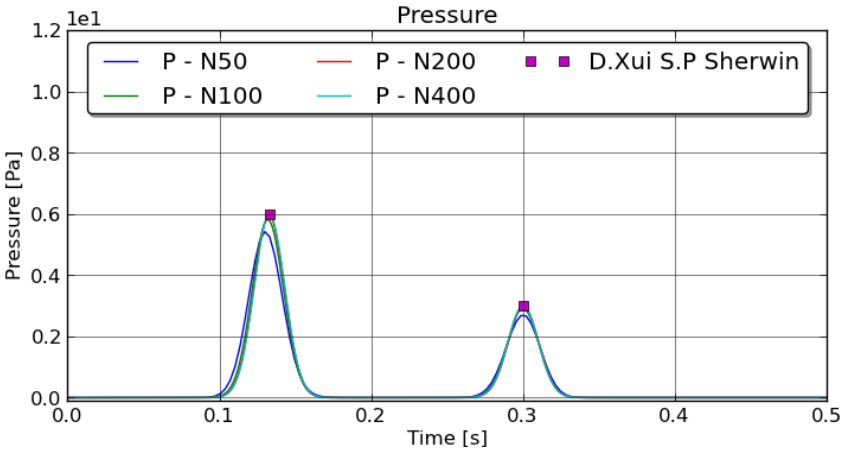

Figure 22: Comparison of the pressure signal P(t) of the simulation with different number of grid points with extracted peak data of D. Xiu and S.P. Sherwin [38] at point B

[17] DataThief: http://www.datathief.org/

4.1.3. Verification of Vascular Polynomial Chaos

The vascular polynomial chaos simulation with the uncertain β^{Lap} parameters as defined previously, is investigated at the same measuring points A-E. As the collected data and corresponding plots are in numbers, the following illustrations will be focused mainly on measuring point B. However, additional figures can be found in the appendix A.1 The simulations are run with several polynomial orders. With the order of the polynomials the computational costs increase. This arises from the increased number of evaluations required for the construction of the gPCE. The number of evaluations is determined by stochastic grid collocation method see section 2.2.2. The number of required simulations for different polynomial orders M are listed in table 5. It was found, that already $M = 3$ leads to an appropriate result for the sensitivity analysis. Figures 24 and 25 show the expected values and the STD at measuring point B for order three and order seven, respectively. The expected values and the STDs of the signals show identical curves. This means, that the sensitivity of the uncertain β_i^{Lap} parameters is already captured by a third order gPCE. Thus it is not necessary to run the costly seven order simulation.

Figure 23 illustrates the expected values and STD signals obtained by D. Xiu and S.P. Sherwin [38] at measuring point B. These results are in good agreement with the expected values and STD calculated with VPC (figure 24 and 25).

order of the polynomials M	2	3	4	5	6	7
req. number of gPC evaluations	19	56	121	252	452	791

Table 5: Order of polynomials with their required number of evaluations

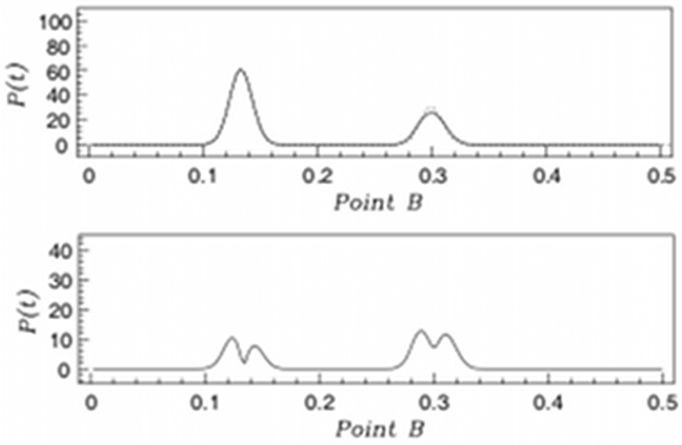

Figure 23: Expected values (top) and STD (bottom) of the pressure signal at measuring point B, obtained by D. Xiu and S.P. Sherwin [38]

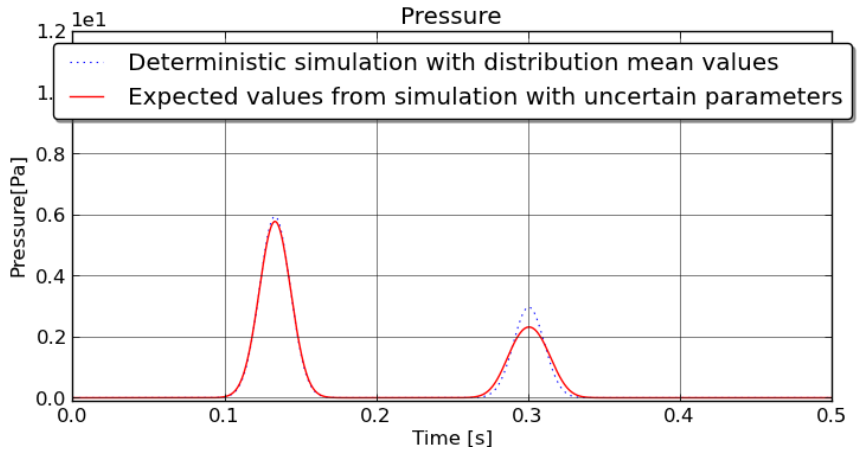

(a)

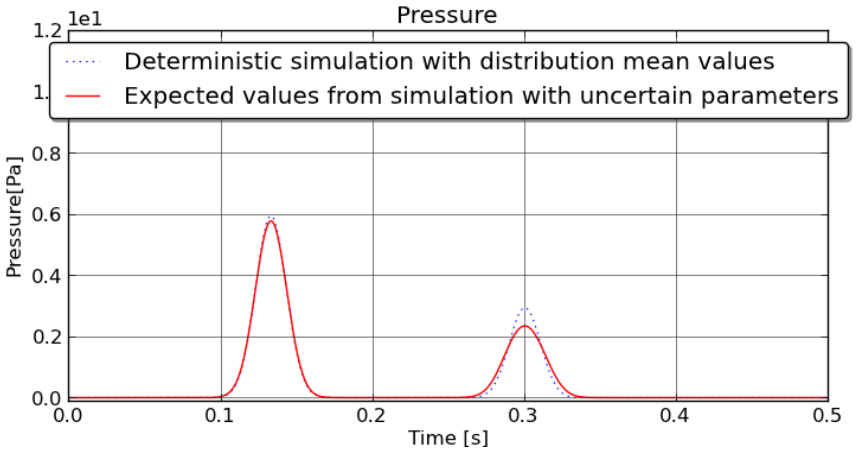

(b)

Figure 24: Expected values of the pressure signal at point B with polynomial order three (24(a)) and polynomial order seven (24(b))

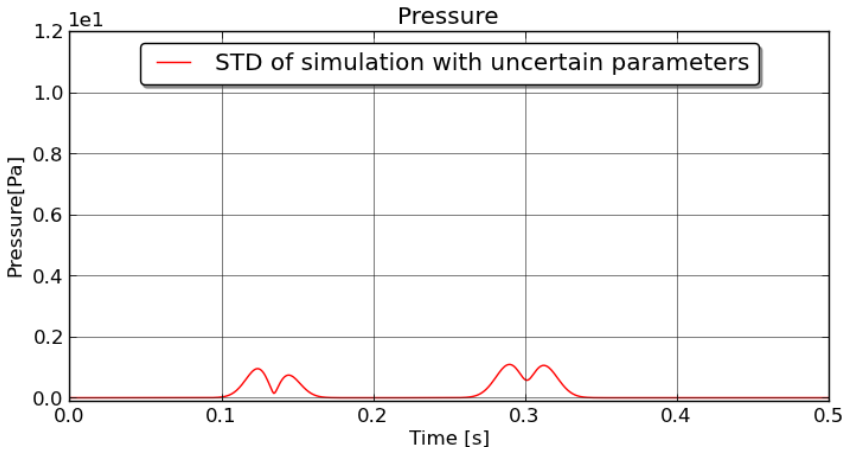

(a)

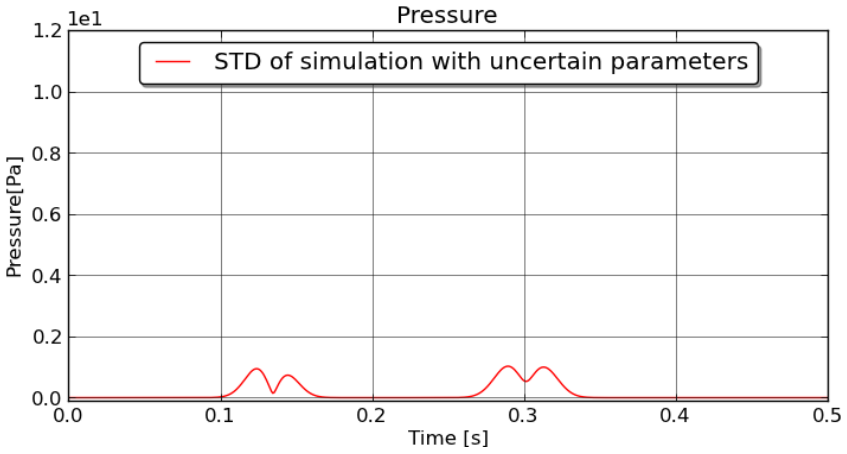

(b)

Figure 25: STD of the pressure signal at point B with polynomial order three (25(a)) and polynomial order seven (25(b))

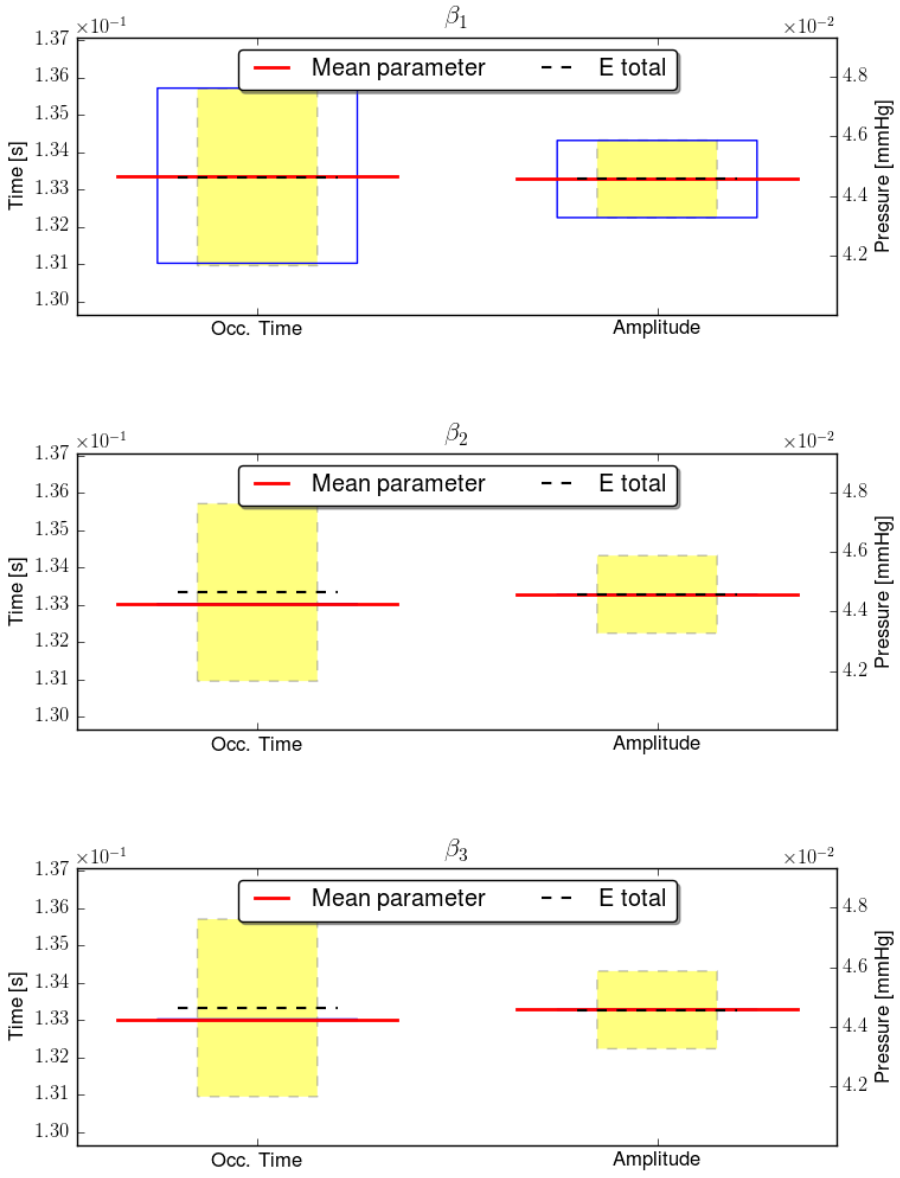

Figure 26: Sensitivity on the first peak (forward directed pulse) at measuring point B, where the blue box is STD_i, the red line $\mathbb{E}_i$, STD_T is illustrated with a yellow surface and $\mathbb{E}_T$ with a black line

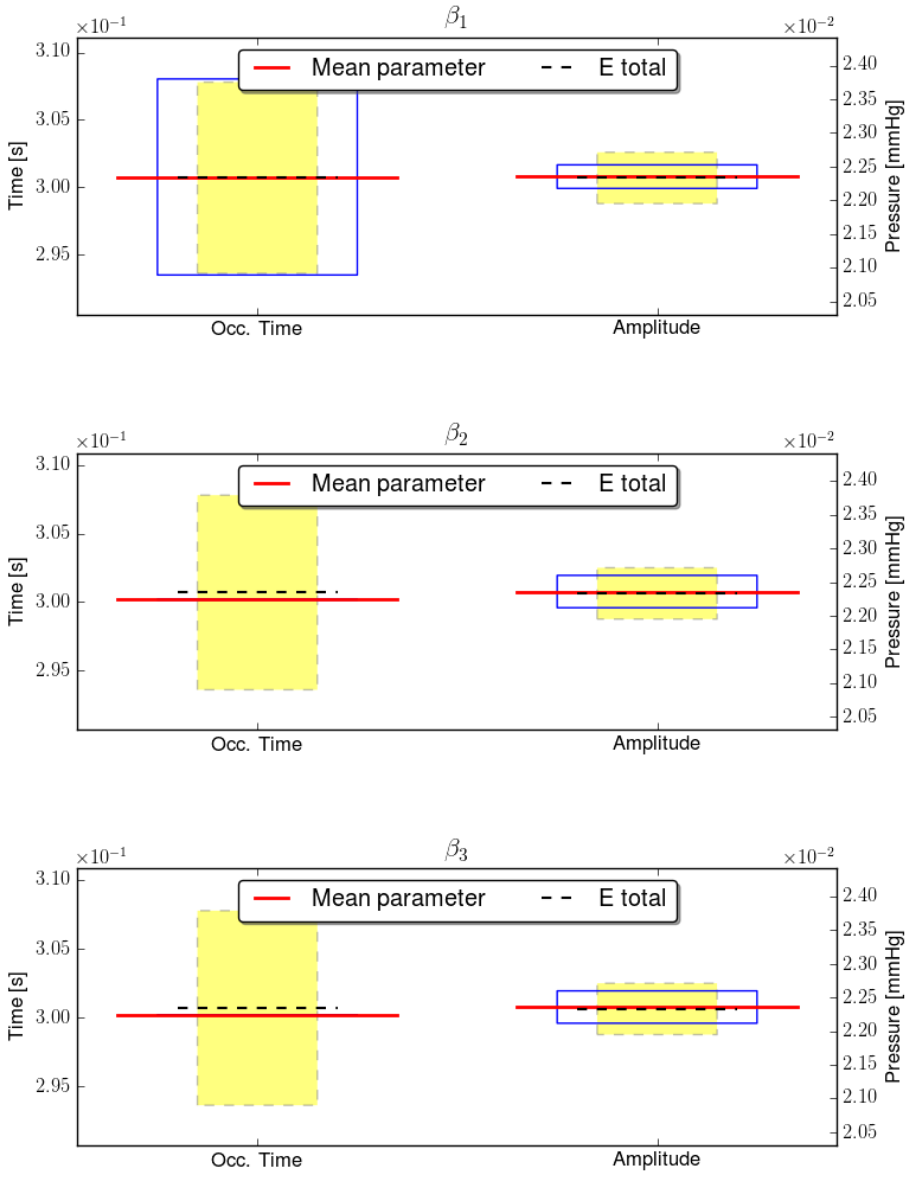

Figure 27: Sensitivity on the second peak (reflected pulse) at measuring point B, where the blue box is STD_i, the red line $\mathbb{E}_i$, STD_T is illustrated with a yellow surface and $\mathbb{E}_T$ with a black line

Verification of the Sensitivity Analysis

To verify the stochastic simulation result, the occurrence times and amplitudes of the pressure peaks are examined.

The peaks of the solution signals are detected (section 3.5.3) for solution u_k of all gPC evaluations. For the time and the amplitude values of each peak, gPCEs are constructed. The sensitivity due to the uncertain β^{Lap} parameters is obtained from these gPCEs (section 3.6). At one hand, the total expected value $\mathbb{E}_T = E[gPCE(\beta_1^{Lap}, \beta_2^{Lap}, \beta_3^{Lap})]$ and the total STD_T of the gPCEs are determined taking all uncertain β^{Lap} parameters into account. At the other hand, the partial expected values and partial STDs for each β_i^{Lap} parameter are calculated. This is done by inserting the expected values of the other two β_i^{Lap} parameters, respectively, in the gPCE expansion. From the resulting polynomial, the expected value and STD of the gPCE are calculated, denoted with the corresponding number of the β^{Lap} parameter, i.e. $\mathbb{E}_1 = E[gPCE(\beta_1^{Lap})]$,$\mathbb{E}_2 = E[gPCE(\beta_2^{Lap})]$ and $\mathbb{E}_3 = E[gPCE(\beta_3^{Lap})]$ and $STD_i = STD(gPCE(\beta_i^{Lap}))$. The standard deviation STD_T shows variability of the simulation result with all uncertain parameters. The STD_i shows the partial variability due to the parameter β_i^{Lap} (see also section 3.6).

In plotting the values of $\mathbb{E}_T$, STD_T, $\mathbb{E}_i$ and STD_i in box plots, the sensitivity of the parameter can be determined, i.e. the amount of partial variability each uncertain value contributes. The β_i^{Lap} parameters can also be compared to each other. In figure 26 and 27 these plots are illustrated for the two peaks at measuring point B. One can see clearly, that only β_1^{Lap} has an effect on the occurrence time of both peaks, the forward directed (figure 26) and the reflected one (figure 27). The amplitude of the first peak is effected by β_1^{Lap} only. After the reflection at point C, the influence of β_2^{Lap}, β_3^{Lap} on the amplitude becomes visible, as the STD_2 and STD_3 increases. As the reflection at the bifurcation is dependent on the waves speeds c_i of the all branches. This effect has been described previously (section 4.1.2) and will be discussed in the following.

To verify the variability obtained by the analysis above a theoretical degree of sensitivity is derived based on the physics and algebra of the system. For this, the areas A_i of the vessels are assumed to be constant. The simulation variabilities, i.e. the STD_i are rescaled as relative STD^*_i:

$$STD^*_i = \frac{STD_i}{\sum_i^D STD_i}, \tag{4.7}$$

where D is the number of uncertain parameters (section 2.2.2).
A similar relative coefficient is applied for the theoretical variations:

$$\Upsilon^*_i = \frac{\Upsilon_i}{\sum_i^D \Upsilon_i}, \tag{4.8}$$

where Υ_i is the variation of occurrence time or amplitude in [%], respectively, due to β_i^{Lap} evaluated on the base of the distributions.

Theoretical Sensitivity on the Occurrence Time

The occurrence time $t_{occ.j}$ of the pressure peak j is determined by the travelling speed of the pulse i.e. the wave speed c_i. As discussed previously, the wave speed in one vessel c_i is proportional to the square root of the β_i^{Lap} of the vessel (equation 4.1).

Using the previous defined relations ship 4.1 and the interval definition of β_i^{Lap} the changes in wave speed c can be derived:

$$\begin{aligned} 0.9\hat{\beta}_i^{Lap} \leq & \beta_i^{Lap} \leq 1.1\hat{\beta}_i^{Lap} \\ 0.9 \leq & \frac{\beta_i^{Lap}}{\hat{\beta}_i^{Lap}} \leq 1.1 \\ c_i \sim \sqrt{\beta_i^{Lap}} \Longrightarrow & \frac{c_i}{\hat{c}_i} \sim \sqrt{\frac{\beta_i^{Lap}}{\hat{\beta}_i^{Lap}}} \\ \sqrt{0.9} \leq & \frac{c_i}{\hat{c}_i} \leq \sqrt{1.1} \\ 0.948 \leq & \frac{c_i}{\hat{c}_i} \leq 1.048 \end{aligned} \tag{4.9}$$

Variation of β_i^{Lap} with $\pm$ 10% leads to an approximated variation of $\pm$ 5% in wave speed c_i. If a pulse j travels through several branches, its wave speed is changed by all β_i^{Lap} parameter of the branches it passes.

The occurrence time $t_{occ.}$ of each point $\hat{x}$ is the fraction of the distances the pulse travels L_{ji} and the wave speed c_i in the branches.

$$t_{occ.} = \sum_i \frac{L_{ji}}{c_i} \Longrightarrow t_{occ.j} \sim \frac{1}{c_i} \tag{4.10}$$

(4.11)

For the discussed case this means, that the variations in occurrence time in the mother branch are only affected by β_1^{Lap}.

E.g. for point B, the theoretical sensitivity coefficients on the occurrence time are for both peaks (forward and reflected):
$\Upsilon_1{}^* = 1$, $\Upsilon_2{}^* = 0$ *and* $\Upsilon_2{}^* = 0$.

The occurrence time in the left daughter branch $i = 2$ is influenced by the variation of β_2^{Lap} and β_1^{Lap} parameter, as the pulse propagates first through the mother branch β_1^{Lap}. This is also applicable for the right daughter branch $i = 3$.

E.g. for point D, the theoretical sensitivity coefficients on the occurrence time are:
$\Upsilon_1{}^* = 2/3$, $\Upsilon_2{}^* = 1/3$ *and* $\Upsilon_2{}^* = 0$.
As the distance travelled in the mother branch is twice as long as in the left daughter branch.

Theoretical Sensitivity on the Amplitude

The amplitude of the pressure peaks is influenced by the β_i^{Lap} in two ways: inside each vessel and by the reflection and transmission at the bifurcation. The total amplitude variation can be calculated by adding both contributions, the change inside the vessel and the change due to reflection/transmission.

A relation for the amplitude variation inside a vessel can be derived from the definition of the characteristic impedance (equation 2.42). As the flow is prescribed as boundary condition, the flow amplitude is assumed to be not effected by the change of β_i^{Lap}. From equation 2.42 and 4.9 the relation between the pressure amplitude P_j^A and the β_i^{Lap} parameters:

$$\begin{aligned} Z_c = \frac{\rho c}{A_0} &= \frac{P}{Q_0} \qquad (recap\ eq.\ 2.42) \\ P^A \sim c &\sim \sqrt{\beta^{Lap}} \\ 0.948 \leq &\frac{P_j^A}{\hat{P}_j^A} \leq 1.048 \end{aligned} \tag{4.12}$$

(4.13)

β_i^{Lap} influences the amplitude of the pressure peaks P_j^A in the same way, as the wave speed c_i, while the pulse is travelling through the vessel.

The amplitudes of the pulses reflected and transmitted at the bifurcation are determined by the reflection coefficient R_f^p 4.4 and the transmission coefficient $T_f^p = 1 - R_f^p$, respectively. R_f^p is a function of the areas A_i (assumed constant) and the wave speeds c_i, which are dependent on β_i^{Lap} (equation 4.9). Setting the variabilities of the wave speeds into the equation 4.4 the contribution in amplitude change of the reflection can be calculated ($P_b^A = P_f^A * R_f^p$). Calculating the sensitivity coefficients shows, that β_1^{Lap} takes influence in a different way than β_2^{Lap} and β_3^{Lap}:

$$0.9 \leq \frac{\beta_i^{Lap}}{\hat{\beta}_i^{Lap}} \leq 1.1$$

$$i = 1 : \quad 1.037 \leq \frac{R_f^p}{\hat{R}_f^p} \leq 0.963 \tag{4.14}$$

$$i = 2,3 : \quad 0.982 \leq \frac{R_f^p}{\hat{R}_f^p} \leq 1.018 \tag{4.15}$$

First, the β_1^{Lap} has more than double the influence as $\beta_{2,3}^{Lap}$. As R_f^p changes with $\mp$3.7% due to β_1^{Lap} but only with $\pm$1.8% due to $\beta_{2,3}^{Lap}$. Second, the relation ship between R_f^p and β_1^{Lap} is inverse proportional, i.e increased β_i^{Lap} leads to a decreased amplitude.

E.g. the total sensitivity coefficients at point B for the forward propagation pulse are $\Upsilon_1{}^* = 1.0$, $\Upsilon_2{}^* = 0$ *and* $\Upsilon_2{}^* = 0$.
For the backward directed wave they become:

$$\Upsilon_1 \approx 5.0\% - 3.7\% = 1.3\%, \quad \Upsilon_{2,3} \approx 1.8\%, \quad \sum_i^D \Upsilon_i = 4.9\%$$
$$\Upsilon_1{}^* = 0.26, \quad \Upsilon_2{}^* = 0.37, \quad \Upsilon_3{}^* = 0.37$$

The transmission coefficient is defined as $T_f^p = 1 - R_f^p$ and can be stated as:

$$T_f^P = \frac{2(\frac{A_2}{c_2} + \frac{A_3}{c_3})}{\frac{A_1}{c_1} + \frac{A_2}{c_2} + \frac{A_3}{c_3}} \tag{4.16}$$

With it, the sensitivity on the amplitude of the transmitted waves can be estimated ($P_t^A = P_f^A T_f^p$). The coefficients change in the ranges:

$$0.9 \leq \frac{\beta_i^{Lap}}{\hat{\beta}_i^{Lap}} \leq 1.1$$

$$\begin{aligned} i = 1 : \quad 0.96 \leq \frac{T_f^p}{\hat{T_f^p}} \leq 1.04 \\ i = 2,3 : \quad 1.02 \leq \frac{T_f^p}{\hat{T_f^p}} \leq 0.98 \end{aligned} \tag{4.17}$$

E.g. the total sensitivity coefficients on the amplitude at point D for the transmitted pulse become:

$$\Upsilon_1 \approx \pm 5.0\% + \pm 4\% = \pm 9\%, \quad \Upsilon_2 \approx \pm 5.0\% + \mp 2\% = \pm 3\%,$$
$$\Upsilon_3 \approx \mp 2\% \quad \sum_i^D \Upsilon_i = 14\%$$
$$\Upsilon_1{}^* = 0.65, \quad \Upsilon_2{}^* = 0.21, \quad \Upsilon_3{}^* = 0.14 \tag{4.18}$$

Comparison of the Sensitivity Coefficients STD* and Υ*

All theoretical sensitivity coefficients Υ_i* and the relative STD*s for the peaks at point A-E are listed in table 6. Figures 28 and 29 show the evaluated data at measuring point B and D respectively as bar plots.
The sensitivities of the occurrence time matches perfectly. The theoretical values Υ_i* for the amplitude of the transmitted waves are differing at measuring point D and E. As the theoretical values are evaluated under the assumption of constant areas A_i and with linear reflection and transmission coefficients, the disagreement seems plausible.

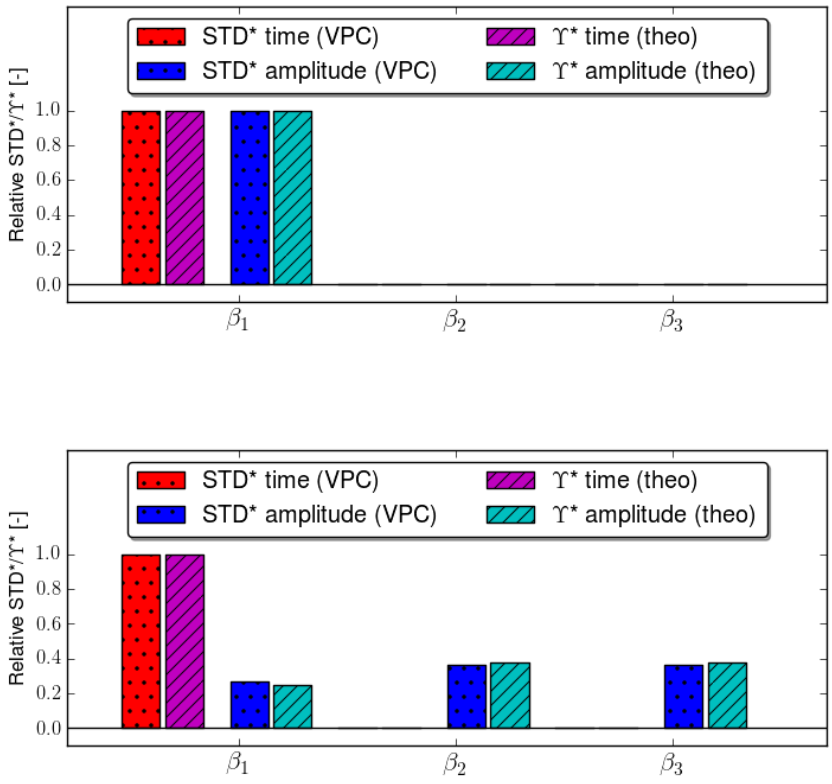

Figure 28: Comparison of the simulation STD* and the theoretical Υ_i* at measuring point B, for the forward directed (at the top) and the reflected (at the bottom) pressure pulse

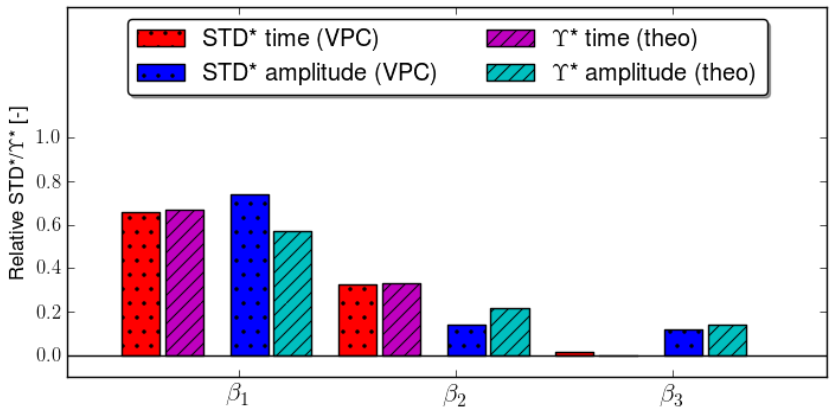

Figure 29: Comparison of the simulation STD* and the theoretical Υ_i* at measuring point D

measuring points		β_1^{Lap} STD*	β_1^{Lap} ϒ*	β_2^{Lap} STD*	β_2^{Lap} ϒ*	β_3^{Lap} STD*	β_3^{Lap} ϒ*
Time							
point A	forward	0.00	0.00	0.00	0.00	0.00	0.00
	reflected	1.00	1.00	0.00	0.00	0.00	0.00
point B	forward	1.00	1.00	0.00	0.00	0.00	0.00
	reflected	1.00	1.00	0.00	0.00	0.00	0.00
point C		0.96	1.00	0.02	0.00	0.02	0.00
point D		0.66	0.66	0.32	0.66	0.01	0.00
point E		0.50	0.50	0.50	0.50	0.00	0.00
Amplitude							
point A	forward	1.00	1.00	0.00	0.00	0.00	0.00
	reflected	0.26	0.26	0.37	0.37	0.37	0.37
point B	forward	1.00	1.00	0.00	0.00	0.00	0.00
	reflected	0.26	0.26	0.37	0.37	0.37	0.37
point C		0.75	0.70	0.12	0.14	0.12	0.00
point D		0.74	0.65	0.14	0.21	0.12	0.14
point E		0.74	0.65	0.14	0.21	0.12	0.14

Table 6: Comparison of the simulation STD* and the theoretical Υ_i* for all measuring points A-E

99%-Confidence Interval

For the test case, 99% confidence intervals are calculated, i.e $\alpha = 1.0$ for each β_i^{Lap} at each peak following the procedure described in section 3.6. Figure 30 illustrates these confidence intervals for measurement point B, in addition with the total expected values of the pressure signals. The confidence intervals state a prediction of what one expects to happen with 99% confidence.

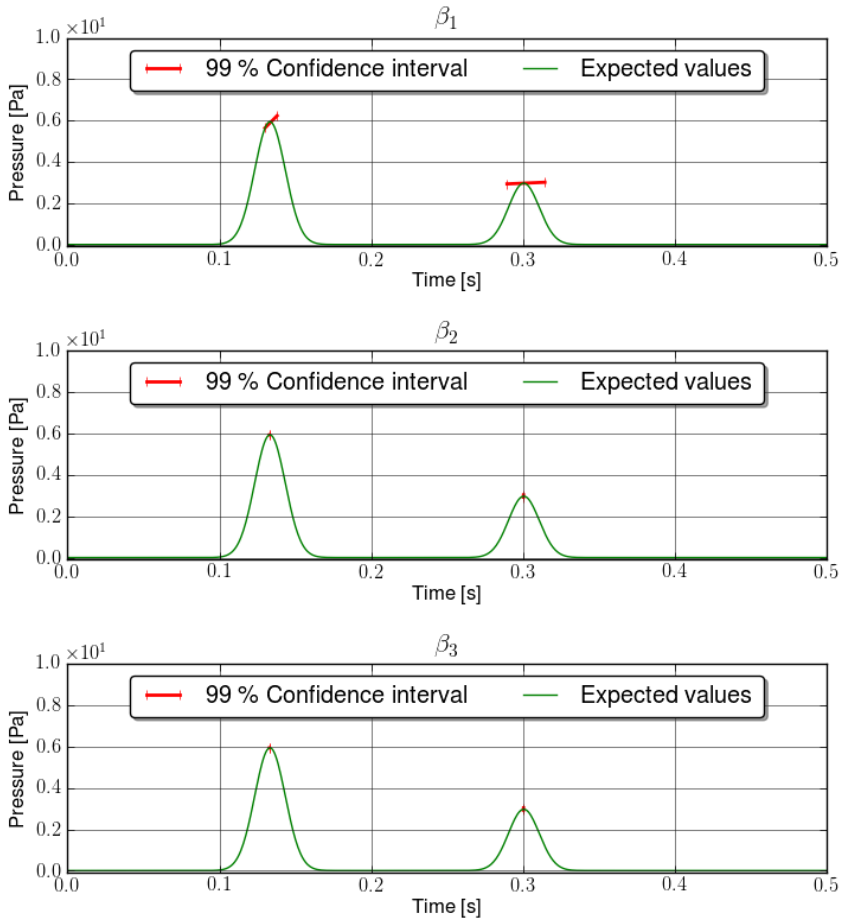

Figure 30: 99%-Confidence intervals for the there β_i^{Lap}, plotted over the total expected values at measuring point B

4.1.4. Results of Case I

Case I is used for the verification of the simulation approach. Due to the simple network setup, the deterministic and the stochastic solution can be evaluated with the analytical solutions.

First the solution of the deterministic simulation is checked, to verify vascular1DFlow. The analytic solution and the result of the work of D. Xiu and S.P. Sherwin [38] are used as comparator basis. It was found that the solution of vascular1DFlow matches well, if the number of grid nodes N is sufficiently high. The best agreement of simulation accuracy and computational time is achieved for N = 200.

Thereafter, the solution of an uncertain simulation calculated with the elaborated simulation approach is tested. Three uncertain parameters are defined, one for each vessel in the network. The impact of the uncertain parameters on the pressure solution is investigated by means of a sensitivity analysis. The variabilities in simulation results due to the parameters are evaluated and verified with plots from D. Xiu and S.P. Sherwin [38]. Additionally, the evaluated values are compared to an analytically derived sensitivity coefficient. The comparisons show that the results of the sensitivity analysis based on the simulation result of VPC are reliable. In addition, different methods of presenting the data have been examined, i.e. box plots and the combination of confidence intervals with total expected values.

Some additional results found are:

- The order of the gPCE does not have to be very high
- With peak detection, the sensitivity can be investigated in regards to occurrence time and amplitude
- Sensitivity of flow and pulse waves are dependent on the measuring point *e.g. at point E, the uncertainty in β_3 could be neglected, but not at point C.*

4.2. Case II - Simulation of the Human Arterial Tree

The human systemic arterial tree, represented by 49 vessels, is studied in the second case. The network is based on the data published by Stergiopulos et al. [28]. The investigation purpose of the study is the estimation of variability of the pressure waves (total, forward and backward) in the ascending aorta due to ageing. The backward contribution of the pressure waves, caused by reflections in the arterial tree are of particular concern. The effect will be first investigated with two deterministic simulations. Thereafter, a stochastic VPC simulation, will be used to study the contributions of different body compartments to the variability of the pressure waves.

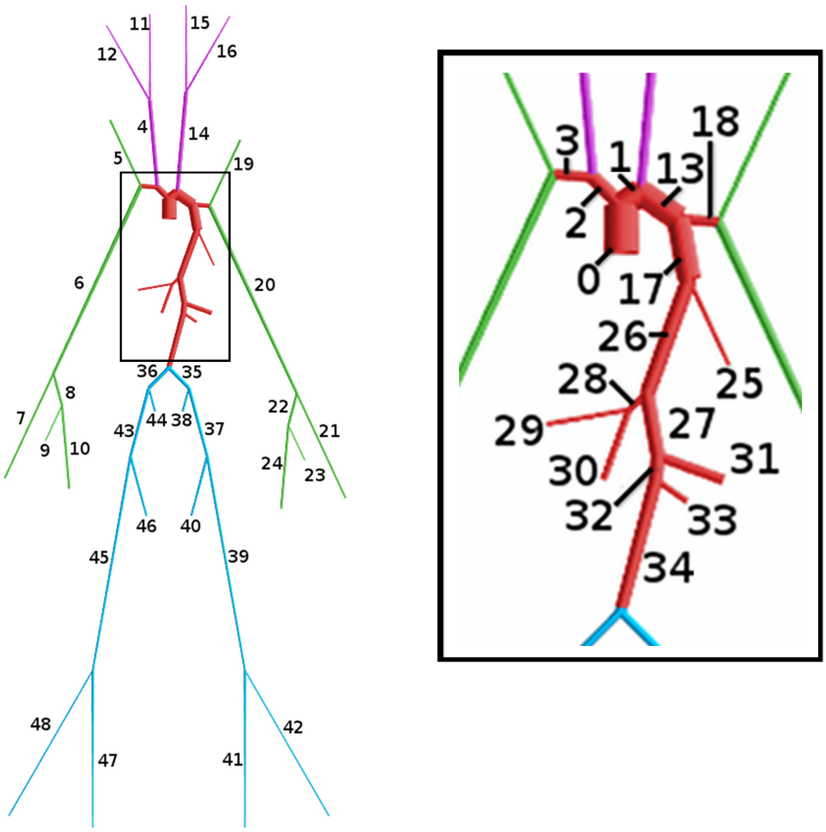

Figure 31: Overview of the network concerned in Case II. The branches are coloured according to the uncertainty groups they belong in; red: the aortic arch, purple: the head arteries, green: the arm arteries and blue: the legs arteries

4.2.1. Simulation Setup

The arterial tree considered is illustrated in figure 31. The deterministic and stochastic simulations are evaluated at the beginning of the ascending aorta (branch with the Id 0). The system is assumed to be inviscid with the viscosity $\mu = 0.004 kg/m^3$ and for the velocity profile, the shape of Poiseulle flow is applied (section 2.1.1). Grid nodes of all vessels are optimized, regarding the CFL number, using the approach presented in section 3.8.1.

Boundary Conditions

At the open end of the ascending aorta, the volumetric flow Q_h from the heart is prescribed as only inflow boundary condition. The inflow has a typical physiological shape and is composed form several continuous functions. The amplitudes, timing and periods of the inflow signal are chosen according the data of Stergiopulos et al. [28]. The inflow signal is illustrated in figure 32.

Furthermore, the boundary at the ascending aorta is defined as non absorbing, i.e. waves coming from the system are reflected. All terminal boundary conditions at the end of the arterial tree are implemented as absorbing boundary conditions. This ensures, that the backward contributions in the ascending aorta are caused by reflections in the arterial tree exclusively.

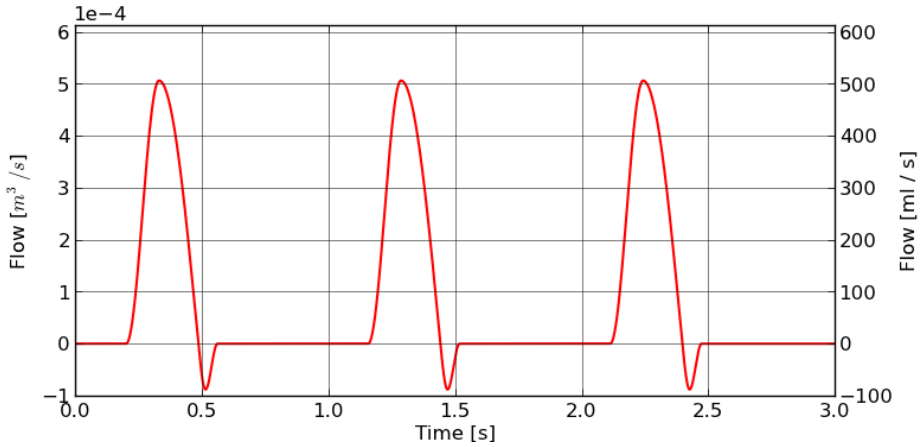

Figure 32: Volumetric inflow boundary condition applied in case II

Material Data of the Branches

The basic material parameters of all vessels are selected from Stergiopulos et al. [28]. However, the wall thickness h and the Youngs's modulus E from each vessel are taken from Wang and Parker [30], who use the data published from Stergiopulos et al. [28] to calculated these parameters. The wall thickness h and the Youngs's modulus E are used to calculated the stiffness parameter β^{Lap} (equation 2.11) for the applied compliance (equation 2.10). All vessel data is listed in table 8.

Effects of Ageing

The compliance of the vascular system decreases with age. The ration of change in compliance between a young and an old person is over 50% [17]. In figure 33, the arterial compliance of persons with different ages, is illustrated. The changes in compliance of the vascular tree is said to lead to an increase in pressure amplitude of backward propagating waves in the ascending aorta [25]. This effect leads to isolated systolic hypertension, i.e. an increase of the systolic total pressure in the ascending aorta to over 150-160 [mmHg], whereas the diastolic pressure stays at a moderate level around 80-95 [mmHg].

[NB: Systolic pressure is defined as the highest amplitude of the pressure pulse and the diastolic pressure as the lowest pressure amplitude in one cycle.]

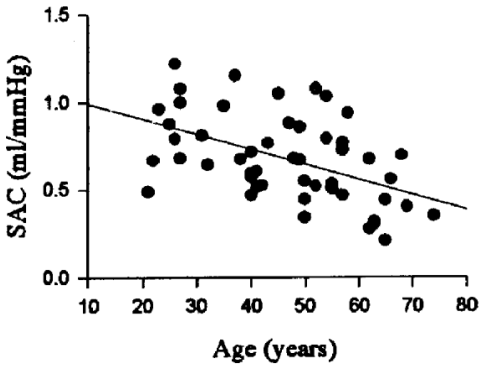

Figure 33: Systemic arterial compliance (SAC) of persons with different age. Figure taken from Liang et al. [17]

The relation of the vessel compliance to the given material parameters is determined by the applied compliance model (equation 2.10). The compliance is inverse proportional to the stiffness parameter β^{Lap}, which is a direct function of the Young's modulus. Thus a relation between the compliance C and the Young's modulus E is given with:

$$C \sim \frac{1}{E} \tag{4.19}$$

As the compliance decreases with age, the Young's modulus E increases, i.e. the artery become stiffer.

The network data used for the simulation in case II represents a young person [28], with Young's modulus E. The Youngs's modulus E_{young} applied in the simulations for a young person is therefore:

$$E_{young} = 1.0\ E \tag{4.20}$$

According to equation 4.19 and the fact that the compliance, decreases with age, the Youngs's modulus E_{old} in the simulations for an old person is set to:

$$E_{old} = 2.3\ E \tag{4.21}$$

The total decrease of compliance in this case is about 57%, which is in the range of the data given in figure 33.

Deterministic simulation set up
Two deterministic simulations with the given network for an old and a young person with Young's moduli E_{young} and E_{old} according to equations 4.20 and 4.21 respectively, are run. With the results of these simulations, the changes in pressure waves in the ascending aorta due to ageing are determined. Additionally, they are used for estimation and verification of the stochastic simulation results.

Uncertain simulation set up
To identify the contributions of different body compartments to the changes in pressure wave amplitudes in the aorta, uncertainty in the Young's modulus is defined. The variability of Young's moduli in each vessel is defined as uniformly distributed random variables. The interval limits of the random variables are set to the young (4.20) and old (4.21) Young's moduli values:

$$z_i(E_i) = Uniform[1.0\ E_i, 2.3\ E_i] \tag{4.22}$$

Hence, the expected value of each Young's modulus distribution corresponds to the Young's modulus of a middle aged person.
The network of 49 branches is organized into four uncertainty groups according to their location in the body. The Young's moduli of each group are changed at the same time, to isolate the changes due to the compartments as a hole. Thus, the random variables necessary for this study can be reduced from 49 to 4, all defined in the same manner:

$$z_j = Uniform[1.0, 2.3], \tag{4.23}$$

where j is group index.
In each evaluation, before the simulation is started, all Young's moduli of each group, are multiplied with their corresponding value z_{jk}. Changing the Young's moduli of all groups with the same values of z_{jk} corresponds to equal ageing of the body compartments. With the definition of the uncertainty groups, the body compartments can vary in age independently. Thus the effects of ageing due to the compartments can be identified with a sensitivity analysis.

The different body compartments are:

- Aortic arch arteries and branches
- Head arteries
- Arm arteries
- Leg arteries

All compartments and the associated vessels, are listed in table 7. In the illustration of the network (figure 31), the uncertainty groups can be identified by color.
The right vertebral artery (Id 5) and left vertebral artery (Id 19) are included in the uncertainty group of the arm arteries, although they actually lead to the head.

The results of the stochastic simulations are evaluated by means of a sensitivity analysis as described in section 3.6. The sensitivity analysis is mainly focused on the total and the backward contribution of the pressure in the ascending aorta (wave separation see sections 2.1.4 and 3.5.2). The systolic and the diastolic pressures are detected (section 3.5.3) and the variation in occurrence time and amplitude of these peaks is investigated.

The vascular polynomial chaos simulation is run with a gPCE order of three. In total 120 deterministic simulation are run for the evaluation process.

Ids of branches in uncertainty group 1: the aortic arch	Ids of branches in uncertainty group 2: the head arteries
0 1 2 3 13 17 18 25 26 27 28 29 30 31 32 33 34	4 11 12 14 15 16

Ids of branches in uncertainty group 3: the arm arteries	Ids of branches in uncertainty group 4: the legs
5 6 7 8 9 10 19 20 21 22 23 24	35 36 37 38 39 40 41 42 43 44 45 46 47 48

Table 7: Classification of the branches in the network into four uncertainty groups according to their location in the body. The uncertainty groups are illustrated with different colours in figure 31

Id	name	L [m] (length)	r_p [mm] (proximal radius)	r_d [mm] (distal radius)	h [mm] (wall thickness)	E [MPa/m] (Young's Modulus)
0	Ascending Aorta	0.04	14.7	14.4	1.63	0.4
1	Aortic Arch I	0.02	11.2	11.2	1.26	0.4
2	Brachiocephalic	0.034	6.2	6.2	0.8	0.4
3	R.Subclavia I	0.034	4.23	4.23	0.67	0.4
4	R.Carotid	0.177	3.7	3.7	0.63	0.4
5	R.Vertebral	0.148	1.88	1.83	0.45	0.8
6	R.Subclavia II	0.422	4.03	2.36	0.67	0.4
7	R.Radial	0.235	1.74	1.42	0.43	0.8
8	R.Ulnar I	0.067	2.15	2.15	0.46	0.8
9	R.Interosseous	0.079	0.91	0.91	0.28	1.6
10	R.Ulnar II	0.171	2.03	1.83	0.46	0.8
11	R.Internal Carotid	0.176	1.77	0.83	0.45	0.8
12	R.External Carotid	0.177	1.77	0.83	0.42	0.8
13	Aortic Arch II	0.039	10.7	10.7	1.15	0.4
14	L.Carotid	0.208	3.7	3.7	0.63	0.4
15	L.Internal Carotid	0.176	1.77	0.83	0.45	0.8
16	L.External Carotid	0.177	1.77	0.83	0.42	0.8
17	Thoracic Aorta I	0.052	9.99	9.99	1.1	0.4
18	L.Subclavian I	0.034	4.23	4.23	0.66	0.4
19	L.Vertebral	0.148	1.88	1.83	0.45	0.8
20	l.Subclavian II	0.422	4.03	2.36	0.67	0.4
21	L.Radial	0.235	1.74	1.42	0.43	0.8
22	L.Ulnar I	0.067	2.15	2.15	0.46	0.8
23	L.Interosseous	0.079	0.91	0.91	0.28	1.6
24	L.Ulnar II	0.171	2.03	1.83	0.46	0.8
25	Intercostales	0.08	2	1.5	0.49	0.4
26	Thoracic Aorta II	0.104	6.75	6.45	1	0.4
27	Abdominal I	0.053	6.1	6.1	0.9	0.4
28	Celiac I	0.02	3.9	2	0.64	0.4
29	Gastric	0.071	1.8	1.8	0.45	0.4
30	Splentic	0.063	2.75	2.75	0.54	0.4

Table 8: Material parameters of all vessels in the network, data according to Stergiopulos et al. [28] and Wang and Parker [30]

continuation of table 8

Id	name	L [m]	r_p [mm]	r_d [mm]	h [mm]	E [MPa/m]
31	Superior Mesenteric	0.059	4.35	4.35	0.69	0.4
32	Abdominal II	0.02	6	6	0.8	0.4
33	R.Renal	0.032	2.6	2.6	0.53	0.4
34	Abdominal IV	0.116	5.8	5.2	0.75	0.4
35	R.Common Iliac	0.058	3.68	3.5	0.6	0.4
36	L.Common Iliac	0.058	3.68	3.5	0.6	0.4
37	L.External Iliac	0.144	3.2	2.7	0.53	0.8
38	L.Internal Iliac	0.05	2	2	0.4	1.6
39	L.Femoral	0.443	2.59	1.9	0.5	0.8
40	l.Deep Femoral	0.126	2.55	1.86	0.47	0.8
41	L.Posterior Tibial	0.321	2.47	1.41	0.45	1.6
42	L.Anterior Tibial	0.343	1.3	1.3	0.39	1.6
43	R.External Iliac	0.144	3.2	2.7	0.53	0.8
44	R.Internal Iliac	0.05	2	2	0.4	1.6
45	R.Femoral	0.443	2.59	1.9	0.5	0.8
46	R.Deep Femoral	0.126	2.55	1.86	0.47	0.8
47	R.Posterior Tibial	0.321	2.47	1.41	0.45	1.6
48	R.Anterior Tibial	0.343	1.3	1.3	0.39	1.6

Table 9: continuation of table 8: Material parameters of all vessels in the network, data according to Stergiopulos et al. [28] and Wang and Parker [30]

	systolic pressure [mmHg]		diastolic pressure [mmHg]	
	young	old	young	old
total signal	112.44	150.29	75.45	76.18
backward contribution	17.67	31.53	5.18	4.61
forward contribution	36.05	62.23	10.11	11.52

Table 10: Systolic and diastolic pressure obtained in the two deterministic simulations corresponding to a young and an old person

4.2.2. Results and Discussion of the Deterministic Simulations

The pressure and flow curves with their forward and backward contributions obtained with the deterministic simulations are illustrated in figures 34 and 35. The pressure and flow signals of the deterministic simulations show reliable curves with correct physiological systolic and diastolic pressure levels (see e.g. figure 1 in Schiffrin [25]). The form of the curve for the young person looks similar to the curves obtained by Stergiopulos et al. [28]. For the old person, the pressure curve is similar to the results obtained by or Westerhof et al. [31]. Any discrepancies may be attributed to the different peripheral boundary conditions applied.
The values of systolic and diastolic pressure of the deterministic signals are listed in table 10.

Compared to values in literature, the values of the young test case are in range with young healthy test subjects: systolic pressure 110-120 mmHg (simulation: 112.44 mmHg) and diastolic pressure 70-80 mmHg (simulation: 75.45 mmHg), e.g. found in the work of Nichols et al. [20].

The simulation of the old person shows isolated systolic hypertension as described by Schiffrin [25], which is an effect of increased arterial stiffness due to ageing. The changes in compliance of the vascular tree is said to lead to an increases in pressure amplitude of backward propagating waves in the ascending aorta. This effect is due to the changed reflection coefficients at bifurcations and narrowings (see also section 4.1). In the two deterministic simulations, the amplitude of the systolic peak of the backward contribution almost doubled as the material parameters changed. Values of test subjects with this pathology determined by Nichols et al. [20] are: systolic pressure 150-160 mmHg (simulation: 150.29 mmHg), diastolic pressure 80-90 mmHg (simulation: 76.18 mmHg).

However, the systolic pressure seems to be very high for this test case, as only reflections in the arterial tree itself and not from the periphery are accounted for. This may be due to an overestimated change in compliance due to ageing. The boundary condition at the inflow point (100% reflection condition) also accounts for the high pressure. This condition is not physiological, as in reality, the reflection is determined by the opening and closing of the aortic valve. Thus, the timing of the reflected pulses and the amplitude is dependent of the movement of the aortic valve. If the aortic valve is closed, the pulses are reflected (similar to the applied condition). But, if the aortic valve (during the systole) is open, the pulses can propagate into the heart and are reflected at the walls of the left ventricle. The inside the heart reflected backward contribution will have a phase shift to later occurrence times, and consequently, the systolic pressure will decrease. In the plots of the flow (figures 35), the total reflection condition can be identified, as the forward and backward contributions incline and decline simultaneously. This could be improve with a varying elastance heart model combined with a aortic valve model [23]. The influence of the heart as reflector is investigated in the work of Wang and Parker [30].

Nevertheless the results of the deterministic simulations show the capability and ability of vascular1DFlow to simulate this kind of networks appropriately.

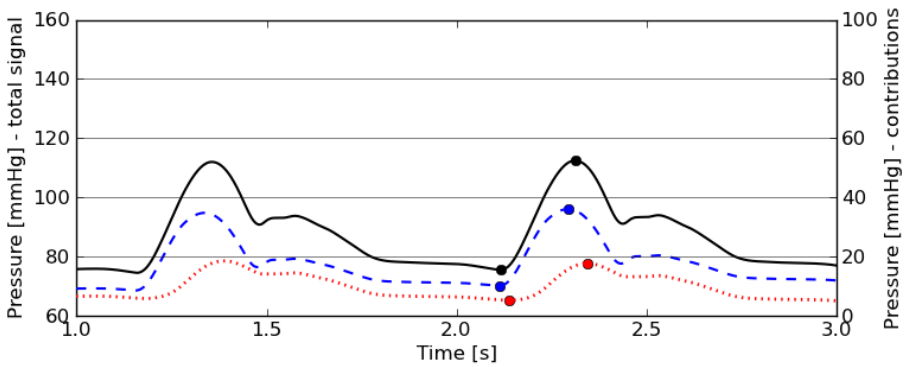

(a) Pressure signals corresponding to a young person, with the total pressure as black solid line, the forward contribution as blue dashed line, and the backward contribution as red dotted line.

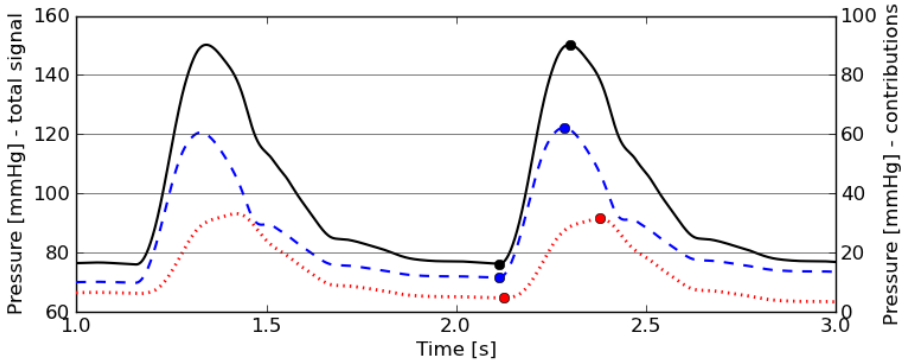

(b) Pressure signals corresponding to an old person, with the total pressure as black solid line, the forward contribution as blue dashed line, and the backward contribution as red dotted line.

Figure 34: Pressure signals in the ascending aorta of a deterministic simulation with different material parameters corresponding to a young (34(a)) and an old (34(b)) person. The systolic and diastolic peaks used in the sensitivity analysis of the uncertain solution are indicated with small circles

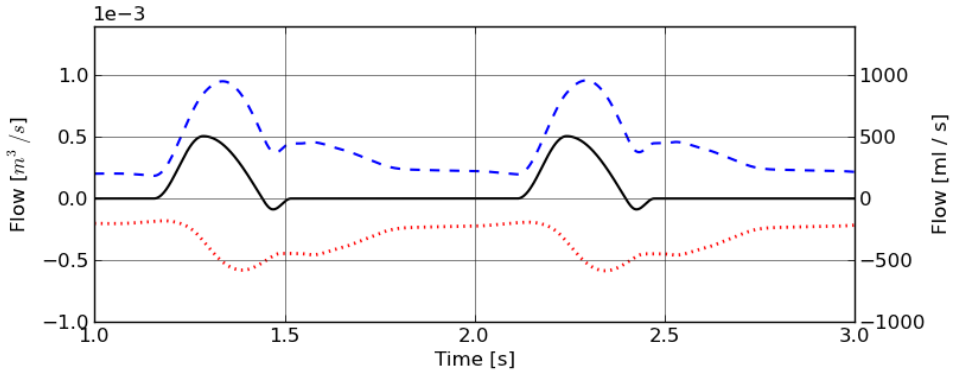

(a) Flow signals corresponding to an young person, with the total flow as black solid line, the forward contribution as blue dashed line, and the backward contribution as red dotted line.

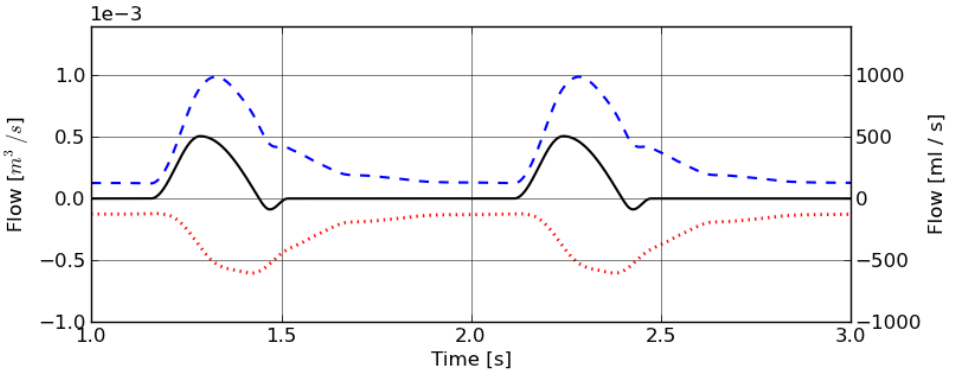

(b) Flow signals corresponding to an old person, with the total flow as black solid line, the forward contribution as blue dashed line, and the backward contribution as red dotted line.

Figure 35: Flow signals in the ascending aorta of a deterministic simulation with different material parameters corresponding to a young (35(a)) and an old (35(b)) person.

4.2.3. Results and Discussion of the Vascular Polynomial Chaos Simulations

The results of vascular polynomial chaos simulation of the second case are more complex and demanding to interpret than the ones obtained in the simple test case I (section 4.1), as there exit no analytic solutions. The results of the deterministic simulations described above are used as reference and help to develop a perception of expectations.

For the analysis of sensitivity, the methods described in section 3.6 are applied: investigation of the total signal, evaluation of extracted peak points and creation of confidence intervals. The sensitivity measures, expected values and STD are calculated, on one hand taking all sensitivity groups into account (denoted as total expected values/STD) and on the other hand for each sensitivity group separately (denoted as partial expected values/STD). The procedure is explained in 3.6 and 4.1.3.
All expected values and STDs (total and partial) of the pressure signal and its backward contribution are illustrated in figures 36 and 37.
[NB: the total sensitivity measures are denoted with 'all groups', whereas the partial sensitivity measures bear their group name.]
The systolic and diastolic peaks are detected and the sensitivities on occurrence time and amplitude are evaluated for each uncertainty group and listed in tables 11 - 14. The box plots of those values for the pressure signal and its backward contribution are illustrated in figures 38,39(Systole) and 40, 41 (Diastole). In addition, 99%-Confidence intervals are created for the systolic and diastolic peaks and plotted over the total expected values (figure 42).

Some particular characteristics of the results and some interpretations are summarized below.

- Expected values and STD of the total signals:
  - The form of the total expected signals when compared with the deterministic solution seems reliable. But the pressure level is slightly lower than in the deterministic case.
  - The partial expected values (coloured lines in figures 36 and 37) are for all uncertainty groups higher then the total expected value (black line in figures 36 and 37). This may be due to the non linearity of the system. Additionally, during evaluation of a partial expected value for one uncertainty group, the other uncertainty distributions are fixed to their mean value, i.e. to a middle aged person. And only the vessels of the specific uncertainty group are running through the ageing process. Which will lead to higher expected values, as some cases *e.g. all uncertainty groups are young* are not reflected in the partial expected values.
  - The uncertainty group 'aortic arch' is the only one with a pulsatile STD contribution, i.e. as the STD increases simultaneously with the pressure pulse. This may come from the small distance to the measuring point.
  - The STDs of the other uncertainty groups stay almost constant on a level of about 5 mmHg. This means, that the uncertainty in these parameters influences the signal at every point in time with equal magnitude. Consequently, the change of

the pressure wave form can be mostly attributed to a change in compliance in the aortic arch.

  - In both the STDs (total and backward) of the Arm arteries a small hill occur (at t≈1.5 t≈2.4). It is slightly before the point in time, where the deterministic simulations show, a small notch (young person) or a change in slope (old person), this point is also called dicrotic notch. There may be a connection, which could be identified by further investigations with another test case.

- Systolic peak evaluation:
  - The relative position of all partial expected values of the backward contribution (figure 39) and the total pressure peaks (figure 38) are similar. The partial STDs are also similar for both peaks, except, that the STD of the aortic arch for the total pressure peak is more dominant, i.e. the STDs of the aortic arch slightly increase whereas the other STDs slightly decrease, in particular the occurrence times of the legs.
  - As in the other plots, shown here again, the aortic arch has the highest influence on the amplitude of the systolic peak.

- Diastolic peak evaluation:
  - The head arteries show almost no influence on the occurrence time of the peak.
  - All other uncertainty groups seem to have the same influence on the occurrence time
  - The amplitude is influenced by all groups with approximately the same magnitude.
  - As for the systolic peak, the variabilities in the backward contribution of the uncertainty groups are reflected in the total signal.

- 99% confidence interval systolic and diastolic peak evaluation:
  - Within the confidence intervals of all uncertainty groups except the 'aortic arch' the total expected value are increased, i.e. as they are above the black lines.
  - The aortic arch has the highest effect on the amplitude deviation of the peaks, as the interval length is the longest.
  - The variability of the occurrence time (i.e. the comparison of the slopes of the interval lines) of the systolic pressure is small compared to the diastolic pressure.

The results of the sensitivity analysis show, that in this configuration none of the body compartments could be neglected in the simulation set up, to evaluate the pressure signals in the ascending aorta. The body compartment aortic arch seems to have the highest influence on the form of the pressure signals. However, this does not mean, that uncertainties of all vessels in all body compartments have to be taken into account. To analyse the impact of uncertainty completely, further investigations are necessary. A new simulation set up for

this could include uncertain parameters for all vessels in the arterial tree. In the sensitivity analysis, one could group the vessels again into compartments, but it would then be possible to asses the partial contribution of each vessel to the sensitivity of their compartments and to the total sensitivity. In doing so, one could identify those vessels, where the uncertainty may be neglected. This would help to create patient specific wave propagation simulations, as not for all vessels patient data would have to be evaluated.

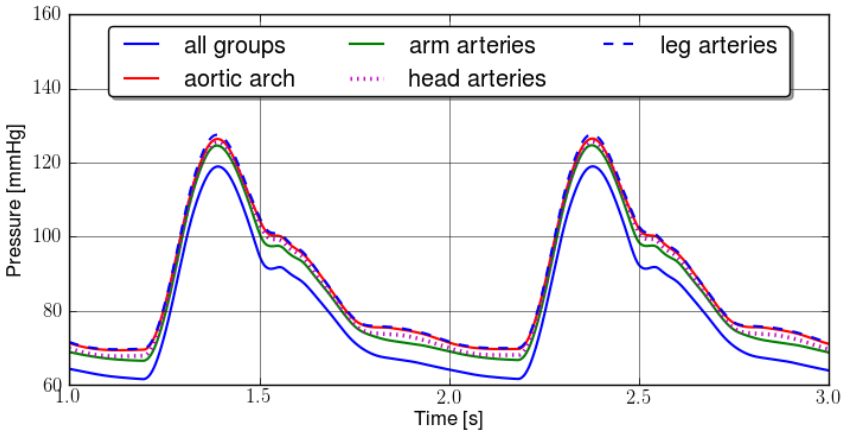

(a) Expected values of the total pressure signal, with the total and partial expected values corresponding to the uncertainty groups

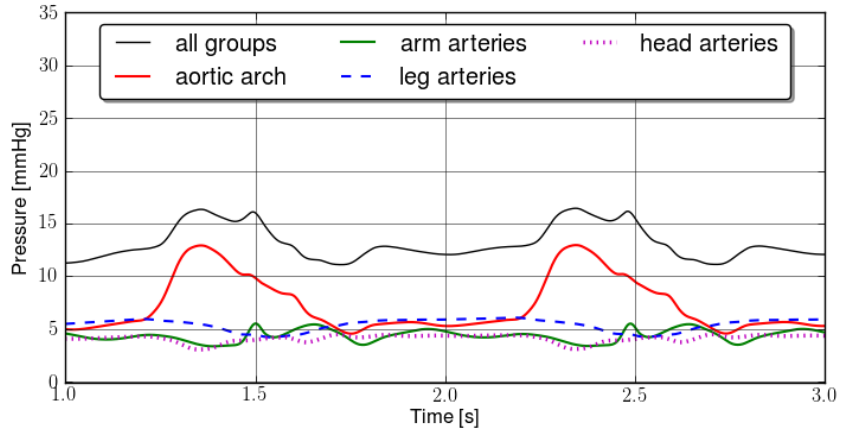

(b) STD of the total pressure signal, with the total and partial STDs corresponding to the uncertainty groups

Figure 36: VPC result for the total pressure signal in the ascending aortic; the expected values 36(a) and the STDs 36(b)

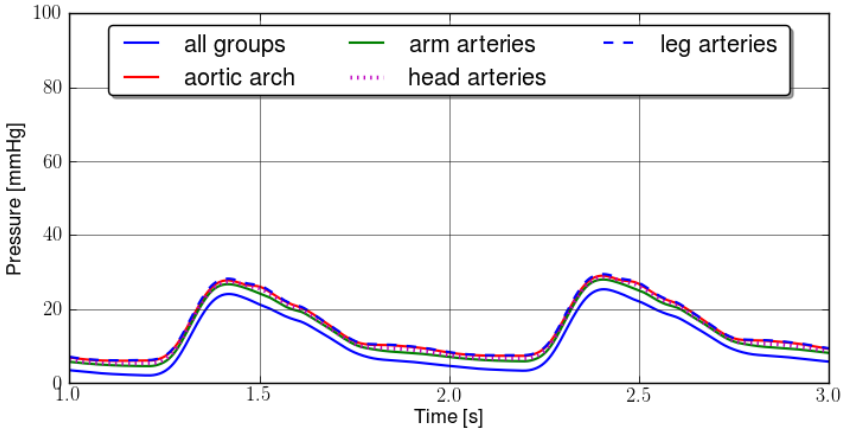

(a) Expected values of the backward contribution, with the total and partial expected values corresponding to the uncertainty groups

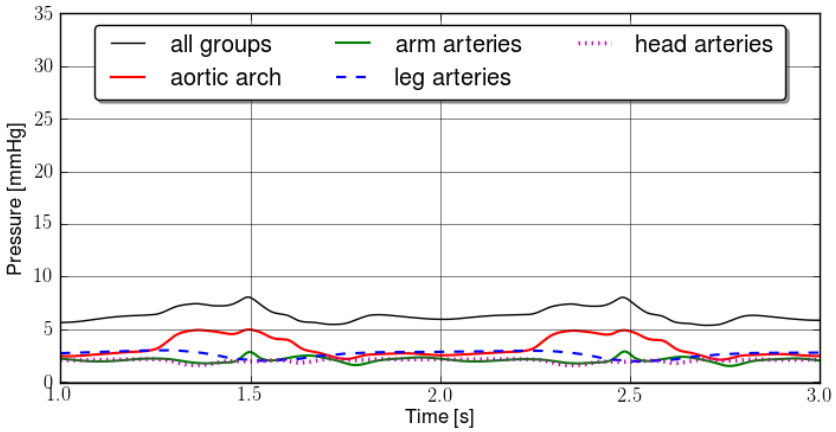

(b) STD of the backward contribution, with the total and partial STDs corresponding to the uncertainty groups

Figure 37: VPC result for the backward contribution of the pressure signal in the ascending aortic; the expected values 37(a) and the STDs 37(b)

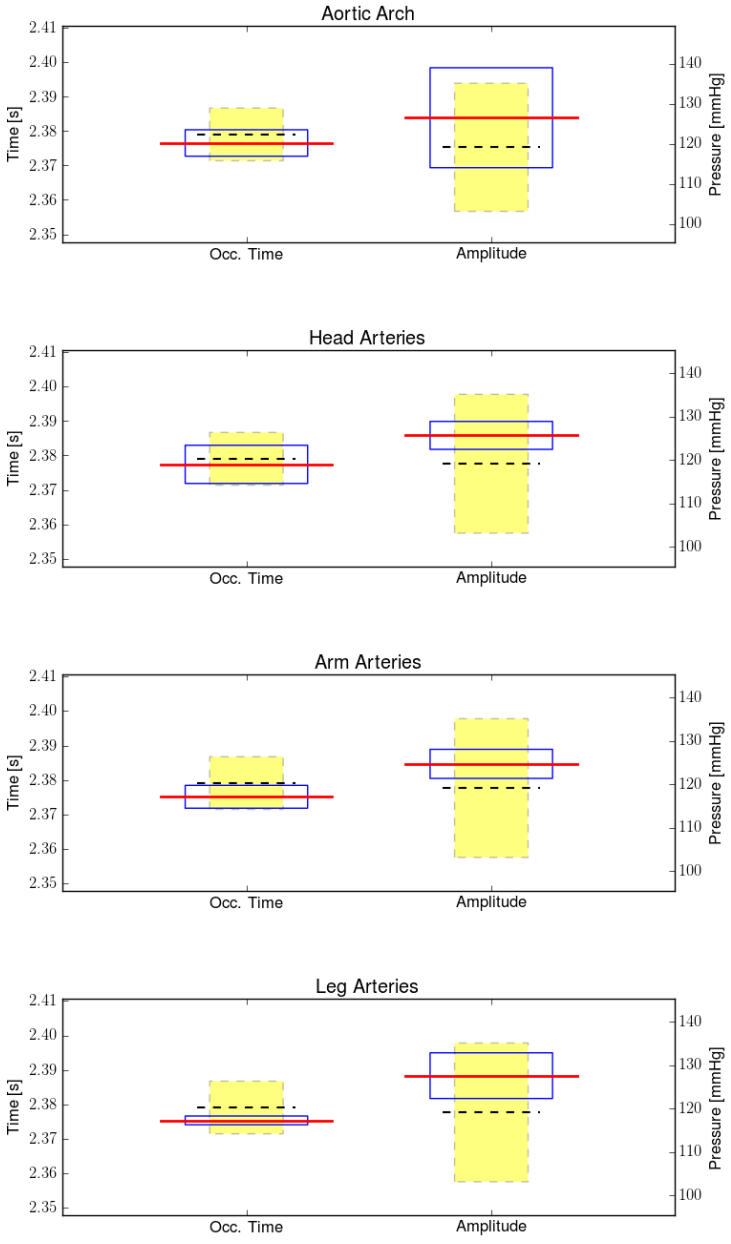

Figure 38: Box plot of the expected values and STD of the occurrence time and amplitude of the **systolic peak in the total pressure signal**, for the individual uncertainty groups. The black dotted line is the total expected value with its STD as yellow plane. The red line is the expected value, and the blue box the STD, receptively, of the uncertain parameter

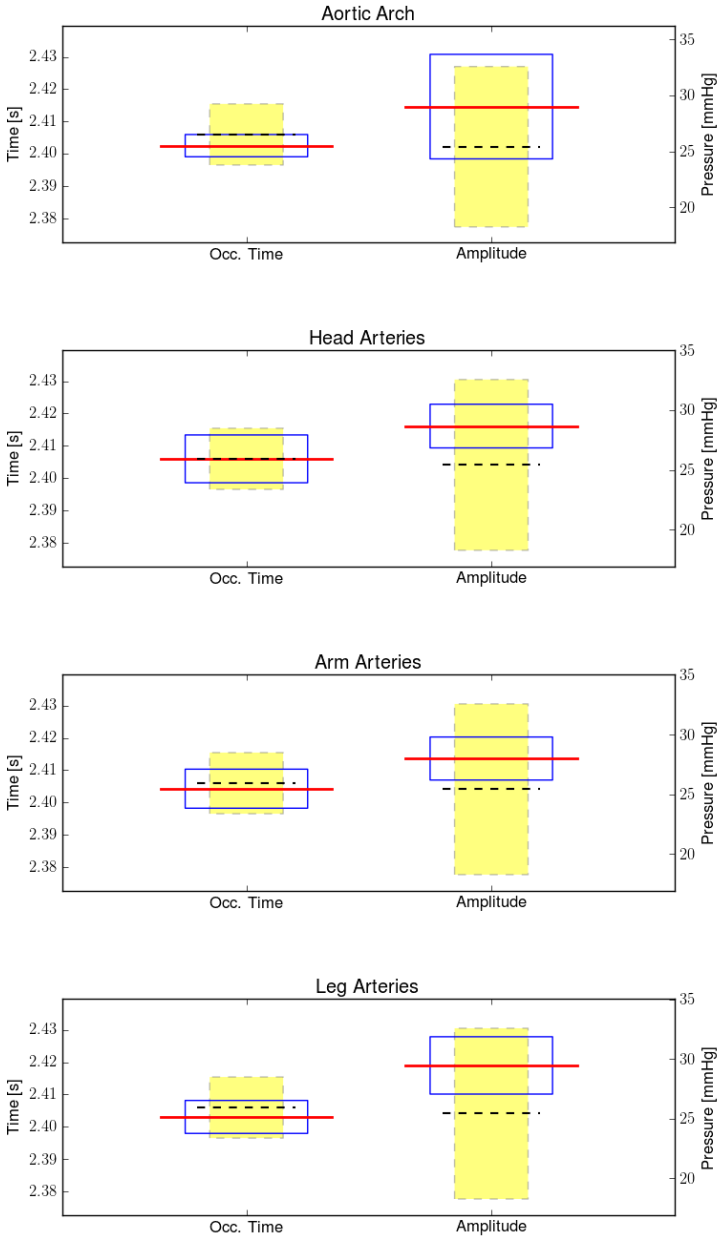

Figure 39: Box plot of the expected values and STD of the occurrence time and amplitude of the **systolic peak in the backward contribution**, for the individual uncertainty groups. The black dotted line is the total expected value with its STD as yellow plane. The red line is the expected value, and the blue box the STD, receptively, of the uncertain parameter

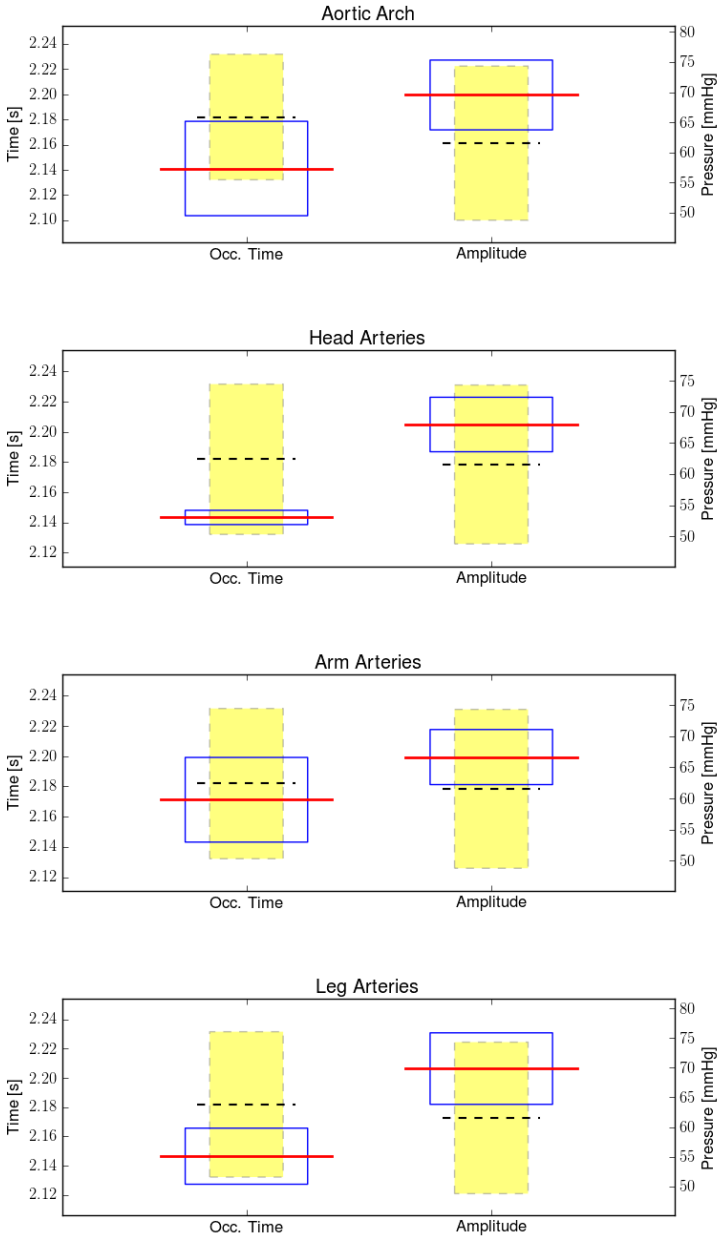

Figure 40: Box plot of the expected values and STD of the occurrence time and amplitude of the **diastolic peak in the total pressure signal**, for the individual uncertainty groups. The black dotted line is the total expected value with its STD as yellow plane. The red line is the expected value, and the blue box the STD, receptively, of the uncertain parameter

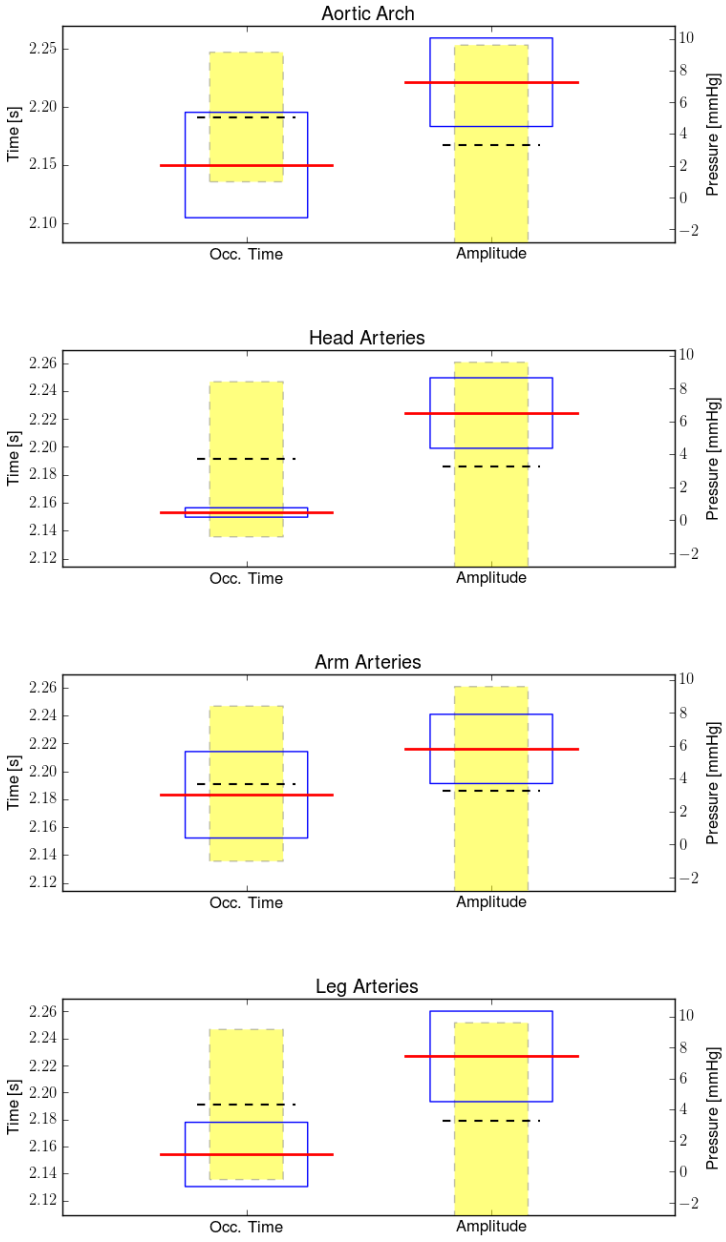

Figure 41: Box plot of the expected values and STD of the occurrence time and amplitude of the **diastolic peak in the backward contribution**, for the individual uncertainty groups. The black dotted line is the total expected value with its STD as yellow plane. The red line is the expected value, and the blue box the STD, receptively, of the uncertain parameter

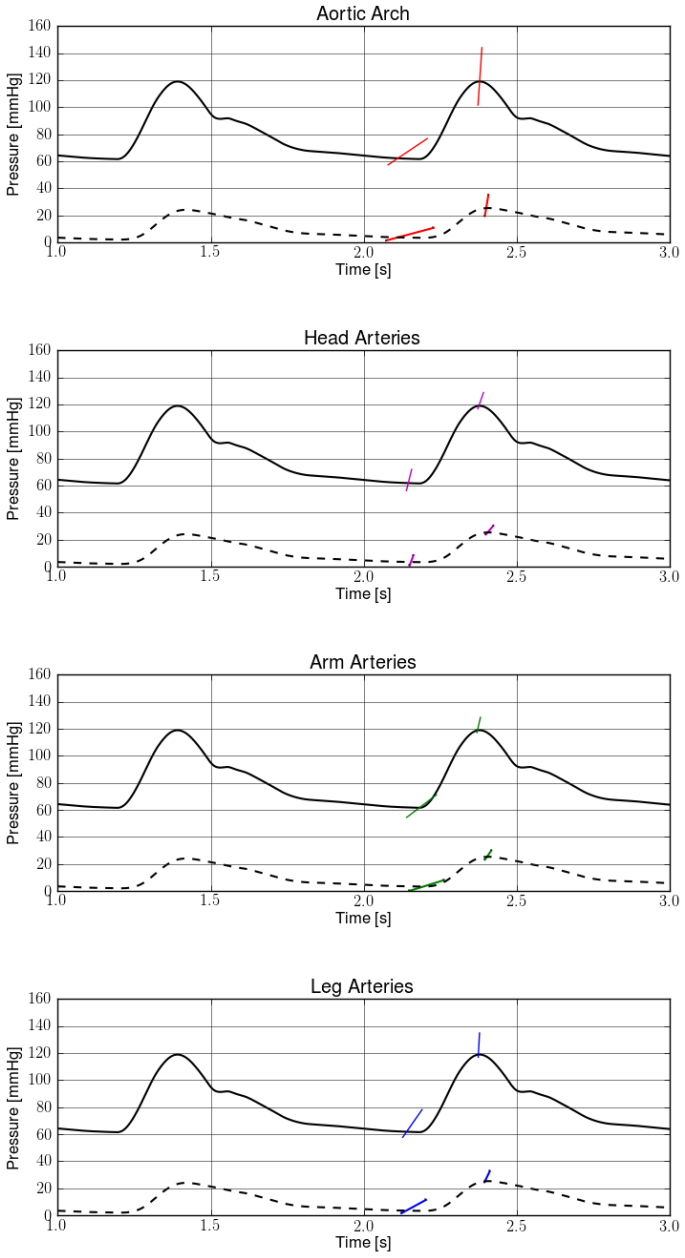

Figure 42: 99%-Confidence interval of the systolic and diastolic peaks and the expected values of the total pressure signal (continuous line) and the backward contribution (dotted line) for all uncertainty groups

Systole	total signal		backward contribution		forward contribution	
Pressure [mmHg]	Expected	STD	Expected	STD	Expected	STD
all groups	119.123	16.004	25.414	7.153	35.144	9.189
aortic arch	126.512	12.492	28.993	4.663	38.811	7.977
head arteries	125.657	3.224	28.670	1.831	38.423	1.559
arm arteries	124.706	3.354	27.990	1.803	38.051	1.727
Leg arteries	127.603	5.271	29.454	2.402	39.457	2.703

Table 11: VPC result for systolic peak occurrence time

Systole	total signal		backward contribution		forward contribution	
Occurrence Time [s]	Expected	STD	Expected	STD	Expected	STD
all groups	2.379	0.008	2.406	0.009	2.360	0.005
aortic arch	2.377	0.004	2.402	0.003	2.359	0.004
head arteries	2.377	0.006	2.406	0.007	2.359	0.002
arm arteries	2.375	0.003	2.404	0.006	2.358	0.003
Leg arteries	2.375	0.001	2.403	0.005	2.358	0.001

Table 12: VPC result for the systolic peak amplitude

Diastole	total signal		backward contribution		forward contribution	
Pressure [mmHg]	Expected	STD	Expected	STD	Expected	STD
all groups	61.542	12.781	3.279	6.323	1.777	6.473
aortic arch	69.529	5.785	7.263	2.787	2.255	3.010
head arteries	67.971	4.384	6.516	2.141	1.450	2.241
arm arteries	66.651	4.430	5.816	2.104	0.806	2.378
Leg arteries	69.862	6.032	7.434	2.919	2.422	3.119

Table 13: VPC result for the diastolic peak occurrence time

Diastole	total signal		backward contribution		forward contribution	
Occurrence Time [s]	Expected	STD	Expected	STD	Expected	STD
all groups	2.182	0.050	2.191	0.056	2.180	0.050
aortic arch	2.141	0.037	2.150	0.045	2.139	0.037
head arteries	2.143	0.005	2.153	0.003	2.142	0.005
arm arteries	2.171	0.028	2.183	0.031	2.170	0.028
Leg arteries	2.146	0.019	2.154	0.024	2.145	0.019

Table 14: VPC result for the diastolic peak amplitude

5. Conclusion and Further Work

5.1. Conclusion

The present work is concerned with the uncertainty analysis of variability in model parameters of vascular networks. Model parameters i.e. the material properties and geometry parameters of the vessels and the variables of the boundary conditions are uncertain.
In this work, the elaboration and implementation of the vascular polynomial chaos framework is presented, i.e. a simulation model to determine the effects of parametric uncertainty in vascular networks. The assessment of the model was successfully carried out by the simulation of two test cases, a single arterial bifurcation and the hole arterial tree under the influence of ageing. The simulations showed that variability in material parameters in the aortic arch are mainly influencing the shape of the pressure signal in the ascending aorta.
A framework incorporating data structures for network descriptions, network data handling, processing of pressure and flow signals *(e.g. peak detection and linear and non linear wave splitting)* and the vascular network creator (vnc) has been developed and implemented to improve the flexibility and usability of the vascular1DFlow simulation tool.
Additionally, the advanced 3D visualisation implemented in course of this work contributes to a better visualisation of simulation results and understanding of pulse wave propagation in arterial networks.

5.2. Further Work

The results of the test cases obtained with the vascular polynomial chaos, indicate the potential of the elaborated method. However, there arise several aspects for further research. More advanced statistical methods for the sensitivity analysis may increase the outcome of the investigations. This includes a method for the investigation of the "partial derivative contributions" of a branched network to the variability of pressure and flow signals. The sensitivity analysis as presented in this work estimates the variability of the solution due to each parametric uncertainty isolated. But the influence of the combination of two or more parameters respectively, is not regarded. As the system is non linear and highly coupled, those changes can have a strong influence on the simulation result. Finally, the case of the arterial tree needs to be reinvestigated with uncertain random variables for each Young's modulus in each vessel, to prove or reject the found results. The implementation of more physiological inflow boundary conditions *e.g. a varying elastance heart model combined with a aortic valve model*, would improve the investigation of the pressure and flow waves in the ascending aorta, as the prescribed inflow to the system also accounts to the shape of the pressure peak and at least partially prescribes reflections. In addition, the arterial tree should be investigated with appropriate boundary conditions at the periphery.

References

[1] A.C.L. Barnard, W.A. Hunt, W.P. Timlake, and E. Varley. A theory of fluid flow in compliant tubes. *Biophysical Journal*, 6(6):717 – 724, 1966. (Cited on page 4.)

[2] D. Bessems, M. Rutten, and F. van de Vosse. A wave propagation model of blood flow in large vessels using an approximate velocity profile function. *Journal of Fluid Mechanics*, 580(1):145–168, 2007. (Cited on page 7.)

[3] J. Bramwell and A. Hill. The velocity of the pulse wave in man. *R Soc London*, 1922. (Cited on page 7.)

[4] K. DeVault, P.A. Gremaud, V. Novak, M.S. Olufsen, G. Vernieres, and P. Zhao. Blood flow in the circle of willis: Modeling and calibration. *Multiscale modeling and simulation: a SIAM interdisciplinary journal*, 7(2):888, 2008. (Cited on page 7.)

[5] G.S. Fishman. *Monte Carlo: Concepts Algorithms and Applications*. Springer-Verlag New York, 1996. (Cited on page 15.)

[6] L. Formaggia, D. Lamponi, and A. Quarteroni. One-dimensional models for blood flow in arteries. *Journal of Engineering Mathematics*, 47(3):251–276, 2003. (Cited on page 7.)

[7] L. Formaggia, A. Quarteroni, and A.Veneziani(Eds.). *Cardiovascular Mathematics - Modelling and simulation of the circulatory system*. Springer Berlin, Heidelberg, 2009. (Cited on page 3.)

[8] C.W. Gardiner. *Handbook of stochastic methods: for physics, chemistry and the natural sciences*. Springer-Verlag, 1985. (Cited on page 15.)

[9] H.O. Georgii, editor. *Stochastik : Einfuhrung in die Wahrscheinlichkeitstheorie und Statistik*. De Gruyter, 2004. (Cited on page 15.)

[10] The Rosen Publishing Group. *The Cardiovascular System*. Britannica Educational Publishing, 2010. (Cited on page 2.)

[11] L.R. Hellevik, J. Vierendeels, T. Kiserud, N. Stergiopulos, F. Irgens, E. Dick, K. Riemslagh, and P. Verdonck. An assessment of ductus venosus tapering and wave transmission from the fetal heart. *Biomechanics and modeling in mechanobiology*, 8(6):509–517, 2009. (Cited on page 7.)

[12] C. Hirsch. *Numerical Computation of Internal and External Flows*. Butterworth-Heinemann, 2007. (Cited on pages 8, 13, 14, and 54.)

[13] T.J.R. Hughes and J. Lubliner. On the one-dimensional theory of blood flow in the larger vessels. *Mathematical Biosciences*, 18(1-2):161 – 170, 1973. (Cited on pages 4 and 5.)

[14] P.E. Kloeden and E. Platen. *Numerical Solution of Stochastic Differential Equations*. Springer-Verlag, 1999. (Cited on page 15.)

[15] H.P. Langtangen. *Python Scripting for Computational Science*. Springer Berlin / Heidelberg, 2008. (Cited on page 45.)

[16] H.P. Langtangen. *A Primer on Scientific Programming with Python*. Springer Berlin / Heidelberg, 2009. (Cited on page 45.)

[17] Y.L. Liang, H. Teede, D. Kotsopoulos, L. Shiel, J.D. Cameron, A.M. Dart, and B.P. McGrath. Non-invasive measurements of arterial structure and function: repeatability, interrelationships and trial sample size. *Clin. Sci.*, pages 669–679, 1998. (Cited on pages xv and 73.)

[18] G.V. Milovanovi and M. Stani. Construction of multiple orthogonal polynomials by discretized stieltjes-gautschi procedure and corresponding gaussian quadratures. *Ser. Math. Inform*, 2003. (Cited on page 18.)

[19] D.C. Montgomery and George C.Runger. *Applied Statistics and Probability for Engineers*. Wiley, 2006. (Cited on page 15.)

[20] W. Nichols, C. Conti, W. Walker, and W. Milnor. Input impedance of the systemic circulation in man. *Circulation Research*, 40(5):451–458, 1977. (Cited on page 78.)

[21] K. Parker. A brief history of arterial wave mechanics. *Medical and Biological Engineering and Computing*, 2009. (Cited on page 2.)

[22] T. Poinsot and S. M. Candel. The influence of differencing and cfl number on implicit time-dependent non- linear calculations. *Journal of Computational Physic*, 1986. (Cited on page 14.)

[23] Reymond, F. Merenda, F. Perren, D. Rüfenacht, and N. Stergiopulos. Validation of a one-dimensional model of the systemic arterial tree. *American Journal of Physiology - Heart and Circulatory Physiology*, 297(1):H208–H222, July 2009. (Cited on pages 3 and 78.)

[24] P. Reymond, F. Merenda, F. Perren, D. Rüfenacht, and N. Stergiopulos. Validation of a one-dimensional model of the systemic arterial tree. *American Journal of Physiology-Heart and Circulatory Physiology*, 297(1):H208, 2009. (Cited on page 6.)

[25] E.L. Schiffrin. Vascular stiffening and arterial complianceimplications for systolic blood pressurevascular stiffening and arterial compliance. *American Journal of Hypertension*, 2004. (Cited on pages 73 and 78.)

[26] S.J. Sherwin, V. Franke, J. Peiro, and K. Parker. One-dimensional modelling of a vascular network in space-time variables. *Journal of Engineering Mathematics*, 47(3):217–250, 2003. (Cited on pages 3, 6, 7, 10, and 52.)

[27] C. Soize and R. Ghanem. Physical systems with random uncertainties: chaos representations with arbitrary probability measure. *Scientific Computing*, 2004. (Cited on page 17.)

[28] N. Stergiopulos, D.F. Young, and T.R. Rogge. Computer simulation of arterial flow with applications to arterial and aortic stenoses. *Journal of Biomechanics*, 25(12):1477 – 1488, 1992. (Cited on pages xvii, 2, 71, 72, 73, 76, 77, and 78.)

[29] F.N. van de Vosse and N. Stergiopulos. Pulse wave propagation in the arterial tree. *Annual Review of Fluid Mechanics*, 43:467–499, 2011. (Cited on pages 3 and 5.)

[30] J.J. Wang and K.H. Parker. Wave propagation in a model of the arterial circulation. *Journal of Biomechanics*, 37(4):457 – 470, 2004. (Cited on pages xvii, 72, 76, 77, and 78.)

[31] B.E. Westerhof, I. Guelen, N. Westerhof, J.M. Karemaker, and A. Avolio. Quantification of wave reflection in the human aorta from pressure alone: A proof of principle. *Hypertension*, 2006. (Cited on page 78.)

[32] N. Westerhof, P. Sipkema, G. Bos, C. van Den, and G. Elzinga. Forward and backward waves in the arterial system. *Cardiovascular Research*, 6(6):648–656, 1972. (Cited on page 11.)

[33] B.J.B.M. Wolters, M. Emmer, M.C.M. Rutten, G.W.H. Schurink, and F.N. van de Vosse. Assessment of endoleak significance after endovascular repair of abdominal aortic aneurysms: A lumped parameter model. *Medical Engineering and Physics*, 2007. (Cited on page 2.)

[34] D. Xiu. Fast numerical methods for stochastic computations: A review. *Communications in Computational Physics*, 2009. (Cited on pages 15 and 17.)

[35] D. Xiu. *Numerical Methods for Stochastic Computations: A Spectral Method Approach*. Princeton University Press, 2010. (Cited on pages 18 and 19.)

[36] D. Xiu and J.S. Hesthaven. High-order collocation methods for differential equations with random inputs. *SIAM J. Sci. Comput.*, 2005. (Cited on page 20.)

[37] D. Xiu and G.E. Karniadakis. The wiener-askey polynomial chaos for stochastic differential equations. *SIAM J. Scientific Computing*, 2002. (Cited on pages xvii, 15, and 18.)

[38] D. Xiu and S.J. Sherwin. Parametric uncertainty analysis of pulse wave propagation in a model of a human arterial network. *Journal of Computational Physics*, 226(2):1385 – 1407, 2007. (Cited on pages xv, 3, 50, 51, 52, 54, 57, 58, and 70.)

[39] P. Lawford Y. Shi and R. Hose. Review of zero-d and 1-d models of blood flow in the cardiovascular system. *BioMedical Engineering OnLine*, 2011. (Cited on page 3.)

A. Appendix

A.1. Additional results of Case I

A.1.1. Expected and STD signals

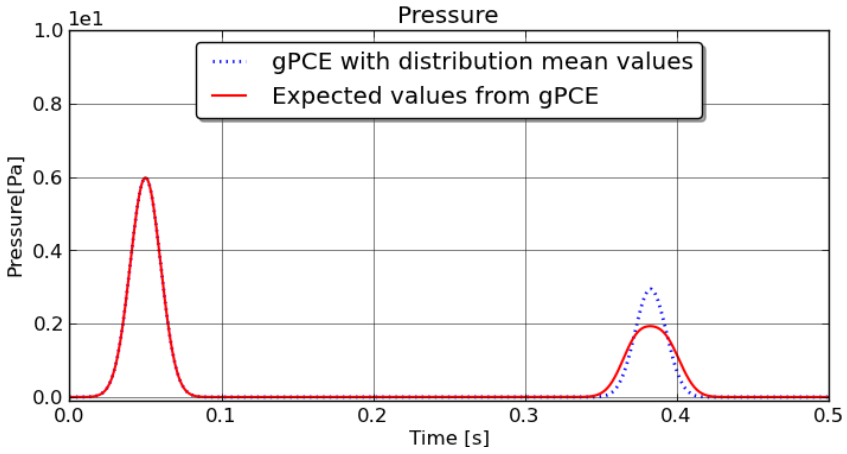

(a) Expected values signal

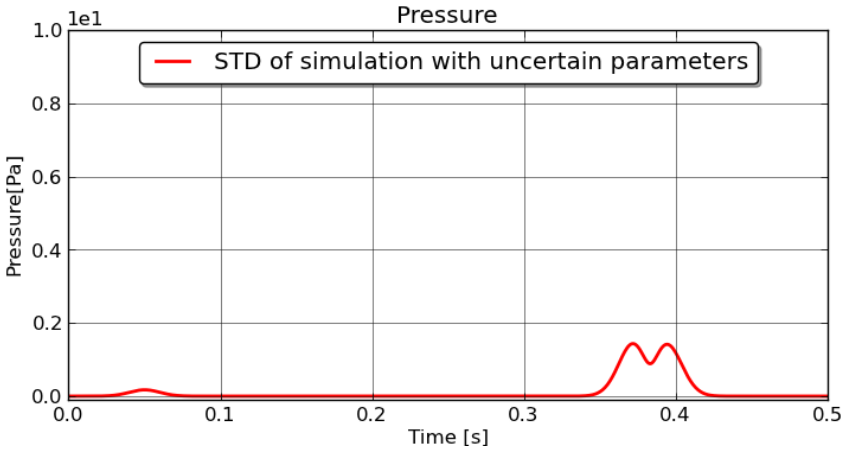

(b) STD signal

Figure 43: Additional figures test case I: expected signal and STD signal of pressure at point A

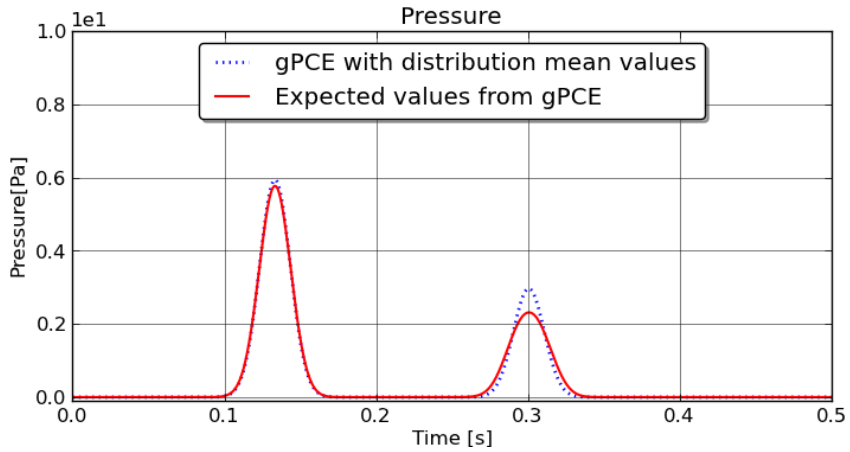

(a) Expected signal

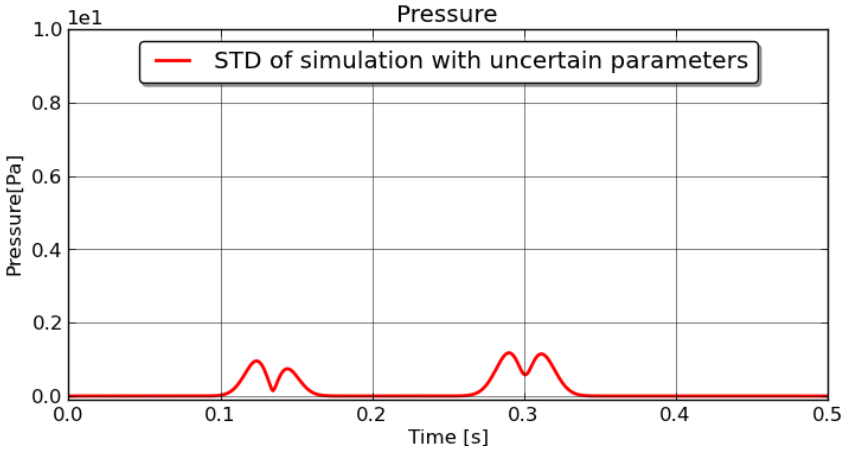

(b) STD signal

Figure 44: Additional figures test case I: expected signal and STD signal of pressure at point B

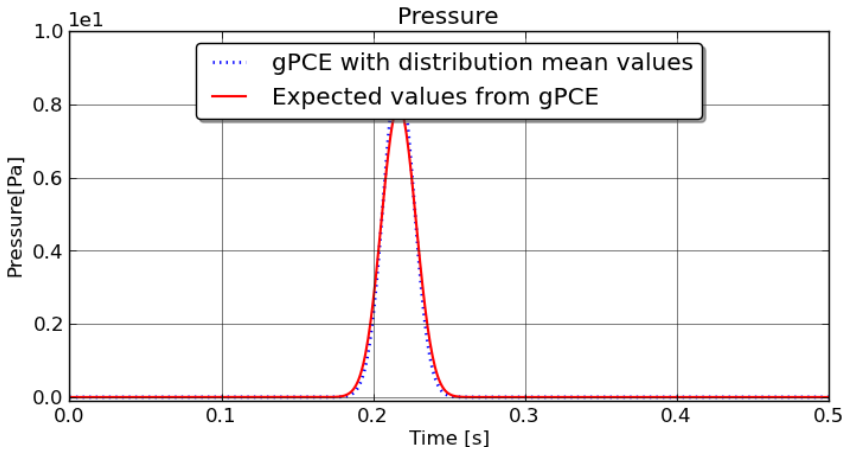

(a) Expected signal

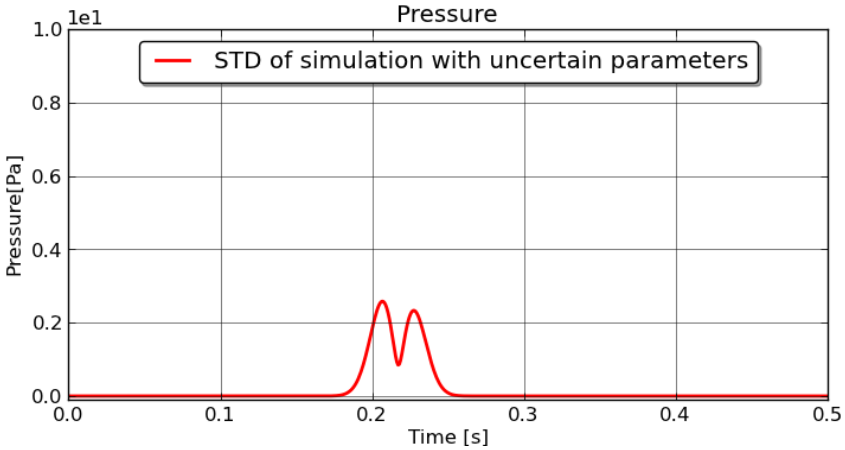

(b) STD signal

Figure 45: Additional figures test case I: expected signal and STD signal of pressure at point C

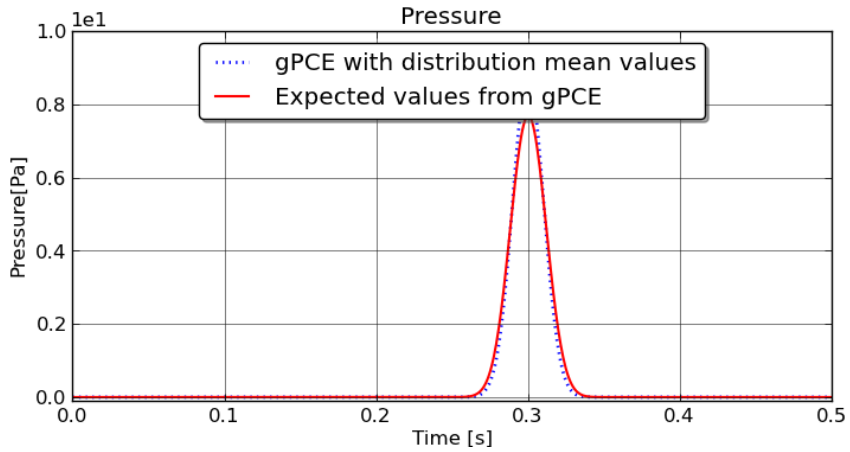

(a) Expected signal

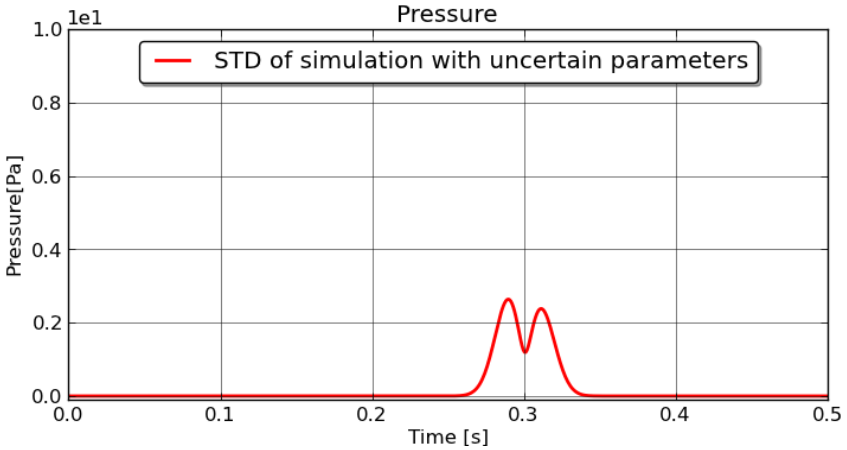

(b) STD signal

Figure 46: Additional figures test case I: expected signal and STD signal of pressure at point D

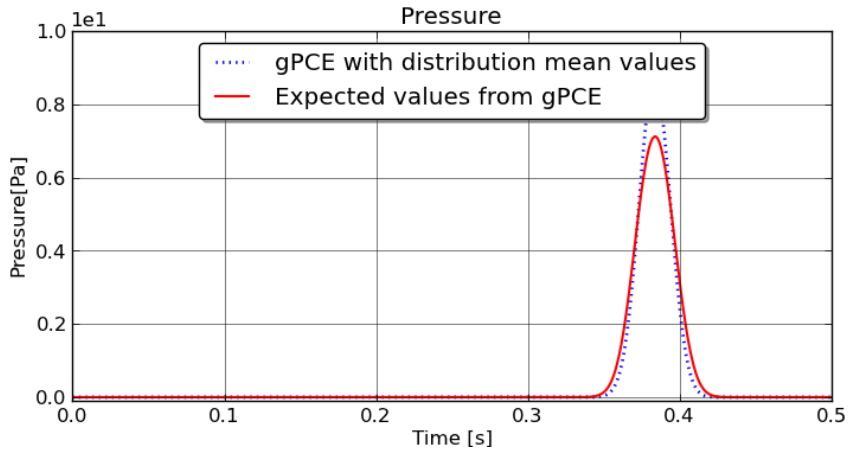

(a) Expected signal

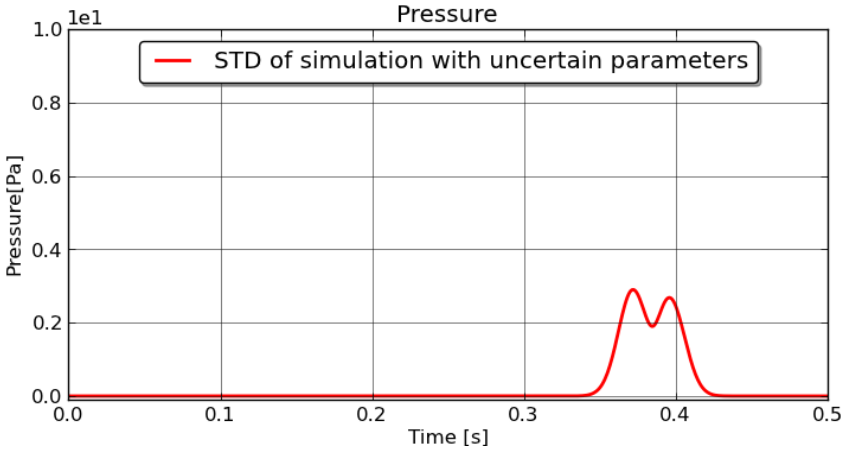

(b) STD signal

Figure 47: Additional figures test case I: expected signal and STD signal of pressure at point E

A.2. Xml-file of the Network in Case I

```
<?xml version='1.0' encoding='ISO-8859-1'?>
<polyChaosBif_Sherwin.xml version="2.0" id="1.0">
  <simulationContext>
    <CFL>0.95</CFL>
    <totalTime unit="s">0.5</totalTime>
    <NumScheme>MacCormack</NumScheme>
    <EqSystem>2</EqSystem>
    <CharSystem>0</CharSystem>
  </simulationContext>
  <boundaryConditions>
    <boundaryCondition vessel_id="0">
      <Ue>
        <Upeak unit="m s-1">0.005</Upeak>
        <C unit="s-2">5000.0</C>
        <Traise unit="s">0.05</Traise>
      </Ue>
    </boundaryCondition>
    <boundaryCondition vessel_id="1">
      <Rt>
        <Rt unit="">0.0</Rt>
      </Rt>
    </boundaryCondition>
    <boundaryCondition vessel_id="2">
      <Rt>
        <Rt unit="">0.0</Rt>
      </Rt>
    </boundaryCondition>
  </boundaryConditions>
  <globalFluid>
    <my unit="Pa s">0.0</my>
    <rho unit="kg m-3">1000.0</rho>
    <gamma unit="">-2.0</gamma>
    <dlt unit="">-0.0</dlt>
    <pref unit="Pa">0.0</pref>
  </globalFluid>
  <vessels>
    <vessel name="parentVessel" end_node="1" rightDaugther="2"
    leftDaugther="1" angleToMother="None" start_node="0" id="0">
      <grid>
        <geom>Uni</geom>
        <N>
```

```
      <scalar unit="">200.0</scalar>
      <interval unit=""/>
    </N>
    <length>
      <scalar unit="m">0.2</scalar>
      <interval unit="m"/>
    </length>
    <radiusA>
      <scalar unit="m">0.005</scalar>
      <interval unit="m"/>
    </radiusA>
    <radiusB>
      <scalar unit="m">None</scalar>
      <interval unit="m"/>
    </radiusB>
  </grid>
  <solid>
    <comp>Laplace2</comp>
    <Pfunc>True</Pfunc>
    <Ps unit="Pa">0.0</Ps>
    <As unit="m2">7.85398163397e-05</As>
    <beta>
      <scalar unit="Pa m-1">324970.0</scalar>
      <interval unit="Pa m-1">292473.0 357467.0</interval>
    </beta>
    <wallThickness>
      <scalar unit="m">None</scalar>
      <interval unit="m"/>
    </wallThickness>
    <youngModulus>
      <scalar unit="Pa">None</scalar>
      <interval unit="Pa"/>
    </youngModulus>
  </solid>
  <fluid/>
</vessel>
<vessel name="leftDaugther" end_node="2" rightDaugther="None"
 leftDaugther="None" angleToMother="25.0" start_node="1" id="1">
  <grid>
    <geom>Uni</geom>
    <N>
      <scalar unit="">200.0</scalar>
      <interval unit=""/>
```

```
    </N>
    <length>
      <scalar unit="m">0.2</scalar>
      <interval unit="m"/>
    </length>
    <radiusA>
      <scalar unit="m">0.0020411</scalar>
      <interval unit="m"/>
    </radiusA>
    <radiusB>
      <scalar unit="m">None</scalar>
      <interval unit="m"/>
    </radiusB>
  </grid>
  <solid>
    <comp>Laplace2</comp>
    <Pfunc>True</Pfunc>
    <Ps unit="Pa">0.0</Ps>
    <As unit="m2">1.30881552563e-05</As>
    <beta>
      <scalar unit="Pa m-1">796020.0</scalar>
      <interval unit="Pa m-1">716418.0 875622.0</interval>
    </beta>
    <wallThickness>
      <scalar unit="m">None</scalar>
      <interval unit="m"/>
    </wallThickness>
    <youngModulus>
      <scalar unit="Pa">None</scalar>
      <interval unit="Pa"/>
    </youngModulus>
  </solid>
  <fluid/>
</vessel>
<vessel name="rightDaugther" end_node="3" rightDaugther="None"
leftDaugther="None" angleToMother="25.0" start_node="1" id="2">
  <grid>
    <geom>Uni</geom>
    <N>
      <scalar unit="">200.0</scalar>
      <interval unit=""/>
    </N>
    <length>
```

```
          <scalar unit="m">0.2</scalar>
          <interval unit="m"/>
        </length>
        <radiusA>
          <scalar unit="m">0.0020411</scalar>
          <interval unit="m"/>
        </radiusA>
        <radiusB>
          <scalar unit="m">None</scalar>
          <interval unit="m"/>
        </radiusB>
      </grid>
      <solid>
        <comp>Laplace2</comp>
        <Pfunc>True</Pfunc>
        <Ps unit="Pa">0.0</Ps>
        <As unit="m2">1.30881552563e-05</As>
        <beta>
          <scalar unit="Pa m-1">796020.0</scalar>
          <interval unit="Pa m-1">716418.0 875622.0</interval>
        </beta>
        <wallThickness>
          <scalar unit="m">None</scalar>
          <interval unit="m"/>
        </wallThickness>
        <youngModulus>
          <scalar unit="Pa">None</scalar>
          <interval unit="Pa"/>
        </youngModulus>
      </solid>
      <fluid/>
    </vessel>
  </vessels>
</polyChaosBif_Sherwin.xml>
```